THE $^{19}F(\alpha,p)^{22}Ne$ REACTION AND THE NUCLEOSYNTHESIS OF

FLUORINE

A Dissertation

Submitted to the Graduate School

of the University of Notre Dame

in Partial Fulfillment of the Requirements

for the Degree of

Doctor of Philosophy

by

Claudio Ugalde, Fís.

_____

Michael C.F. Wiescher, Director

Graduate Program in Physics

Notre Dame, Indiana

July 2005

THE $^{19}F(\alpha,p)^{22}Ne$ REACTION AND THE NUCLEOSYNTHESIS OF

FLUORINE

Abstract

by

Claudio Ugalde

The $^{19}F(\alpha,p)^{22}Ne$ reaction is considered to be the main source of fluorine depletion during the Asymptotic Giant Branch and Wolf-Rayet phases in stars. The reaction rate still retains large uncertainties due to the lack of experimental studies available. The yields for both the ground p_0 and first excited state p_1 exit channels of ^{22}Ne have been measured with the University of Notre Dame KN van de Graaff accelerator. Several resonances were found in the energy range E_{lab}=792-1990 keV and their energies and reduced width amplitudes have been determined in the context of the R-matrix theory of nuclear reactions. A new reaction rate is provided and the impact the new rate has for the nucleosynthesis of fluorine in stellar environments is discussed.

A Xóchitl, que la quiero de aquí al Big Bang...

CONTENTS

TABLES

ACKNOWLEDGMENTS

ix

CHAPTER 1

INTRODUCTION

On December 10, 1906, the Nobel Prize in Chemistry was awarded to Henri Morrisan "in recognition of the great services rendered by him in his investigation and isolation of the element fluorine, and for the adoption in the service of science of the electric furnace called after him". Fluorine's existence had been deduced by Berzelius after his work with hydrofluoric acid but all efforts to isolate it had failed. The problem was eventually overcome by Morrisan in 1886. Fluorine has the largest electronegativity of all elements so the energy of the bonds it forms with other atoms is prodigious. For example, fluorine combines with hydrogen at temperatures as low as -230 ^oC and at ambient temperatures it forms molecules with carbon and silicon.

Fluorine is never observed isolated in Nature. On Earth's crust it is found more commonly as fluorite (CaF_2, widely used in the experimental part of this work), a cubic crystal of high transparency used in the manufacture of photographic-quality glass. Beyond our atmosphere, fluorine would be found more commonly bound to the most abundant nucleus in the universe: hydrogen. Astronomers usually look for absorption lines of HF, hydrofluoric acid, when looking for fluorine.

One of the most popular applications of fluorine is in stomatology, more specifically in teeth health. Our teeth are made of calcium hydroxyapatite, a compound

of calcium, phosphorus, and oxygen and by adding sodium monofluorophosphate to toothpaste and water some of the surface material in the teeth is supposed to turn into fluorapatite by contact. Fluorapatite is a very hard material so in the enamel, it prevents teeth from decay. However, if abused, excess fluorine in water causes mottled enamel in teeth. Another compound of fluorine, SF_6, is an excellent insulating gas widely used in electrostatic particle accelerators to reduce sparking between mechanic and electric elements within the tank.

Fluorine by itself is an extremely corrosive and toxic yellow gas; it forms molecules even with noble gases. By diffusion of UF_6 fluorine can be used to isolate uranium for nuclear weapons development and it was during World War II that fluorine extraction was optimized to the point of being made commercially available. Another type of compounds of fluorine that would be lethal to life in the planet are chlorofluorocarbon gases (CFCs or more commonly "freons"), used in refrigeration until when in 1987 the *Montréal Protocol* was signed, regulating its use. Mario Molina and Sherwood Rowland had explained fourteen years before how the ultraviolet light-shielding ozone layer in the stratosphere would be destroyed by the decompostition of the CFC molecule.

Nevertheless, fluorine is a nucleus far from being abundant in nature. In fact it is the least abundant of nuclei with atomic mass between 11 and 32 (there is only one fluorine atom per every 3.3×10^7 hydrogen atoms in the Sun [3]). This suggests that either fluorine is very hard to nucleosynthesize or it is extremely fragile in stellar environments. Today the mechanism of synthesis of fluorine is still highly debated. However, it would sound reasonable to anticipate that it is made in different stellar environments, each contributing to the abundance we can observe.

In this work we have investigated the nuclear reaction that seems to be the major source of fluorine destruction in Nature: the $^{19}F(\alpha,p)^{22}Ne$ reaction. Our main goal is to provide stellar astrophysicists with a reaction rate as accurate as possible and we do this both by reproducing and observing the reaction in the laboratory and by the application of nuclear models of the reaction mechanism to the analysis of the experimental data. The idea of the problem came about as astrophysicists realized that the abundance of fluorine is largely affected by the uncertainty in the rate of the $^{19}F(\alpha,p)^{22}Ne$ reaction. But, where does this rate come from? How reliable it is? Can we improve it?

To try to answer these questions we looked at Thielemann et al.'s [91] *REA-CLIB* library, probably the most widespread reaction rate compilation today. They list a rate for the $^{19}F(\alpha,p)^{22}Ne$ reaction made up of a resonant and a non-resonant term, both from Caughlan and Fowler's famous compilation in 1988 [15]. Now, refering to these authors one finds a table with the rate evaluated in the temperature interval $0.003 \leq T_9 \leq 10.0$. An expression for its evaluation is given as well (see figure 6.2 for a plot of their rate):

$$N_A\langle\sigma v\rangle = 4.50 \times 10^{18} \times T_9^{-2/3} * \exp(-43.467T_9^{-1/3} - (T_9/0.637)^2)$$

$$+7.98 \times 10^4 T_9^{3/2} * \exp(-12.760/T_9). \tag{1.1}$$

They do not provide further details on how they estimated the rate but they mention their paper to be an update of their own previous work. We looked in their older publications. First, Caughlan and Fowler's 1985 compilation of rates [16] only lists the $0.003 \leq T_9 \leq 10.0$ table of the rate; however, no further discussion or even equation 1.1 are mentioned as only revised rates were discussed

in this paper. Looking backwards, neither Harris et al.[45] nor Harris[44] update the rate, so no mention to it is made. However, Fowler et al. [33] show again equation 1.1 for the rate, without further comments; before this compilation no information whatsoever is found about the rate. This means that probably the first calculation was made between 1967 and 1975. But where and how? A place to look for is literature cited in Fowler et al.'s paper[33] dated between 1967 and 1975. It was Wagoner [100] who first calculated the reaction rate by following the recipe from Fowler and Hoyle's 1964 work[32]. The calculation of the rate is a theoretical evaluation that assumes a "blackbody" nucleus in the framework of the optical model. Wagoner states that the rate is only valid above $T_9 = 0.8$, fact that is not considered in the propagation of the rate to the compilation published in 1988. It could have been possible to obtain a rate based on experimental results by using the work of Kuperus in 1965 [65]; it seems that the nuclear astrophysics group at Caltech never knew of Kuperus's work.

Having discussed the status of the almost 40-year-old rate for the $^{19}F(\alpha, p)^{22}Ne$ reaction it is clear that an update is urgent; here we do so. The structure of this work is as follows: in chapter 2 the three astrophysical environments where fluorine is thought to be synthesized are described. Chapter 3 describes the reactions important in the nucleosynthesis of fluorine in AGB and Wolf-Rayet stars; a summary of the rates is given and an update of the $^{14}C(\alpha, \gamma)^{18}O$ and $^{18}O(\alpha, \gamma)^{22}Ne$ reactions is given. In chapter 4 the experimental work for measuring the $^{19}F(\alpha, p)^{22}Ne$ reaction is presented. In particular the development and successful preparation of a stable fluorine target for measuring the reaction is described. Chapter 5 discusses the interpretation of the experimental data in terms of an R-matrix formalism of nuclear reactions; a new R-matrix analysis code is introduced. In chapter 6 the

rate for the measured reaction is presented and a discussion on the impact the new rate has on the destruction of fluorine in AGB stars is given. Finally, chapter 7 has the conclusions of this work and future experimental and theoretical research is suggested.

CHAPTER 2

NUCLEOSYNTHESIS OF FLUORINE

To date three different scenarios for the nucleosynthesis of fluorine have been proposed. The first includes the neutrino dissociation of ^{20}Ne in supernovae type II; it was proposed by Woosley and Haxton in 1988 [104]. A year later, Goriely, Jorrisen, and Arnould [39] examined several possiblities including hydrostatic H- and He-burning, and explosive He-burning. They concluded that ^{19}F could be produced both during the thermal pulse phase of AGB stars and by hydrostatic burning in the He-shell of more massive stars. To date, none of the possiblities has been verified to dominate over the others. It is likely that all three contribute to the formation of fluorine in the Universe.

2.1   The ν-process scenario

On February 23, 1987, a bright spot appeared in LMC's Tarantula Nebula. While working at Las Campanas observatory in Atacama, Chile, Ian Shelton and Oscar Duhalde discovered what may be the most important supernova ever observed: 1987A. The star could be seen with an unaided eye as its magnitude was an astonishing 5th. Within hours after the news of the event spread, most telescopes in the Southern Hemisphere and in orbit were pointing at 1987A. Ultraviolet instruments caught the light curve on its way down while curves in the

optical could be registered still while rising. Hydrogen lines showed in the spectra. A type II supernova had just gone off.

Meanwhile, on the northern side of the globe physicists at Kamioka in Japan and Cleveland in the US had been trying to observe neutrinos from proton decays with their huge water tanks Kamiokande II and IMB, respectively. When they heard the news about 1987A they went back to their records and concluded independently that a burst of neutrinos had reached their detectors at the same time. Overall, the detected burst consisted of 19 events in 15 seconds; 10^{58} neutrinos had been ejected from supernova 1987A [73].

As the core of a massive star collapses in a supernova type II event electrons are captured by nuclei and neutrinos are released. Only a very small fraction of the gravitational energy of the remnant is carried out by the shock wave; the rest is radiated in neutrinos [46]. Almost all the layers of the collapsing star are transparent to the neutrino flux. However, some neutrinos may lose energy by their charged-current reactions on some nuclei and free nucleons, and by both charged and neutral current scattering off electrons.

Neutral-current inelastic scattering off nuclei dominates over other heating processes as all neutrino flavors participate in this type of interaction. Different regimes of neutrino interactions can be identified during the collapse of a supernova. In the first one, during the early stages of the collapse, neutral current scattering and other inelastic processes enhance thermalization of electron neutrinos. This means that this type of neutrinos can escape from the core as their mean free paths are increased. Protons are freed from electron-neutrino thermalization and electrons captured as a result. In the second stage (some milliseconds after core bounce) the shock wave moves into the neutrino region and the energy of

the shock front is dissipated by photodisintegration of ^{56}Fe, other nuclei passing through the shock, and by neutrino production. A burst of relatively low-energy neutrinos is produced at this moment and a significant fraction of the energy carried by these neutrinos is used to preheat ^{56}Fe outside the shock front. Once ^{56}Fe has been preheated its dissociation would require less energy; at the same time most of the energy of the shock front is retained while it moves through the iron core. The result is that the chance of an explosion is increased. As the supernova collapse enters the cooling stage the temperature of μ and τ neutrinos rises with respect to that of electron neutrinos and their reaction cross section increases as well. Nevertheless, neutrino nucleosynthesis could only succeed in a well defined set of conditions. In the first place, if it happens very close to the core the products would never escape the collapsing star before being destroyed. On the other side, if the synthesis is far away, the neutrino flux would be too small to produce a non-negligible amount of the new nuclei. Good candidates to fulfill this condition for synthesis of fluorine are the carbon and neon shells in type II supernovae.

Fluorine may be produced in this scenario [104] [103] by a two-step process. First, μ and τ neutrinos interact with ^{20}Ne via neutral current inelastic scattering, and then the excited $^{20}Ne^*$ emits a proton, i.e.

$$^{20}Ne(\nu, \nu')^{20}Ne^* \rightarrow {}^{19}F + p. \tag{2.1}$$
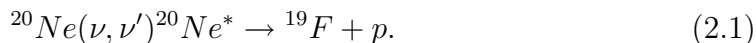
However, $^{20}Ne^*$ has more decay modes. First and most important,

$$^{20}Ne^* \rightarrow {}^{19}Ne + n, \tag{2.2}$$

8

and second but almost irrelevant

$$^{20}Ne^* \rightarrow {}^{16}O + \alpha. \tag{2.3}$$

The branching ratio between proton and neutron emission is 0.66 to 0.30. On the other side, the $\alpha-$emission channel is blocked as most of the states populated via neutrino inelastic scattering are isovector.

A typical neutrino temperature in this scenario is 10 MeV, with a mean cross section per flavor of 2.7×10^{-17} barns. The flux of neutrinos can be estimated from the total energy of neutrinos produced in the collapse ($\sim 3 \times 10^{53}$ erg), the radius of the neon-rich shell ($\sim 2 \times 10^9$ cm), and the neutrino temperature. For a Fermi-Dirac distribution of neutrinos the flux at the neon shell would be 1×10^{38} cm^{-2}). With the branching ratio of proton to neutron emission, the estimate of the amount of fluorine produced via this mechanism is $0.0042 \times [^{20}Ne]$, such that $[^{20}Ne]$ is the original abundance of ^{20}Ne. This is about one order of magnitude larger than the solar abundance.

There are two main mechanisms for fluorine destruction in supernovae type II. First, all the protons available in the environment could react with fluorine via $^{19}F(p,\alpha)^{16}O$. Second, when the shock front moves through the neon shell the temperature rises and $^{19}F(\gamma,\alpha)^{15}N$ can become important at $T_9 > 1.7$.

Recently, Heger et al.[47] improved previous work on neutrino nucleosynthesis by including in their model the mass loss in the evolution of the progenitor. They also updated their reaction network by including all elements through bismuth and improved the reaction rates calculated with new $^{20}Ne^*$-decay branching ratios. Their cross sections are smaller than those of Woosley et al.[103]. This translates into a reduction of ^{19}F by 50%.

Some of the most important uncertainties in this model for fluorine nucleosynthesis are the mass loss rates in the progenitor of the star, the neutral-current cross sections, and most important, the fact that current supernovae type II codes with $\nu-$process do not lead to the explosion of the star. Nevertheless, fluorine has never been observed in a type II supernova remnant.

2.2 The AGB star scenario

It was in 1992 when Alain Jorrisen, Verne Smith, and David Lambert [56] published their results after analyzing the composition of a set of giant stars. They claimed to have found fluorine in their samples.

Their data consisted of high-resolution infrared spectra taken at a wavelength around 2.2 μm with the 4 meter telescope and the Fourier Transform Spectrometer at the Kitt Peak National Observatory in Arizona and included M, MS, S, K giants, a couple of cool barium stars, SC, and N and J stars. These observations not only confirmed that fluorine is produced in a He-burning site but were also able to constrain models of AGB stars.

By the time most of the information about the abundance of fluorine in the galaxy was reduced to that coming from the solar system itself and these observations are the first extensive work in which fluorine abundances were reported from sources outside the solar system. Previous observations of uncertain abundances of extra solar fluorine were limited to some planetary nebulae, α Ori (Betelgeuse), and circumstellar medium.

Fluorine was found to be enhanced in C and S stars (carbon rich) with respect to K and M (oxygen rich) stars. This suggested the He-burning site, where carbon is produced by the triple alpha reaction, to be the same as where fluorine is

synthesized. However, there are two different effects that control the amount of fluorine relative to carbon in a star; on the one hand the alteration of the abundances during the life of the star and on the other the differences in primordial compositions due to galatic chemical evolution. Looking for a correlation between the amounts of C and F on the surface of the star requires disentanglement of these effects; both the abundances of carbon and fluorine need to be normalized to the abundance of a species sensitive only to galactic chemical evolution and not to AGB nucleosynthesis. A good candidate is oxygen. In fact Jorrisen et al. found a positive correlation between fluorine and carbon while carbon and oxygen abundances remained uncorrelated in their analysis.

2.2.1 Evolution to the AGB phase

The evolution of a star from the main sequence (MS) to the AGB phase is highly dependent on both the initial mass and metallicity. A low mass star ($M \sim 1 M_\odot$) in the main sequence burns hydrogen into helium in its center and due to the increasing molecular weight the density rises and its temperature with it. When hydrogen is exhausted the helium core starts growing by burning hydrogen in a shell around it. The density keeps increasing until the central core becomes electron degenerate and the outer layers of the star respond to the increasing temperature in the core by expanding and cooling down; they become convective and the star leaves the main sequence at this point (zero age main sequence or ZAMS) into the red giant branch (RGB).

The convective region in the star extends down to the upper layers of the helium-rich region and some of the nuclei produced from hydrogen burning (as $^4He, ^{13}C, ^{14}N$) are then moved up to the stellar surface; this event is called the

first dredge-up. The He-rich core is inert at this time of the evolution but keeps contracting and heating. However, neutrino cooling moves the maximum of temperature in the core from the center outward until He-burning is ignited where the temperature is at a maximum. The core is degenerate and will not cool down by expanding so the temperature rises dramatically and He burning with it. The core suffers a partial runaway and the star flashes.

After the flash the star cools down and starts burning helium in a convective core and hydrogen in a shell around it; the star then settles down in the horizontal branch (HB). When helium is exhausted in the core the star leaves the HB by expanding its envelope and increasing its luminosity again. The C-O core becomes electron degenerate and He and H are burned in shells. The star then enters the asymptotic giant branch phase (AGB).

A star with a higher mass ($> 4M_\odot$) behaves different as after the first dredge-up He-burning establishes at its center in nondegenerate conditions; hydrogen burns in a shell above the core. When helium is exhausted in the core it starts burning in a shell. The outer layers of the star expand and cool down and hydrogen burning stops; as the luminosty increases the star moves towards the AGB phase. Later on, the convective envelope penetrates down to the shell where hydrogen was burnt before and material is brought to the surface. This event is the second dredge-up and it only happens for these more massive stars. After the dredge-up the hydrogen shell reignites and the star finally enters the AGB phase.

Jorrisen et al. [56] found that K and M stars have a $^{19}F/^{16}O$ value larger that solar. Nevertheless, Mowlavi et al.[79] showed that neither the first nor the second dredge up events can account for this enhancement.

2.2.2 Stellar structure at the AGB phase

The structure of a star at the AGB phase is fundamentally the same for all stellar masses. From the center outwards there is an electron degenerate carbon and oxygen (C-O) core. The temperature in this region is not high enough to ignite further reactions. Above the core there is a He-rich (helium intershell) region where at the bottom He burns by the triple alpha reaction (helium burning shell). Then there is the hydrogen rich region. At its bottom hydrogen is being burnt (H-burning shell). Finally the outermost layer of the star is the convective envelope (see figure 2.1).

For stars of low mass there is a radiative region between the envelope and the H-burning shell. For more massive stars this radiative region dissapears as the temperature can be high enough to ignite hydrogen burning at the base of the envelope. This is called hot bottom burning (HBB).

The helium intershell is where the most diverse nuclesynthetic processes occur. On the one hand, nuclear burning occurs both at its bottom (He-burning) and top (H-burning), and on the other, it is thin enough that whenever energy from burning is dumped here temperature increases with no pressure changes at all. These two facts make the intershell a very unstable region and at some point in the early AGB phase this region will start pulsating.

An increase in temperature will cause the rate for the triple alpha reaction to go up abruptly. In this case a higher rate means more energy produced in the intershell and the temperarure gradient is enhanced even more. The energy loss due to the increasing temperature gradient increases until energy is dumped in the intershell faster than the rate at which it is lost; enough cooling by radiation is not achieved so convection starts, the region then becomes unstable and a
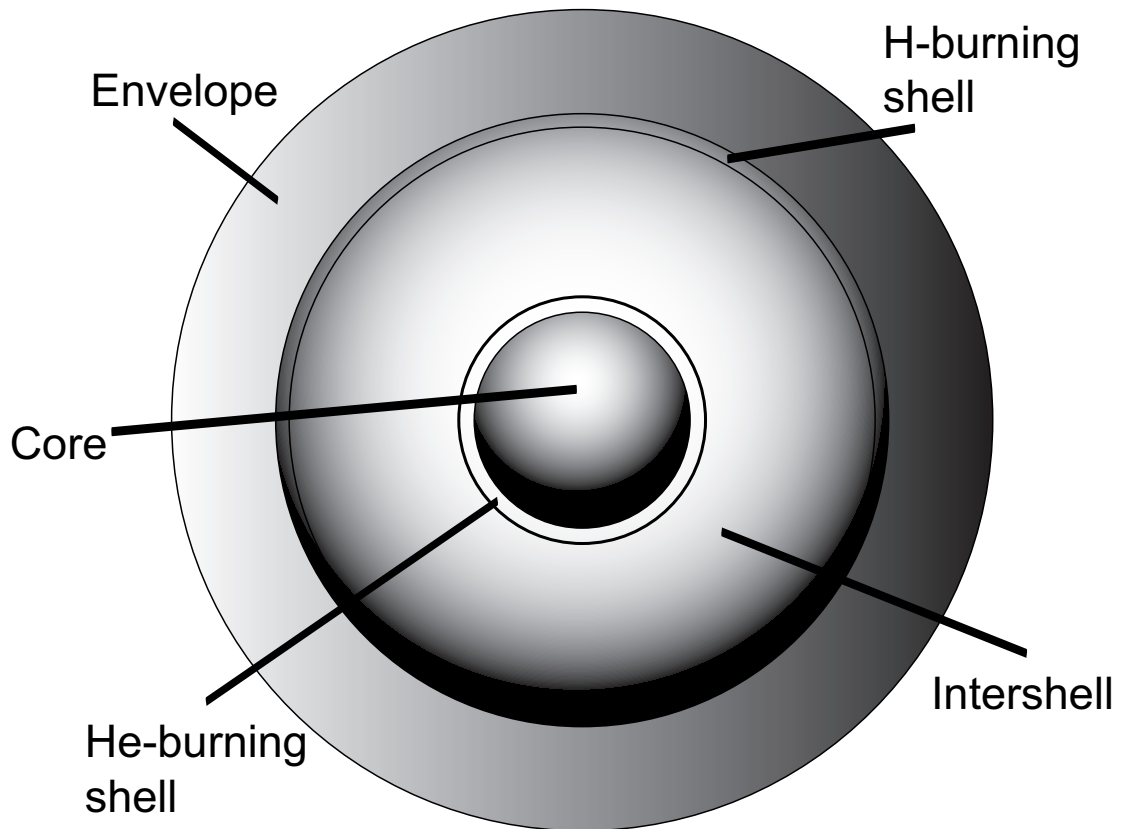
Figure 2.1. Schematic of the structure of a star in the AGB phase. The core of the star is carbon and oxygen rich in a degenerate state. It is surrounded by a semiconvective He-rich intershell. The outer envelope is convective and hydrogen rich. There are two regions where thermonuclear burning takes place: an inner He-burning shell and a H-burning region below the convective envelope. The figure is not drawn to scale.
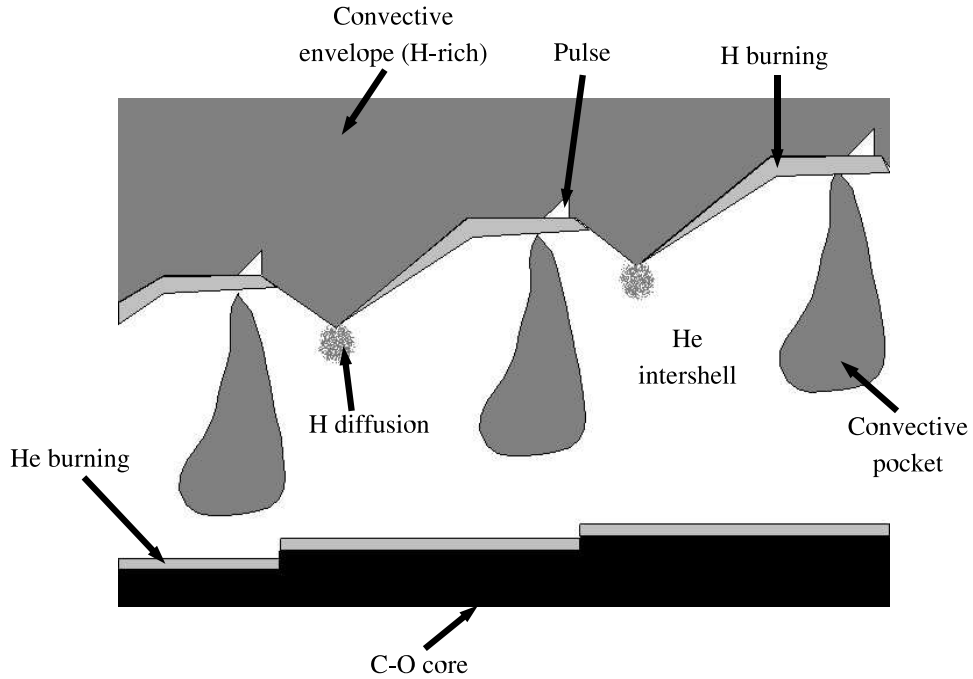
Figure 2.2. Schematic of the structure of the helium intershell. The vertical axis represents the mass and spans from 0.65 to 0.68 $M_\odot$ in a $3M_\odot$ star. The horizontal axis is the model number. The dark region at the bottom of the figure represents the electron-degenerate carbon-oxigen core. The region engulfed by the helium and hydrogen burning shells is very unstable and it flashes periodically. As a result convective regions (pockets) are formed and the envelope moves down to the helium-rich region (TDU), probably mixing down some of the protons into the intershell (PMZ).

pulse is triggered. After the pulse the intershell becomes radiative again and the convective envelope penetrates the upper region of the intershell; freshly made nuclei are then brought to the surface of the star (third dredge-up or TDU). (See figure 2.2 for details). However, this process can not be reproduced consistently for AGB stars of low mass [51]. Recent work by Karakas [58] showed that the efficiency of the TDU is highly dependent on both the mass and metallicity of the star.

The TDU repeats several times as hydrogen is brought down to a hotter region where it can be burnt, starting the heating up of the region all over again.

2.2.3 Fluorine production in AGB stars

Fluorine nucleosynthesis in AGB stars takes place in the intershell region when ^{14}N leftovers from the CNO cycle capture a ^4He from the He-rich environment. The unstable ^{18}F nucleus is formed and it decays with a half life of 109.8 minutes to ^{18}O. Both a proton or a ^4He can be captured by ^{18}O. In the former case an alpha and a ^{15}N are produced, while in the latter ^{22}Ne is made instead and no fluorine production takes place. This is known as a "poisoning reaction". When ^{15}N captures an alpha fluorine is produced . The environment in the intershell is not hydrogen rich so protons need to be produced in some way: the most efficient mechanism is the $^{14}N(n,p)^{14}C$ reaction. The neutrons required for this reaction to take place come from the $^{13}C(\alpha,n)^{16}O$ reaction. Some other protons may be mixed in when the convective envelope penetrates the intershell region at the end of the TDU.

Mowlavi et al.[79] explained only the lowest fluorine overabundances observed at the surface of AGB stars. They proposed that an additional source of ^{13}C would

16

account for the largest fluorine contents. Besides, they found that massive AGB stars will not produce large fluorine abundances and that low metallicity stars have less fluorine dredged-up to the surface than solar metallicity stars. However, the models they used did not reproduce the TDU consistently and they had to introduce it artificially[30].

One of the most important and interesting problems in AGB stellar structure and evolution is the formation of the ^{13}C-rich region that eventually would be the source of neutrons necessary not only for the synthesis of fluorine but for the main component of the s-process [14]. It is thought that ingestion of protons into the He intershell during the TDU leads to the formation of ^{13}C through the chain $^{12}C(p, \gamma)^{13}N(\beta^+\nu)^{13}C$, where ^{12}C is a product of He burning and therefore is relatively abundant in the intershell region [54]. However, the proton diffusion mechanism into the intershell is not well understood yet. Some possible explanations of the process include stellar rotation [68], convective overshooting [52], and gravitational waves [24].

With neutrons available in the environment an alternate reaction chain starting with the $^{14}N(n, p)^{14}C$ reaction is plausible as well. This reaction not only makes the protons required by $^{18}O(p, \alpha)^{15}N$ but also produces ^{14}C that may capture a ^4He and produce more of the ^{18}O required to synthesize fluorine.

Fluorine is very fragile. There are three main reactions that may lead to fluorine destruction. First, due to the high abundance of ^4He in the region, the $^{19}F(\alpha, p)^{22}Ne$ would play an important role. Second, other less abundant nuclei could be captured by fluorine as well. One case is protons ($^{19}F(p, \alpha)^{16}O$) and the other is neutrons ($^{19}F(n, \gamma)^{20}F$), where neutrons are produced by the $^{22}Ne(\alpha, n)^{25}Mg$ reaction.

The discovery of fluorine in extremely hot post-AGB stars with FUSE (Far Ultraviolet Spectroscopic Explorer) has been reported by Werner et al. [101]. Due to the high effective temperature of these stars material is usually highly ionized and absorption lines appear in the far ultraviolet region of the spectrum. The authors found very high overabundances of fluorine with respect to solar's in hydrogen-deficient stars and confirmed the general trend of increasing F abundance with increasing C abundance discussed in 2.2. Today, independent observations of over-abundances of fluorine confirm that stars in the AGB phase are producers of this rare element.

2.3   The Wolf-Rayet Star scenario

During the Second International Symposium on Nuclear Astrophysics (Nuclei in the Cosmos II) held at Karlsruhe, Germany in July 1992, Meynet and Arnould 1993 [74] presented the first quantitative work on nucleosynthesis of fluorine in hydrostatic He-burning sites after following the suggestion by Goriely et al.[39]. They showed that it is not the He-burning shell that can produce fluorine but instead during the early He-burning core phase where the synthesis takes place. Nevertheless, they were concerned with the fact that the $^{19}F(\alpha,p)^{22}Ne$ reaction would have destroyed all fluorine by the end of that phase. The only way out of the problem was to propose that the star would eject ^{19}F before the completion of the He-burning phase. The process of mass ejection while the core is burning He occurs in Wolf-Rayet stars; ^{19}F enrichment of the interstellar medium with fluorine can become important for a higher metallicity.

Later on, Meynet and Arnould 2000[75] extended their own work by including a wider range of initial masses and metallicities in their analysis. They also included

improved mass loss rates and a moderate core overshooting [76]. Their conclusion was that the highest fluorine yields come from stars with solar metallicities and masses ranging between 40 and 85 $M_{\odot}$. Wolf-Rayet stars with lower metallicities have weaker winds and uncover the He-burning core only for the most massive stars but after ^{19}F has already been burnt. For higher metallicities and for masses above 85 $M_{\odot}$, the H-burning core decreases so rapidly during the main sequence because of the strong stellar winds that the He-burning core becomes too small for being uncovered by the stellar winds later on.

Fluorine would be synthesized in Wolf-Rayet stars through the main reaction chain

$$^{14}N(\alpha, \gamma)^{18}F(\beta^+)^{18}O(p, \alpha)^{15}N(\alpha, \gamma)^{19}F \qquad (2.4)$$
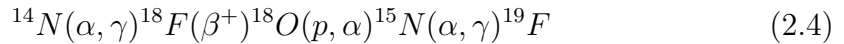
where neutrons come from $^{13}C(\alpha, n)^{16}O$ and protons from $^{14}N(n, p)^{14}C$. The main source of fluorine destruction is thought to be $^{19}F(\alpha, p)^{22}Ne$.

According to [75] Wolf-Rayet stars could account for most of the content of fluorine in the solar system. Nevertheless, fluorine has never been observed in a Wolf-Rayet star.

2.4 Galactic enrichment of fluorine

There have been several attempts to explain the origin of galactic fluorine. However, none of them is conclusive. Most important is the lack of observational data. Fluorine abundance studies are limited to the solar system (see Anders and Grevesse, 1989[3], for example), the work by Jorrisen et al.[56] for stellar abundances in the Milky Way and more recently, the first observations of fluorine outside our galaxy by Cunha et al.[18] in the LMC and the globular cluster ω Centauri and Smith [89] in ω Centauri. It is certainly necessary to extend research

in this direction.

Timmes et al.[93] have modelled the galactic chemical evolution of 76 stable elements from hydrogen to zinc with a simple galactic dynamical model. They concluded that metal-poor dwarfs would have a subsolar fluorine-to-oxygen ratio. At larger metallicities they were successful to describe Jorrisen's[56] normal K-giant observations. Other peculiar giant-star fluorine abundances were not described well as their model did not include contribution from AGB stars; the claim is that half of the solar fluorine abundance may come from supernovae type II events and the other half from AGB stars. In 2001, their results were verified by the model of Alibés et al. [2].

Later on, Timmes et al.[92] suggested that if fluorine could be detected at large redshifts (Z> 1.5) in quasi-stellar objects (QSO) this would be the strongest evidence possible for the existence of the $\nu-$process in massive stars. Nevertheless, these observations have not happened yet.

Katia Cunha and collaborators's recent observations [18] are in agreement with Timmes's predictions [93] about the fluorine-to-oxygen ratio for metal-poor stars in the LMC. This means that the main mechanism for fluorine nucleosynthesis in the LMC is not the AGB process. The Wolf-Rayet scenario could not be tested as at the time no prediction of chemical evolution included yields from this mechanism.

More recently Renda et al.[86] studied the chemical evolution of fluorine in the Milky Way by including yields from all three nucleosynthesis mechanisms. Their model fails to reproduce fluorine abundances in the solar neighborhood when only contributions from supernovae type II are included. However, their full model is in agreement with the observational data. AGB stars would have

enriched significantly the interstellar medium with fluorine during the course of evolution of the Milky Way. On the other hand, comparison of their results with observations from the LMC and ω Centauri was not possible due to the star formation and chemical evolution differences with the Milky Way. They speculate that in this case earlier generations of supernovae type II were responsible for the current fluorine abundances.

CHAPTER 3

THE RATES OF REACTIONS RELEVANT TO FLUORINE SYNTHESIS

In this chapter a summary of the nuclear reactions and rates relevant to the nucleosynthesis of fluorine in both AGB and Wolf-Rayet star scenarios is presented. First the concept of the rate of a reaction is introduced and its different types are discussed. An overview of the current status of the various reaction rates used in this work is presented and necessary experimental research is suggested.

3.1 The equations of stellar structure and evolution

Here we make an account of the basic equations of stellar structure. They have been discussed elsewhere and the reader is referred for example to [62] for a detailed description of their derivation. The first equation represents the mass distribution in a spherically symmetric stellar model and can be written as

$$\frac{\partial r}{\partial M_r} = \frac{1}{4\pi r^2 \rho},$$ (3.1)

where r is the distance from the center of the star to the mass shell element M_r and ρ is the mass density at r. The second equation describes the hydrostatic equilibrium in terms of the internal pressure and the gravitational force, both

acting in opposite directions:

$$\frac{\partial P}{\partial M_r} = \frac{GM_r}{4\pi r^4}, \tag{3.2}$$

such that G is the gravitational constant, and P the pressure. Now, for the star to be stable it is also necessary that the energy emitted from the stellar surface in a given time t is compensated by the energy generated in its center. Let L_r be the luminosity of a shell of mass M_r, ϵ_n the thermonuclear energy generation, C_p the specific heat at constant pressure, T the temperature, P the pressure, and ϵ_ν the energy loss by neutrino emission, then

$$\frac{\partial L_r}{\partial M_r} = \epsilon_n - \epsilon_\nu - C_p\dot{T} + \frac{\delta}{\rho}\dot{P}, \tag{3.3}$$

with

$$\delta = -\left(\frac{\partial \ln \rho}{\partial \ln T}\right)_P. \tag{3.4}$$

The energy transport equation is given by

$$\frac{\partial T}{\partial M_r} = -\frac{GM_r T}{4\pi r^4 P} \cdot \nabla, \tag{3.5}$$

such that ∇ is the temperature gradient, either in radiative or convective regions, and is written as

$$\nabla = \left(\frac{\partial \ln T}{\partial \ln P}\right). \tag{3.6}$$

Finally, for each nuclear species i the equation of abundance variation due to nuclear reactions is

$$\frac{dY_i}{dt} = \rho N_A \left(- \sum_{j} Y_i Y_j \langle \sigma \nu \rangle_{ij} + \sum_{l} Y_l Y_k \langle \sigma \nu \rangle_{lk} - Y_i \lambda_i(\beta) + Y_m \lambda_m(\beta), \right) \quad (3.7)$$

where N_A is Avogadro's number, ρ is the mass density, Y_i is the ratio of the number of nuclei of species i to the total number of nucleons in the system, and $\langle \sigma \nu \rangle$ is the reaction rate per particle pair. The first term on the right hand side represents the two-body reactions destroying the nucleus i, while the second term is a sum over all two-body reactions leading to nucleus i. The next two terms are the destruction and synthesis of i-nuclei via β-decays, respectively. Other pairs of terms should appear in the equation above. For example, three-body reactions, though rare, need to be considered as well; probably the most important example is the triple α reaction nucleosynthesizing ^{12}C. A photon dissociation term is considered important in some cases as well.

3.2 Nuclear reaction mechanisms and their rates

Equations 3.3 and 3.7 probably represent the most important link between stellar astrophysics and nuclear physics. Both imply the abundances of different nuclear species and therefore, the probability of synthesizing a specific type of nucleus in a stellar environment. This probability is quantified by the reaction rate per pair of particles $\langle \sigma \nu \rangle$.

Imagine a gas of particles a with a density N_a and particles b with a density N_b. We define the reaction rate per unit volume r as the product of σN_b with the flux of particles a $v N_a$, such that σ is the reaction cross section of particles a and

b and v their relative velocity, i.e.

$$r = N_a N_b v \sigma. \tag{3.8}$$

The relative velocity of particles in a gas is described by a distribution so the rate needs to be averaged over v. In general the reaction cross section is energy dependent, so we write

$$r = N_a N_b \langle v \sigma(v) \rangle, \tag{3.9}$$

such that

$$\langle v \sigma(v) \rangle = \int_0^\infty \sigma(v) \phi(v) v \, dv. \tag{3.10}$$

For the special case of a threshold for the reaction at positive energies the lower limit of the integral is replaced by the velocity at threshold. The velocities in stellar AGB and Wolf-Rayet environments are described by a non degenerate gas with a Maxwell-Boltzmann distribution, and with $E = mv^2/2$, we write the expression for the rate as

$$\langle v \sigma(v) \rangle = \left(\frac{8}{\pi \mu} \right)^{1/2} (kT)^{-3/2} \int_0^\infty \sigma(E) E \exp\left(-\frac{E}{kT} \right) dE, \tag{3.11}$$

such that k is Boltzmann's constant and μ is the reduced mass.

The cross section measurement (or theoretical prediction, in the worst case scenario) involves a good part of work efforts in nuclear astrophysics. In particular, chapter 5 of this work is dedicated to the determination of the cross section. Approximations to the reaction rate are very useful, though. For example, relative to the energy dependence of the cross section the reaction rate can be of three

different types [100], i.e.

$$\langle v\sigma(v)\rangle = \langle v\sigma(v)\rangle_{nr} + \langle v\sigma(v)\rangle_r + \langle v\sigma(v)\rangle_c, \tag{3.12}$$

such that "nr" labels the non-resonant part of the rate; it dominates at the lowest energies, where it is not likely to find resonances in the cross section. The term $\langle v\sigma(v)\rangle_r$ is the resonant part of the rate and in this region the cross section shows well isolated resonances. Finally, $\langle v\sigma(v)\rangle_c$ stands for the continuumn term, where the density of resonances per energy interval D is high ($D > 10MeV^{-1}$ [84]).

Let us concentrate in the case of a reaction between two charged particles. One of the reasons the determination of the cross section at stellar temperatures is an interesting problem is the fact that Coulomb repulsion is extremely strong to allow nuclear reactions to happen frequently, thus giving values of the cross section sometimes too tiny to be measured. The energy dependence of the cross section was examined for the first time for the case of alpha decay by George Gamow [35], who found that the probability P that a pair of charged particles would overcome the Coulomb barrier can be written as

$$P \sim \exp(-2\pi\eta) \sim \exp(-(E_G/E)^{1/2}), \tag{3.13}$$

with

$$\eta = \frac{Z_1 Z_2 e^2}{\hbar v}, \tag{3.14}$$

$$E_G = 2\mu(\pi\eta v)^2, \tag{3.15}$$

Z_1 and Z_2 the atomic numbers of the particles, $\hbar$ the reduced Planck constant, v the relative velocity of the particles, and e the proton charge. On the other hand,

the cross section should be proportional to the effective geometrical area $\pi\lambda^2$ seen by the particle pair during the collision (see [94] for further details), such that

$$\sigma \sim \pi\lambda^2 \sim \left(\frac{1}{p}\right)^2 \sim \left(\frac{1}{E}\right) \tag{3.16}$$

where p is the linear momentum and λ the de Broglie wavelength. In this way we may write

$$\sigma(E) = \frac{S(E)}{E}\exp(-2\pi\eta), \tag{3.17}$$

with $S(E)$ known as the astrophysical S-factor. By substituting equation 3.17 into equation 3.11 we finally get

$$\langle\sigma v\rangle = \left(\frac{8}{\pi\mu}\right)^{1/2}(kT)^{-3/2}\int_0^\infty S(E)\exp\left(-\frac{E}{kT}-\frac{b}{E^{1/2}}\right)dE. \tag{3.18}$$

Writing the cross section as in equation 3.17 is just a matter of convenience as the S-factor has no physical meaning [87]; nevertheless it is very useful in removing the strong energy dependence of the cross section —usually spanning several orders of magnitude in a small energy region— thus enhancing the visualization of the resonant nature of the reaction.

3.2.1 The non-resonant reaction rate

In general $S(E)$ can be written as a Taylor series around an energy E_0; in the special case of a non-resonant reaction $S(E)$ is a constant given by $S_0 = S(E_0)$. Taking S_0 out of the integral in equation 3.18 the reaction rate per particle pair concept can be put in a more practical context for stellar astrophysics. The first factor in the integrand of equation 3.18 represents the probability densitiy that two particles would collide with each other at an energy E, and is given by a

27

Maxwell-Boltzmann distribution. On the other hand the second factor in the integrand gives the probability that once a pair of particles have encountered each other at an energy E they would penetrate the Coulomb barrier and be thrown into a reaction channel. The product of the integrands defines a region of energy where given a gas with temperature $E = kT$ the reactions between particles a and b are likely to take place. The region is known as the "Gamow window".

The concept of the Gamow window can be extended to reaction regimes different from the non-resonant mechanisms by assuming $S(E) = S_0$. In this way the relevance of a cross section in an astrophysical environment can be assesed before solving and evolving the set of equations for stellar structure and evolution.

3.2.2 The resonant reaction rate

For case of an isolated sharp resonance the cross section can be written as

$$\sigma(E) = \frac{\lambda^2}{4\pi} \frac{2J+1}{(2I_1+1)(2I_2+1)} \frac{\Gamma_{in}\Gamma_{out}}{(E-E_R)^2 - (\Gamma/2)^2}, \tag{3.19}$$

where λ is the de Broglie wavelength, E_R is the energy of the resonance J is the spin of the compound state, I_1 and I_2 are the spins of the colliding nuclei, Γ_{in} and Γ_{out} are the partial widths for the entrance and exit channel, respectively, and Γ is the total width. The total width Γ is defined as the sum of the partial widths

$$\Gamma = \sum_i \Gamma_i, \tag{3.20}$$

and

$$\Gamma\tau = \hbar, \tag{3.21}$$

28

where τ is the lifetime of the state at E_R. On the other hand the partial widths Γ_i are a product of the penetration factor P and the squared matrix element γ of the transition between the channel and the compound state, i.e.

$$\Gamma_i = 2P\gamma^2. \tag{3.22}$$

Substituting in equation 3.11

$$\langle \sigma v \rangle = \left(\frac{8}{\pi\mu} \right)^{1/2} (kT)^{-3/2} \int_0^\infty \frac{\lambda^2}{4\pi} \omega \frac{\Gamma_{in}\Gamma_{out}}{(E - E_R)^2 - (\Gamma/2)^2} E \exp\left(-\frac{E}{kT} \right) dE, \tag{3.23}$$

where the spin factor ω is defined as

$$\omega = \frac{2J + 1}{(2I_1 + 1)(2I_2 + 1)}. \tag{3.24}$$

Assuming $E \exp(-E/kT)$ changes very little in the resonance region we can write

$$\langle \sigma v \rangle = \left(\frac{8}{\pi\mu} \right)^{1/2} \frac{\lambda^2}{4\pi} \omega E_R \frac{\Gamma_{in}\Gamma_{out}}{(kT)^{3/2}} \exp\left(-\frac{E_R}{kT} \right) \int_0^\infty \frac{dE}{(E - E_R)^2 - (\Gamma/2)^2}, \tag{3.25}$$

such that the integral evaluates to $2\pi/\Gamma$. Let us define $\gamma = \Gamma_{in}\Gamma_{out}/\Gamma$, so

$$\langle \sigma v \rangle = \omega\gamma \left(\frac{2\pi}{\mu kT} \right)^{3/2} \hbar^2 \exp\left(-\frac{E_R}{kT} \right). \tag{3.26}$$

The case of several resonances can be approximated by summing over various terms of the form 3.26, i.e.

$$\langle \sigma v \rangle_R = \left(\frac{2\pi}{\mu kT} \right)^{3/2} \hbar^2 \sum_i (\omega\gamma)_i \exp\left(-\frac{E_R}{kT} \right)_i. \tag{3.27}$$

Most of the rates described in the last section of this chapter were calculated using

29

the expression for $\langle \sigma v \rangle_R$ given above.

3.2.3   The rate in the continuum

At energies where the density of states is high ($D > \Gamma$) the sum over resonances can be approximated by an integral over E_R [100]. The rate is then obtained by retaining the most energy-dependent terms. The rate in the continuum can still be written as a sum of two terms:

$$\langle \sigma v \rangle_c = \langle \sigma v \rangle_{uc} + \langle \sigma v \rangle_{sc}. \tag{3.28}$$

The first term corresponds to the "unsaturated continuum" rate and here the entrance channel partial width Γ_{in} is small compared to the total width Γ. The second term is the "saturated continuum" term, where the penetration factor (equation 3.13) is large enough to allow the incoming partial width approximate Γ, the total width. In general the functional dependence of the continuum rates with energy is as follows:

$$\langle \sigma v \rangle_{uc} = F T_9^{-2/3} \exp[-\tau_c T_9^{-1/3} - (T_9/T_u)^2] \tag{3.29}$$

and

$$\langle \sigma v \rangle_{sc} = H \exp[-11.605 E_c/T_9], \tag{3.30}$$

such that T_9 is the temperature in GK, and E_c, F, H, τ_c, and T_u are constants.

The rate for the $^{19}F(\alpha, p)^{22}Ne$ reaction was first calculated in 1969 by Robert Wagoner [100] as discussed in Chapter 1, with the two equations above by assuming that the compound ^{23}Na has a high density of states at excitation energies above the alpha threshold (10.467 MeV) and therefore falls in his definition of

rate in the continuum. It is relevant to mention that Wagoner put limits to the validity of his rate ($0.8 \leq T_9 \leq 3.0$) and that later on the limits were ignored in publications that eventually led to the value published in Caughlan and Fowler's 1988 compilation of rates [15].

3.3 Reaction chain involving fluorine nucleosynthesis in AGB and Wolf-Rayet stars

It was discussed in Chapter 2 the mechanism of fluorine nucleosynthesis in various environments. A summary of the reactions involved in the nucleosynthesis process in AGB and Wolf-Rayet stars is as follows. Starting from ^{14}N, a product of the CNO cycle and the abundant ^4He nuclei in these environments,

$$^{14}N(\alpha, \gamma)^{18}F(\beta^+)^{18}O(p, \alpha)^{15}N(\alpha, \gamma)^{19}F. \tag{3.31}$$
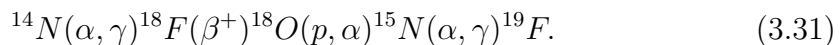
Protons are produced through the reaction

$$^{14}N(n, p)^{14}C, \tag{3.32}$$

and the required neutrons come from

$$^{13}C(\alpha, n)^{16}O. \tag{3.33}$$

Competing with the previous chain of reactions the

$$^{14}C(\alpha, \gamma)^{18}O(\alpha, \gamma)^{22}Ne. \tag{3.34}$$

and the ^{15}N poison reaction

$$^{15}N(p,\alpha)^{12}C, \tag{3.35}$$

would reduce the fluorine yields.

Destruction of ^{19}F could occur by proton, alpha, or neutron capture via

$$^{19}F(p,\alpha)^{16}O \tag{3.36}$$

$$^{19}F(n,\gamma)^{20}F, \tag{3.37}$$

and

$$^{19}F(\alpha,p)^{22}Ne. \tag{3.38}$$
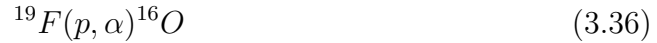
A comparison between the rates for the reactions responsible for destruction of fluorine is shown in figure 3.1. In the last chapter of this work we shall discuss the importance of these reactions. From a first glance one would improvise that in the temperature range of relevance to this work ($0.1 < T_9 < 0.3$) the $^{19}F(\alpha,p)^{22}Ne$ reaction is of marginal importance to the destruction of fluorine. However, the relative abundances of protons, alphas, and neutrons needs to be taken into account as well.

3.4   Summary of reaction rate studies

There has been a considerable effort and improvement in the determination of the nuclear reaction rates over the last few years since the early ^{19}F nucleosynthesis studies. In particular new measurements on key reactions such as $^{14}\text{C}(\alpha,\gamma)^{18}\text{O}$, $^{14}\text{N}(\alpha,\gamma)^{18}\text{F}$, $^{15}\text{N}(\alpha,\gamma)^{19}\text{F}$, $^{18}\text{O}(\alpha,\gamma)^{22}\text{Ne}$ provided new information on low energy resonances either ignored or only insufficiently included in previous estimates. The
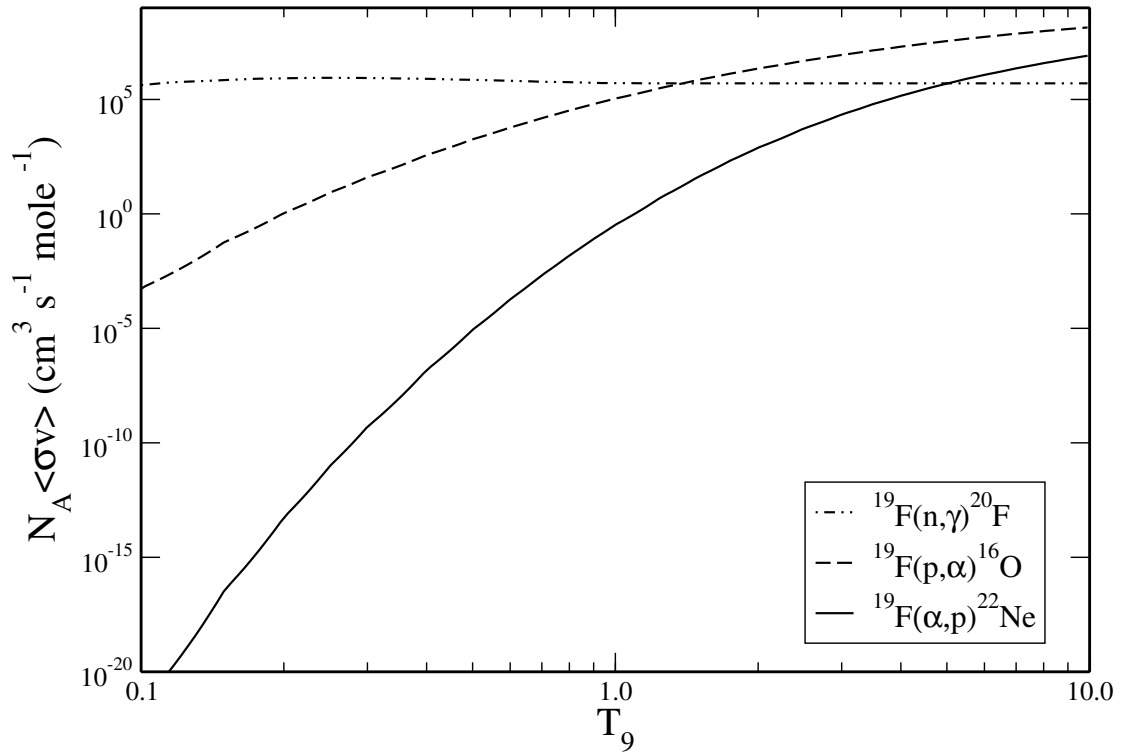
Figure 3.1. The reaction rates for the three main mechanisms responsible for destroying fluorine in AGB stars. The rates are from Jorrisen and Goriely's NETGEN compilation[55]

results of all these studies will be summarized and discussed in this section. New experimental results will be also soon available for the $^{13}C(\alpha, n)^{16}O$ stellar neutron source reaction [48]. There has not been much improvement in the $^{18}O(p,\alpha)^{15}N$ rate and there has been very little experimental effort in the study of $^{19}F(\alpha, p)^{22}Ne$. A tabulation of some of the rates used in this work can be found in appendix 1 and in [97]; the effect their uncertainties has in the synthesis of fluorine in AGB stars has been thoroughly evaluated in [71].

3.4.1 The reaction rate of $^{13}C(\alpha, n)^{16}O$

For the $^{13}C(\alpha, n)^{16}O$ reaction, the rate from Drotleff et al.[27] and Denker et al.[25] is about 50% lower than the rate recommended by NACRE[5] in the temperature range of interest $(0.1 < T/GK < 0.3)$. Recent $^{13}C(^{6}Li,d)$ α-transfer studies by Kubono et al.[64] suggest a very small spectroscopic factor of $S_\alpha = 0.01$ for the subthreshold state at 6.356 MeV. This indicates that the high energy tail for this state is negligible for the reaction rate in agreement with the present lower limit. However, a detailed re-analysis by Keeley et al.[60] of the transfer data leads to significant different results for the spectroscopic factor of the subthreshold state $S_\alpha = 0.2$ which would imply good agreement with the value used here, which is lower than the rate suggested by NACRE. This situation requires further experimental and theoretical study. A re-evaluation of the rate based on new experimental results, including elastic scattering data [49], has been performed by Heil[48] and will be published soon.

3.4.2 The reaction rate of $^{14}C(\alpha, \gamma)^{18}O$

The reaction $^{14}C(\alpha, \gamma)^{18}O$ has been studied experimentally in the energy range of 1.13 to 2.33 MeV near the neutron threshold in the compound ^{18}O by Görres et al.[43]. The reaction rate is dominated at higher temperatures by the direct capture and the single strong 4^+ resonance at E_{cm}=0.89 MeV. Towards lower temperatures, which are of importance for He shell burning in AGB stars, important contributions may come from the 3^- resonance at E_{cm}=0.176 MeV (E_x=6.404 MeV) an a 1^- subthreshold state at E_x=6.198 MeV. It has been shown in detailed cluster model simulations that neither one of the two levels is characterized by a pronounced α cluster structure [26]. The strengths of these two contributions are unknown and have been estimated by Buchmann et al.[13] adopting an α spectroscopic factor of Θ_α^2=0.02, 0.06 for the 6.404 MeV and the 6.198 MeV states, for determining the 0.176 MeV resonance strength and the cross section of the high energy tail of the subthreshold state. While the value for the 6.404 MeV state is in agreement with the results of a $^{14}C(^6Li,d)^{18}O$ α-transfer experiment [19] the value for the 6.2 MeV state appears rather large since the corresponding α transfer was not observed. This reflects lack of appreciable α strength in agreement with the theoretical predictions. We therefore adopted an upper limit for the spectroscopic factor of this resonance of Θ_α^2=0.02. The upper limit for the reaction rate is based on the experimental data [43] plus the low energy resonance contributions calculated from the upper limit for the α spectroscopic factor. For the recommended reaction rate we adopted a considerably smaller spectroscopic factor Θ_α^2=0.01 for calculating the $\omega\gamma$ strength of the 0.176 MeV resonance. In this we followed the recommendations by Funck and Langanke[34]. The lower limit of the reaction rate neglects the contribution of this resonance altogether and corresponds directly to
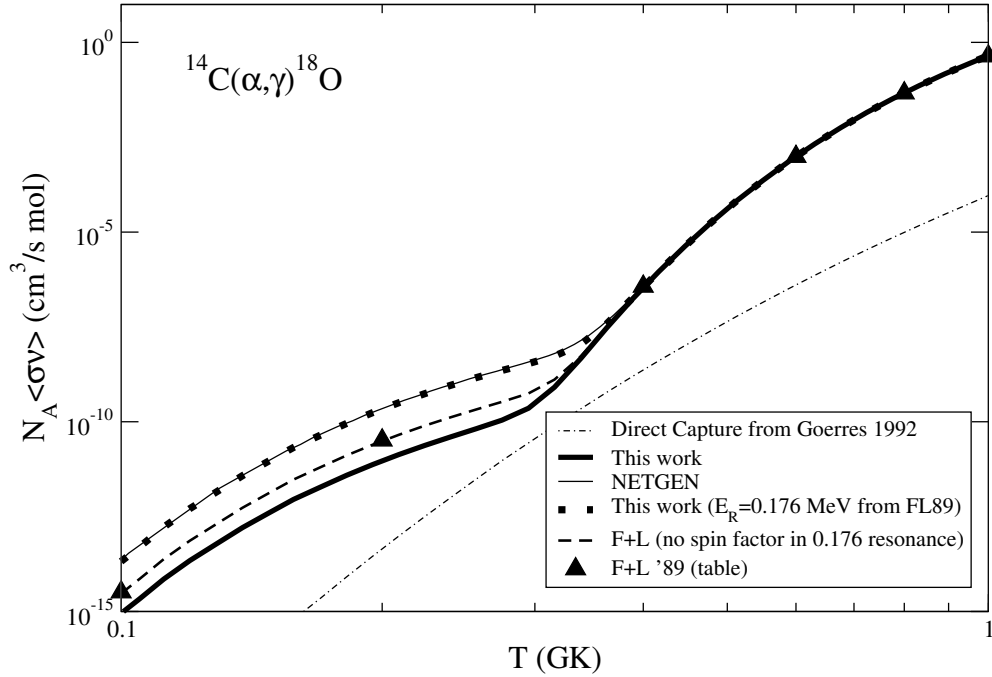
Figure 3.2. Rates for the $^{14}C(\alpha, \gamma)^{18}O$ reaction. The rate obtained in this work is represented by the thick continuous black line and is close to one order of magnitude different from the NETGEN rate (thin continuous line). The triangles are Funck and Langanke's values from Table 1 of their paper. Following their indications to get the rate, we obtained the rate represented by the dotted line, in perfect agreement with NETGEN's. We were able to reproduce (thick dashed line) their table by removing the spin factor to the strength of the resonance at 0.176 MeV

the experimental results [43]. It should be noted however that the uncertainty for the resonance strength and therefore its contribution to the reaction rate is up to five orders of magnitude.

Interesting is to point out the difference between the rate listed in the NET-GEN compilation [55] (based on Funck and Langanke's rate for this reaction) and our rate; a problem is made evident when after trying to explain the order of magnitude difference (see figure 3.2) one realizes that it is not possible to re-

produce Funck and Langanke's table from their own recipe. However, with their method we were able to reproduce NETGEN's rate; this pointed out to an inconsistency in Funck and Langanke's recipe for getting the rate; and that is the case indeed. The problem is the strength $\omega\gamma$ of the resonance at 0.176 MeV; they provide the relation $\omega\gamma = 7\Gamma_\alpha$, such that Γ_α is the alpha width and 7 the spin factor. They assume a dimensionless spin factor $\Theta_\alpha^2 = 0.01$ and get an alpha width $\Gamma_\alpha = 2.87 \times 10^{-18}$ MeV. If one removes the spin factor then one can reproduce their table; this means that what they list as Γ_α is in fact the strength $\omega\gamma$ itself. The typo led Alain Jorrisen and Stéphane Goriely to the incorrect evaluation of the rate in NETGEN. It would be interesting to find out what is the effect of an order of magnitude variation in this rate for all the works using NETGEN's values under $T = 0.3$ GK. Now, one can ask how relevant is this reaction; for starters the reaction is at the base of the chain leading to one of the two sources of neutrons for the s-process, i.e.

$$^{14}C(\alpha,\gamma)^{18}O(\alpha,\gamma)^{22}Ne(\alpha,n)^{25}Mg. \qquad (3.39)$$
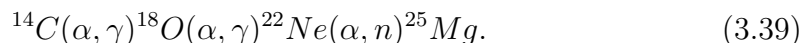
3.4.3   The reaction rate of ^{14}N$(\alpha,\gamma)^{18}$F

The low energy resonances in ^{14}N$(\alpha,\gamma)^{18}$F have recently successfully been measured by [41]. Previous uncertainties about the strengths of these low energy resonances were removed. Due to these results the reaction rate is reduced by about a factor of three compared to NACRE.

3.4.4   The reaction rate of ^{15}N$(\alpha,\gamma)^{19}$F

The reaction rate of ^{15}N$(\alpha,\gamma)^{19}$F is the same as NACRE's. The rate is dominated by the contribution of three low energy resonances. The resonance strengths

are based on the analysis of De Oliveira[22]. It should be noted though that there were several recent experimental studies which point towards a significantly higher reaction rate. De Oliveira et al.[23] themselves already suggested higher resonance strengths than given in their earlier paper. Direct α-capture measurements of the two higher energy states by Wilmes et al.[102] also indicate higher strengths. A recent indirect α-transfer analysis to the three resonance levels by [31] does suggest even higher values for the resonance strengths. Altogether the reaction rate of ^{15}N$(\alpha, \gamma)^{19}$F might be underestimated by a factor of five.

3.4.5 The reaction rate of ^{15}N$(p, \alpha)^{12}$C

The ^{15}N$(p, \alpha)^{12}$C reaction has been investigated by Schardt et al.[88], Zyskind et al.[107], and more recently by Redder et al.[85] at $E_p(\text{lab}) = 78$-810 keV. These results were summarized and compiled by NACRE. The reaction rate at $T_9 \sim 0.2$ is dominated by the $J^\pi = 1^-$ resonance at $E_p = 334$ keV. However, contributions from other three resonances at 1027, 1639, and 2985 keV have been included as well.

3.4.6 The reaction rate of ^{18}O$(\alpha, \gamma)^{22}$Ne

The $^{18}O(\alpha, \gamma)^{22}$Ne is of interest for the discussion of the ^{19}F production in AGB stars since it competes with the ^{18}O$(p,\alpha)^{15}$N process. A strong rate might lead to a reduction in the ^{19}F production. The reaction rate of $^{18}O(\alpha, \gamma)^{22}$Ne has been last summarized and discussed by Käppeler et al.[57] and by the NACRE compilation. The main uncertainties result from the possible contributions of low energy resonances which have been estimated on the basis of α-transfer measurements by [36]. A recent experimental study of $^{18}O(\alpha, \gamma)^{22}$Ne by Dababneh[20]

and Görres[42] led to the first successful direct measurement of the postulated low energy resonances at 470 keV and 566 keV thus reducing to 33% the previous uncertainty of about a factor of 30 given by NACRE at the temperature of interest which was given by taking the previously available experimental upper limit for the 470 keV resonance strength [36]. Not measured still is the 218 keV resonance which is expected to dominate the rate at temperatures of T≤0.1 GK, well below the temperature in typical He-burning conditions. The resulting reaction rate is in very good agreement with the previous estimate by [57] which was used for the calculations of ^{19}F production.

3.4.7 The reaction rate of ^{19}F$(\alpha, p)^{22}$Ne

The reaction rate of ^{19}F$(\alpha, p)^{22}$Ne is one of the most important input parameters for a reliable analysis of ^{19}F nucleosynthesis at AGB stars conditions. Yet, there is only very little experimental data available about the ^{19}F$(\alpha, p)^{22}$Ne reaction cross section at low energies. Experiments were limited to the higher energy range above E_α=1.3MeV [65]. As discussed previously, Caughlan and Fowler [15] suggested a rate which is based on a simple barrier penetration model previously used by [100]. This reaction rate is in reasonable agreement with more recent Hauser-Feshbach estimates assuming a high level density and has therefore been used in most of the previous nucleosynthesis simulations.

The applicability of the Hauser-Feshbach model, however, depends critically on the level density in the compound system [84]. We analyzed the level density in the compound ^{23}Na above the α-threshold of Q_α=10.469 MeV as compiled by [29]. The typical level density is $\approx$0.02 keV^{-1}. This level density is confirmed directly for the ^{19}F$(\alpha, p)^{22}$Ne reaction channel by direct studies from [65] at resonance
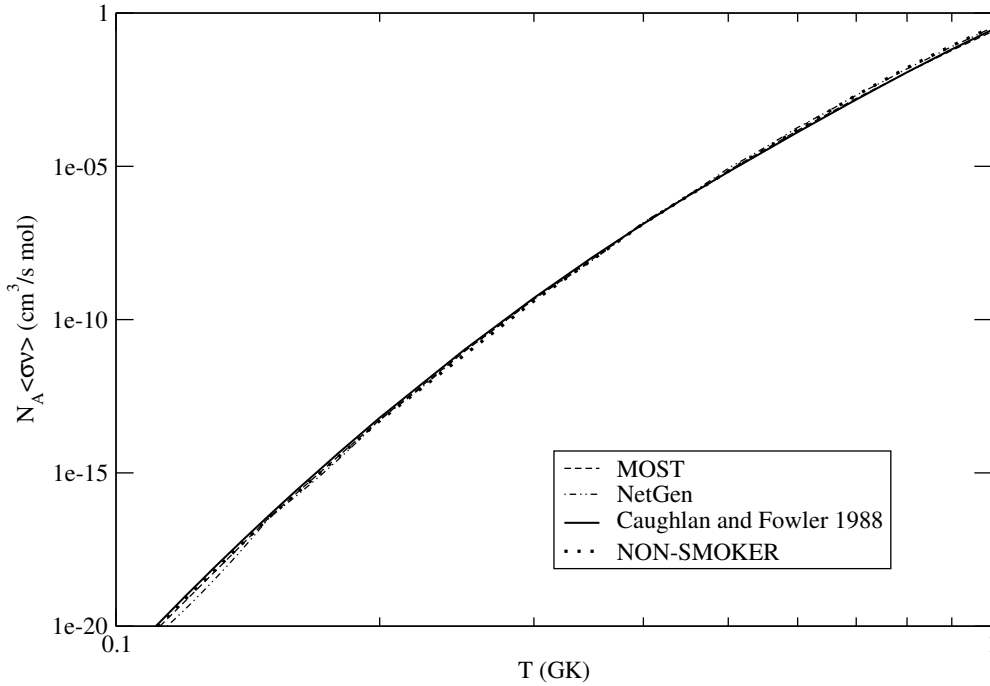
Figure 3.3. Comparison between some ^{19}F$(\alpha,p)^{22}$Ne rates available.
They all were calculated in a fundamentally equivalent way. MOST is
Goriely's rate [38], NetGen is Jorrisen's rate [55], Non-smoker
corresponds to Rauscher's [82] and [83]. Caughlan and Fowler's rate has
been discussed previously in this work.

energies above 1.5 MeV and further confirmed by this work. This low resonance
density translates into an averaged level spacing of D$\approx$50 keV which is consider-
ably larger than the average resonance width of $\Gamma \approx$8 keV in this excitation range.
Based on these estimates the requirement of $D \leq \Gamma$ for the applicability of the
Hauser-Feshbach approach [84] is not fulfilled. The reaction rate for ^{19}F$(\alpha,p)^{22}$Ne
therefore needs to be determined from determining the strengths $\omega\gamma$ for the single
resonances.

Some of the rates available to date are shown in figure 3.3. They more or less
are consistent with each other as all are based on treatments of the compound in

the continuum.

CHAPTER 4

MEASUREMENT OF THE $^{19}F(\alpha,p)^{22}Ne$ REACTION

Depletion of ^{19}F by alpha capture occurs through a resonant process involving the formation of the ^{23}Na compound nucleus in a region of high density of states. These resonant states can proceed to the ground (p_0 protons) and first excited state (p_1 protons) of ^{22}Ne. Possible scenarios for studying the $^{19}F(\alpha,p)^{22}Ne$ reaction include the detection of both p_0 and p_1 protons. An alternate approach consists of the measurement of the p_1 channel by the detection of the γ transition from the first excited state (2^+) to the ground state (0^+) of ^{22}Ne, i.e. $^{19}F(\alpha,p_1\gamma)^{22}Ne$. (See figure 4.1).

In this chapter the experimental method used to investigate the $^{19}F(\alpha,p)^{22}Ne$ reaction is described. Section 4.2 includes a description of the measurement of the gamma yield curve from the $^{19}F(\alpha,p_1\gamma)^{22}Ne$ process at beam energies between 1.1 and 1.9 MeV. In section 4.2 we describe the measurement of the p_0 and p_1 yield curves from 1.2 MeV to 1.9 MeV of beam energy; evaporated transmission targets were used and the lowest beam energy reached was limited because of target unstability reasons. Finally, section 4.3 describes the method developed for obtaining a yield curve for both the p_0 and p_1 channels from 0.8 MeV to 1.4 MeV of beam energy with a fluorine target implanted on a thick substrate. Most likely the fluorine targets were the most important factor in determining the success of the experiments performed; special attention is given to the process of their
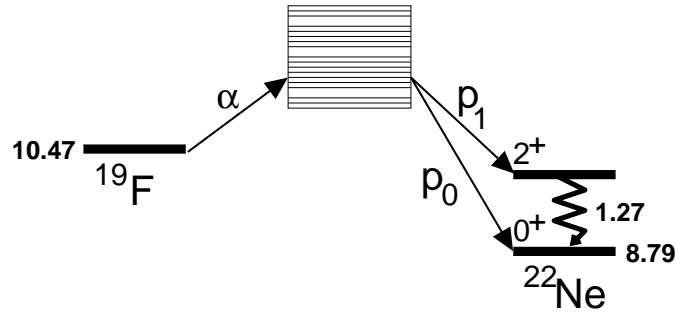
Figure 4.1. Energy level scheme for the $^{19}F(\alpha, p)^{22}Ne$ reaction. The entrance channel ($\alpha + ^{19}$F) has a Q-value of 10.47 MeV with respect to the ground state of the compound ^{23}Na. The compound can then proceed either to the $p_0 + ^{22}$Ne exit channel (leaving ^{22}Ne in the ground state) or to the $p_1 + ^{22}$Ne channel (leaving ^{22}Ne in its first excited state). The emission of a 1.27 MeV photon from the decay of the first excited state (2^+) to the ground state (0^+) of ^{22}Ne can also be observed. The grided square above ^{23}Na represents the energy region studied in this work.

1. SNICS Ion Source
2. HIS Ion Source
3. FN Van de Graaff Accelerator
4. Gamma Spectroscopy Beamline
5. Spectrograph Beam Line
6. R2D2 Beam Line (1 m scattering chamber)
7. Weak Interaction Beam Line
8. RNB Beam Line
9. Neuton Detection Wall
10. Conference Room
11. Accelerator Control Consoles
12. ECR Ion Source Test Setup
13. KN Van de Graaff Accelerator
14. JN Van de Graaff Accelerator
15. ORTEC Scattering Chamber
16. Windowless Gas Target Beam Line
17. Gamma Table
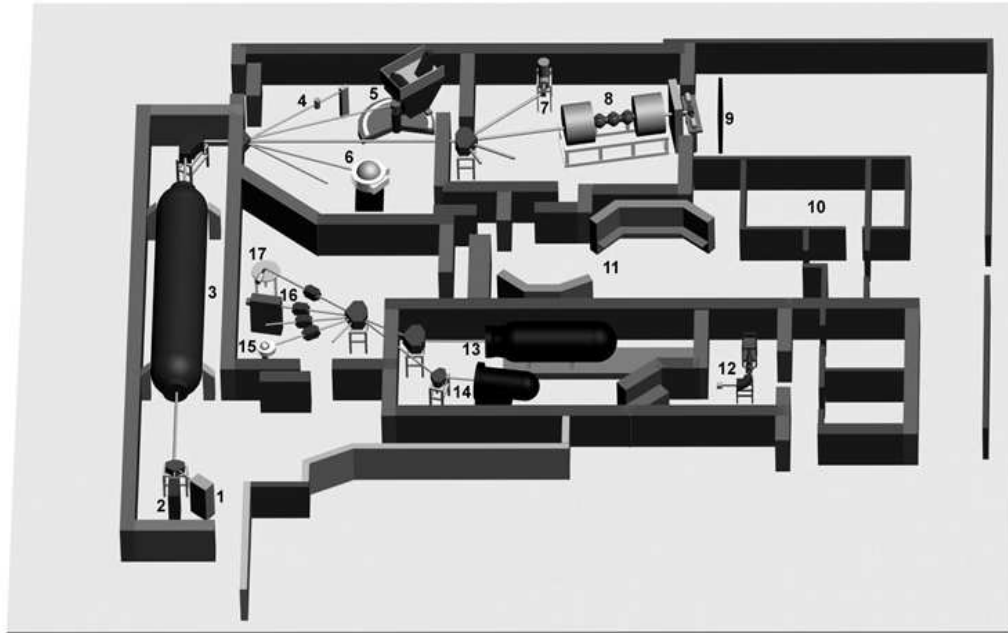
Figure 4.2. The Nuclear Structure Laboratory at the University of Notre Dame. (Plan courtesy of the Nuclear Structure Laboratory.)

production. All the experiments were performed at the facilities available in the Nuclear Structure Laboratory at the University of Notre Dame. A floormap of the laboratory is shown in figure 4.2.

4.1 The gamma-ray experiment

The first set of experiments performed were the measurement of the gamma-ray yield from the p_1 channel from 1.1 to 1.9 MeV of beam energy [96].

4.1.1 Preparation of evaporated targets

The preparation of targets for nuclear reaction experiments is a complex process that usually involves several steps. An ideal target should in principle be stable and show no deterioration when bombarded with high intensity beams. Also, it should not produce radiation that would interfere with the measurement of the reaction of interest.

For the gamma-ray experiment an evaporated target was used. The substrate consisted of a 1.5 inch side square cut from a 99.5% tantalum sheet with a thickness of 0.01 in. Tantalum is an excellent substrate as it has a very high melting point temperature (3016 ^oC), making it stable at high beam intensies. Moreover, tantalum has a very high thermal conductivity (0.575 $W/cm \cdot K$ at 1 atm and 25^oC); this means that the substrate can be water-cooled very efficiently.

The evaporation of a thin film on a substrate requires a vacuum chamber in which the material to be deposited is heated above its melting temperature. Due to the high vapor pressure the material is deposited as a thin film on a surface where it condenses [6]. In particular, calcium fluoride (CaF_2) was our material of choice for preparing the targets. CaF_2 is a crystal with a melting point temperature of 1418^oC so, to avoid amalgamation, any material used to support it during the evaporation process needs to have a significantly higher melting point. Tungsten has the highest melting temperature of all metals; a boat of this material was used both as a holder and as a resistive heater to evaporate the CaF_2 powder. (A scheme of the evaporation chamber is shown in figure 4.3). After cleaning thoroughly with alcohol and paper towels, the tantalum substrate was placed 20 cm above the tungsten boat. Right next to the target a film thickness monitor was placed at about the same distance from the CaF_2 powder. A rough estimate
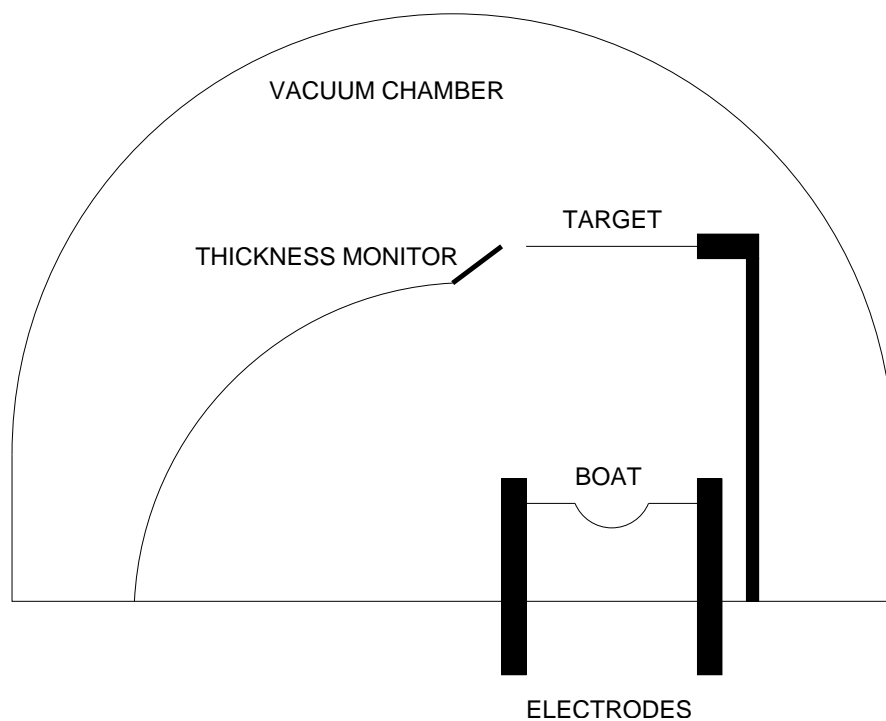
Figure 4.3. The evaporation chamber. It consists of a crystal bell that rests on and can be lifted from a stainless steel plate serving as an evaporation table.

of the film thickness was obtained during the evaporation process.

Vacuum in the chamber was achieved with both a mechanical and a diffusion pump. (See fig. 4.4). The mechanical pump was used both as a roughing pump and as a backing for the diffusion pump. A vacuum of some 1×10^{-7} Torr was achieved below the high vacuum valve 1 to 2 hours after the diffusion pump was turned on. Filling the liquid nitrogen (LN_2) deposit further improved the vacuum.

The tungsten boat was heated with a high current power supply connected to electrodes outside the chamber (see figure 4.3). While slowly increasing the current in the potentiometer of the power supply, the thickness of the film was
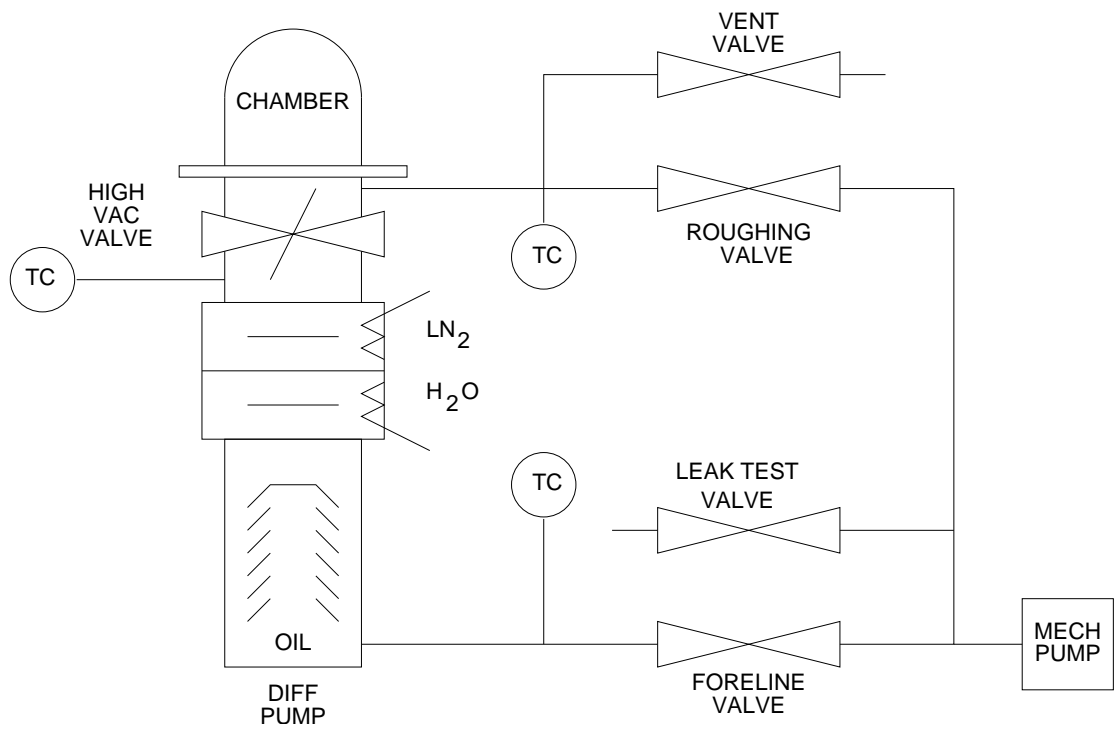
Figure 4.4. Vacuum system of the evaporator. The vacuum system and
the chamber are connected through an opening on the plate.

monitored for changes. When the thickness monitor readout started to change, the current was not increased further. The film thickness monitor is a quartz crystal that oscillates at a frequency of 5 MHz when a current is applied to it. The frequency of oscillation decreases with the increasing mass being deposited on its surface; the change in frequency is proportional to the surface density of the deposited film.

Two targets with a thickness of 25 keV each were prepared simultaneously by evaporating calcium fluoride onto tantalum sheets. While one target was used in the experiment the other remained wrapped in aluminum foil. Tantalum was selected as a substrate for evaporating the thin target layer for its high melting temperature and, therefore, its stability at high beam currents.

4.1.2 Energy calibration of the photon detectors

The main assumption for calibrating the energy in the photon detectors was a linear behaviour of the electronic signal amplitude as a function of the energy deposited by photons in the crystal in the $1173 \leq E_\gamma/keV \leq 1333$ region.

A ^{60}Co radioactive source was placed at 10 cm from the detector crystal and an energy spectrum was taken. ^{60}Co β^--decays to ^{60}Ni by populating the 4^+ state at 2506 keV in ^{60}Ni, which then decays to the 2^+ state at 1333 keV by emitting an 1173 keV $\gamma-$ray in cascade with the subsequent 2^+ to the 0^+ ground state 1333 keV γ-ray[10]. The plot of the $\gamma-$ray energy versus the signal amplitude(channel number) for the full energy peaks defined a straight line that was used for energy calibration. The photons from the $^{19}F(\alpha, p_1\gamma)^{22}Ne$ reaction have $E_\gamma =$1274 keV, right in between the two ^{60}Co lines.

4.1.3 Efficiency calibration of the photon detectors

The efficiency ϵ_y was measured by placing a ^{60}Co source of known activity at the target position. A spectrum was taken and values of ϵ_y were obtained for $E_\gamma =$1173 keV and 1332 keV.

The efficiency calibration with the ^{60}Co source was corrected for summing effects. Let A_1 and A_2 be the count rates measured for the peaks at 1173 keV and 1332 keV, respectively, N_0 the activity of the radioactive source, and ϵ_1 and ϵ_2 the corrected efficiencies at both energies, respectively. If the probability of detecting a gamma from the source anywhere in the spectrum is given by ϵ_T then

$$A_1 = N_0\epsilon_1 - N_0\epsilon_1\epsilon_T \tag{4.1}$$

$$A_2 = N_0\epsilon_2 - N_0\epsilon_2\epsilon_T \tag{4.2}$$

$$A_3 = N_0\epsilon_1\epsilon_2 \tag{4.3}$$

such that A_3 is the count rate for the summing peak [37]. The efficiencies obtained are 1.10×10^{-2} and 1.01×10^{-2} at 1173 and 1332 keV, respectively.

The yields used to determine the detector efficiencies were corrected for angular correlation effects (see [10] and [105]) as well. Let $w(\theta)$ be the probability per unit solid angle that two successive gammas are emitted from the source at an angle θ. An expansion of $w(\theta)$ [10] is given by

$$w(\theta) = 1 + \frac{1}{8}\cos^2(\theta) + \frac{1}{24}\cos^4(\theta), \tag{4.4}$$

characteristic of two successive quadrupole transitions with angular momenta $J_1 = 0$ $J_2 = 2$ $J_3 = 4$ and no parity change (electric quadrupole). For a derivation see the work by Yang in 1948[105]. As the detector has a finite size we define the

correction factor W by

$$W = \frac{\int_0^R 2\pi r w(\theta) dr}{\int_0^R 2\pi r dr},\qquad(4.5)$$

where R is the radius of the detector crystal (4 cm). Let θ be half the angle covered by the detector and x the distance from the center of the detector crystal to the radioactive source (20 cm), so $r = x\tan\theta$. We rewrite the numerator in equation 4.5 as

$$\int 2\pi r w(\theta) dr = \int 2\pi x^2 \tan\theta\, w(\theta) \sec^2\theta d\theta,\qquad(4.6)$$

with

$$dr = x\sec^2\theta d\theta,\qquad(4.7)$$

so $W = 1.09$.

The activity of the source N_0 in equations 4.1-4.3 was replaced by WN_0. The efficiencies corrected for angular correlation effects are 1.06×10^{-2} and 9.7×10^{-3} at 1173 and 1332 keV, respectively.

The radioactive source proved to be ideal for the calibration as the gamma produced by the $^{19}F(\alpha, p_1\gamma)$ reaction has an energy that falls between the ^{60}Co lines. At these gamma energies the relation

$$\log \epsilon = a(\log E) + b\qquad(4.8)$$

holds for the Ge detector used[80]. Here ϵ is the detection efficiency, E is the energy of the gamma, and a and b are constants. Therefore, the efficiency at 1274 keV can be interpolated to give 9.98×10^{-3}.
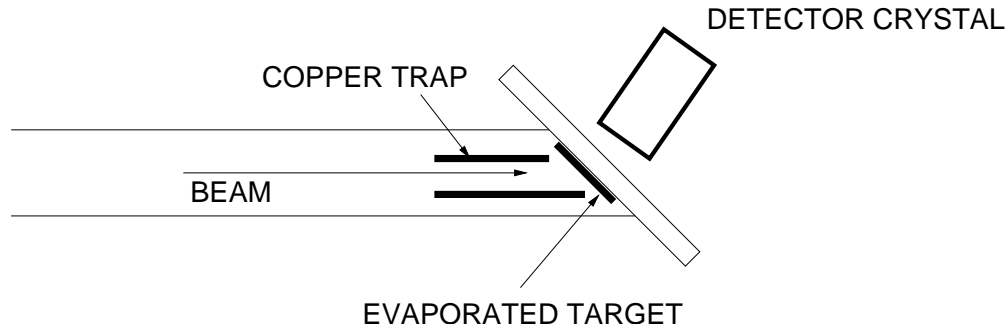
Figure 4.5. The 150 cm^3 scattering chamber used for the gamma-ray experiment. Both the target and its holder were tilted 45° with respect to the beam direction. The back of the target was water-cooled. The detector crystal was placed at 55° from the beam direction.

4.1.4   Experimental setup and procedure

A 150 cm^3 brass cylindrical scattering chamber (see figure 4.5) at the end of the 0° beam line of the KN accelerator was used for the experiment. The far end of the cylinder was tilted 45° from the beam direction and was both a target holder and a Faraday cup. The scattering chamber and the detector were shielded with lead bricks to prevent environment radiation from being registered. A liquid nitrogen-cooled copper trap was placed at the end of the beam line close to the scattering chamber and reduced carbon build up on the target. The trap was kept at -350 volts so electrons were suppressed from the beam as the current was integrated at the Faraday cup.

The experiment consisted of three parts. The first included the measurement of the reaction yield from 2009 keV to 1238 keV of alpha energy with a Ge detector. In the second stage a BGO scintillator was used to measure the reaction yield from 1700 keV to 1648 keV and from 1354 keV to 1150 keV of beam energy. Larger detection efficiency for the low yield at these energies made up for the loss

51

in energy resolution. The last stage included gamma detection with the same Ge detector and was used to scan several times through the resonances found in previous stages of the experiment. This allowed us to study the thickness and stability of the target. On the other hand, the 2 - 4 μA alpha beam was produced by the 4 MV KN Van de Graaff accelerator at Notre Dame. Typical spectra for both the BGO and the Ge detector experiments are shown in figure 4.6

4.1.5   Beam energy calibration

The beam energy was determined by monitoring the magnetic field at the center of the analyzing magnet with an NMR probe. The relation between the resonant frequency ν_{NMR} and the energy E of the analyzed particles is

$$\nu_{NMR} = k\sqrt{E}, \tag{4.9}$$

such that k is a constant.

The determination of k was done by scanning the 991.82 keV resonance in $^{27}Al(p,\gamma)^{28}Si$. The transition from the first 2^+ excited state (1778.6 keV) to the 0^+ ground state of ^{28}Si was observed with a germanium detector. By comparing the frequency at which the resonance was positioned with the known energy, $k = 213.32$ was determined. The relation between k for protons and alphas is given by

$$\frac{k_\alpha}{k_p} = \sqrt{\frac{m_\alpha}{m_p}}, \tag{4.10}$$

such that m_α and m_p are the masses of the alpha and the proton, respectively.
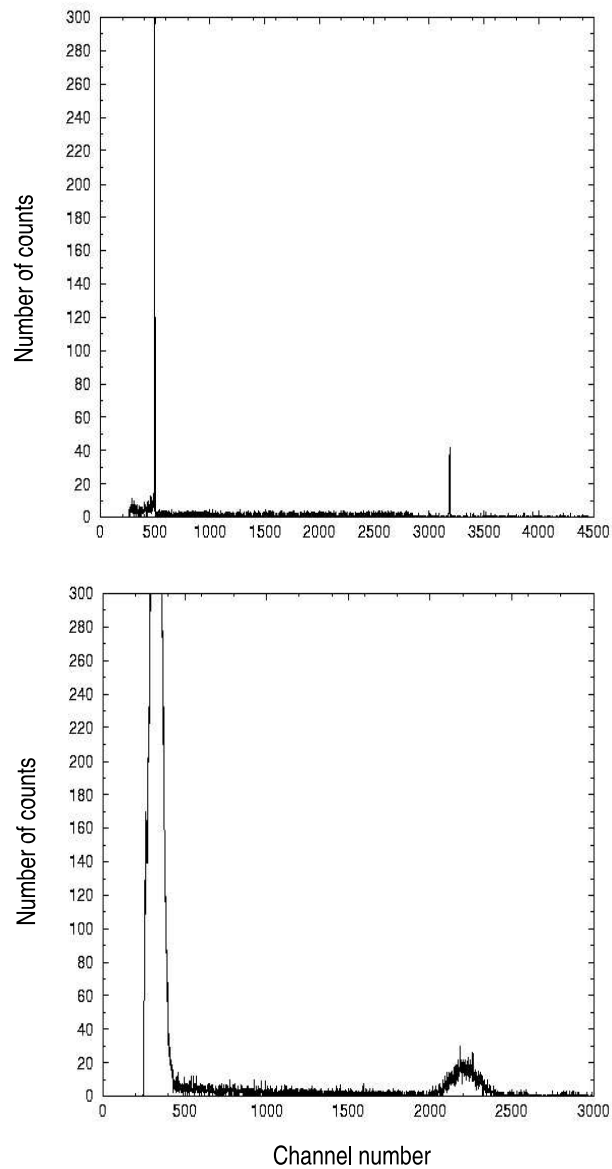
Figure 4.6. Typical spectra for both the Ge detector (above) and the BGO detector experiment (below) are shown. The difference in energy resolution can be appreciated but made no difference in the easy identification of the 1274 keV gamma line from the $^{19}F(\alpha,p_1\gamma)^{22}Ne$ reaction. Both spectra depict single events obtained with passive shielding of the detector crystals.

4.1.6 Yield curve and analysis

The experimental absolute yield Y for gammas was obtained with

$$Y = \frac{N_y(\theta)}{N_\alpha \epsilon_y}, \qquad (4.11)$$

where $N_y(\theta)$ is the number of events registered in the detector, N_α is the number of impinging alphas (obtained by integrating the current at the Faraday cup), and ϵ_y is the efficiency of the detector.

The experimental data points below $E_\alpha = 1.33$ MeV were obtained with a BGO detector at the same position of the Ge detector used in previous runs. The yield curve from the BGO was renormalized to match the germanium detector curve.

The yield curve is shown in figure 4.7. Eight resonances can be identified for the gamma yield from the $^{19}F(\alpha, p_1\gamma)^{22}Ne$ reaction in the range $E_\alpha = 1200 - 1900$ keV. To obtain the resonance strengths from the yield curve we need to consider the effect of the target thickness on the yield value.

Let Y be the thin-target yield (where the energy loss in the target is much smaller than the resonance width) such that

$$Y = \sigma \frac{dE}{\epsilon} \qquad (4.12)$$

where dE is the projectile energy loss in the target, ϵ is the stopping cross section, and σ is the reaction cross section.

To describe the yield for a thick target (where the thin-target condition stated above is not fulfilled) the thin-target yield has to be integrated over the target thickness Δ:

$$Y(E_0) = \int_{E_0-\Delta}^{E_0} \frac{\sigma(E)}{\epsilon(E)} dE. \qquad (4.13)$$
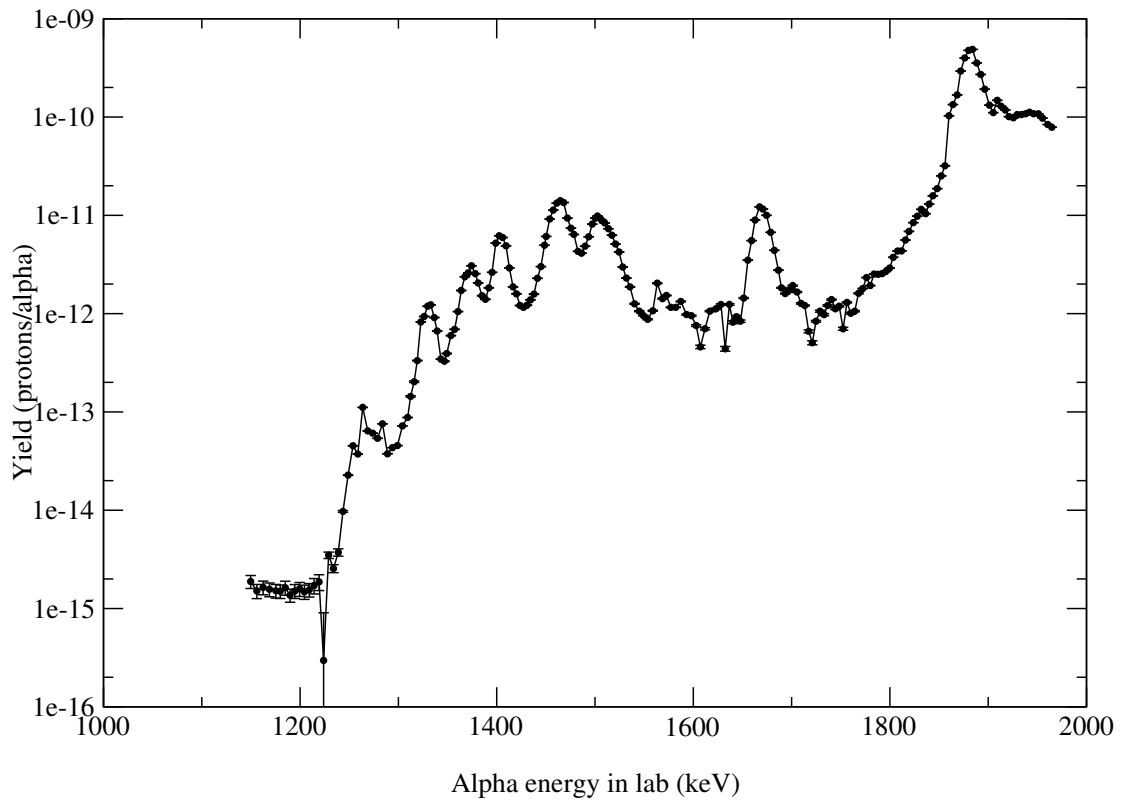
Figure 4.7. Gamma-yield curve from $^{19}F(\alpha, p_1\gamma)^{22}Ne$ between 1.1 MeV and 2.0 MeV of beam energy.

Using the Breit-Wigner formula for $\sigma(E)$ and assuming $\epsilon(E)$ to be constant in the resonance region we get

$$Y(E_0) = \frac{\lambda^2}{2\pi}\omega\gamma\frac{M+m}{M}\frac{1}{\epsilon}\left[\arctan\frac{E_0-E_R}{\Gamma/2} - \arctan\frac{E_0-E_R-\Delta}{\Gamma/2}\right]. \qquad (4.14)$$

Here E_0 is the energy of the projectile, Γ is the total width of the resonance, E_R is the energy of the resonance, $\omega\gamma$ is the strength of the resonance, M is the mass of the target, m is the mass of the projectile, and λ is the Compton wavelength of the projectile.

E_R, Γ, $\omega\gamma$, and Δ were treated as varying parameters and the yield curve was fitted to the yield expression above with a genetic algorithm code (available upon request and based in the techniques described in [78] and [77]). All four parameters were varied at the same time and the strengths and resonance energies are shown in table 4.1. At a 68% confidence interval the error bars for $\omega\gamma$ alone were determined to be of 20%. The routines for calculating the error bars were implemented in the genetic code and are based on the evaluation of the curvature matrix [81].

4.1.7 Discussion of the gamma ray experiment

A discussion on this experiment is given here as no further mention to it is made in this work. The calculation of the reaction rate and the determination of the reduced width amplitudes and energies of the resonances given in the results chapter are independent of this experiment. The simple reason is that as the $^{19}F(\alpha,p_1\gamma)^{22}Ne$ reaction is a three step process (formation of the compound state, decay into the exit channel and decay of the residual) the angular correlation needs to be taken into account as well when analyzing in the context of the R-matrix

theory. The R-matrix code AZURE [7] will include this type of treatment in the near future. Nevertheless, we have decided to include a description of this experiment because it was fundamental in the development of the design of the experiments discussed below. Also, it contains the first evidence of the existence of five resonances in the $^{19}F(\alpha, p)^{22}Ne$ system at the lowest energies ever measured (see tables 4.1 and 4.2). In the spirit of the treatment of experimental data provided by Kuperus [65], we decided to include a Breit-Wigner analysis of the experimental data. It has to be made clear though that this kind of analysis is not appropriate, as discussed in chapter 5.

Regarding the targets used for this experiment, much thinner targets would have improved the energy resolution of the measurement of the cross section. On the other hand very thin targets would have reduced the gamma yield and therefore would have increased the time necessary to accumulate enough counts to get acceptable statistics. The target thickness was a trade off between these two effects.

The genetic algorithm proved to be a powerful tool in the Breit-Wigner analysis for extracting the strengths of the resonances. It may be an alternative to the conventional minimization techniques used by the R-matrix code AZURE. Typical fits are shown in figures 4.8 and 4.9. Of course the interference between resonances is ignored in the analysis.

As a comparison data from Kuperus 1965 [65] are shown in table 4.2.
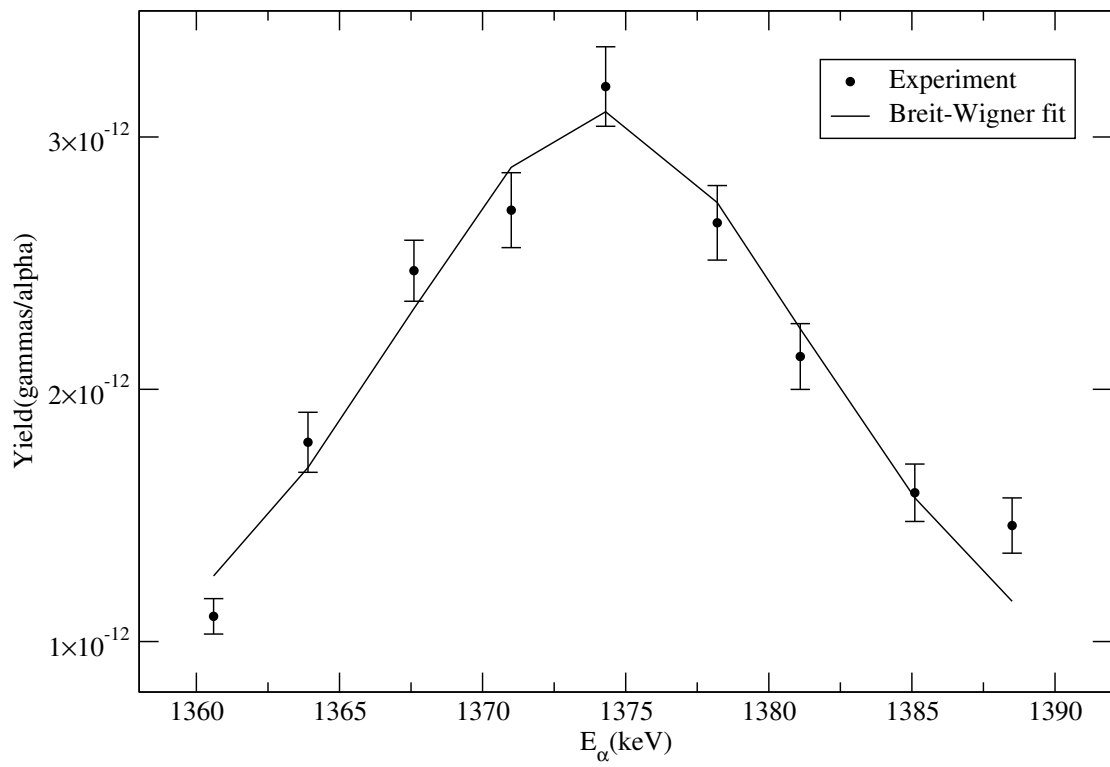
Figure 4.8. Breit-Wigner fit for the resonance at 1372 keV.
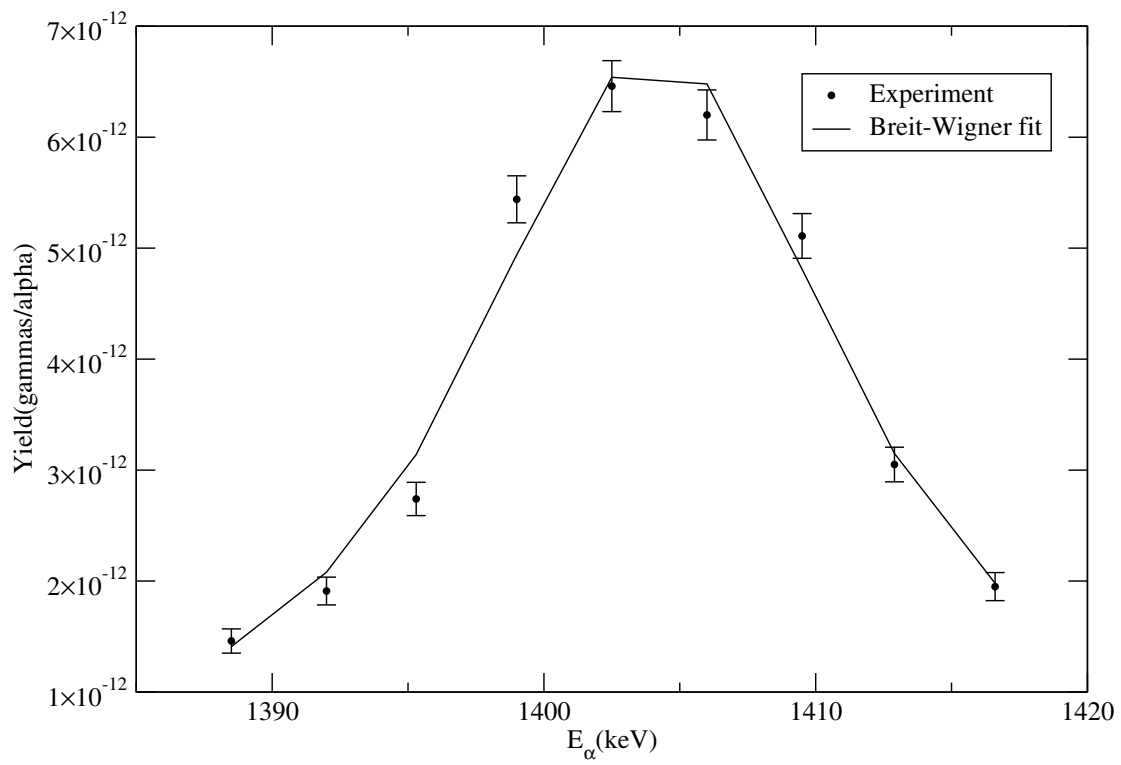
Figure 4.9. Breit-Wigner fit for the resonance at 1401 keV.

TABLE 4.1

RESONANCES FOR $^{19}F(\alpha, p_1\gamma)^{22}Ne$ (THIS WORK).

$E_r(keV)$	$\omega\gamma(eV) \pm 20\%$
1270	0.04
1330	0.21
1372	0.33
1401	0.35
1462	2.1
1503	1.4
1668	2.7
1880	60

TABLE 4.2

RESONANCES FOR $^{19}F(\alpha, p_1)^{22}Ne$ FROM [65].

$E_r(keV)$	$\omega\gamma(eV) \pm 40\%$
1492	1.3
1507	0.26
1574	< 0.7
1879	< 4
1884	27

4.2 The Ortec chamber experiments

A second set of experiments consisted of measuring the excitation function from both exit channels by detecting the protons directly. The setup used for the previous experiment would not work for several reasons. First, protons interact much more strongly with matter than photons; charged particle detectors need to be placed inside the beam line under vacuum to avoid the interactions with air that eventually would stop all protons before they could reach the detection system.

The technique used to measure the reaction yield for this set of experiments depends on the fact that the elastic scattering of alphas on fluorine follows a Rutherford law. The elastics are measured simultaneously with the reaction products (protons) and instead of normalizing to the integrated beam current, the reaction yield is relative to the Rutherford scattering yield.

4.2.1 Preparation of evaporated transmission targets

Targets where beam and reaction products can go through are called transmission targets. They were prepared by evaporating CaF_2 on thin carbon substrates.

The first step in transmission target manufacturing is the preparation of the substrate. Thin carbon foils are delivered commercially mounted on glass slides so they need to be removed from the glass without being torn apart and then mounted on an aluminum frame to allow their handling. This is done by floating the foil in water. To prevent contamination of the foil, distilled (or at least deionized) water was used in the process. The optimum water temperature was found to be

40 ± 2^oC. Lower temperatures made foils very brittle, while higher temperatures caused foils to roll or fold themselves. Before submerging the slides into water, the borders of the carbon foils were removed with a sharp razor to prevent them from being stuck to the glass. Foils are cut into their final size while still mounted on the slides.

Slides are slowly submerged into water at a 45° angle relative to the surface. The carbon foil is then gradually separated from the slide and floats to the surface. An aluminum target frame was used to lift the foil from the surface of the water. Mounted foils were then left to dry overnight.

Thin foils are fragile and break easily with drastic temperature changes, vibration, or even slowly moving air. The situation was improved by flashing foils with an intense light source; photon flux on the foil changed the structure of the surface from a tight, shinny-looking appearance to one relaxed and rough. The foil was able to expand and contract loosely in response to temperature changes induced by the beam or the evaporation process. Energy from mechanical vibration was also efficiently distributed without tearing of the surface. To flash foils, a photographic flash with a guide number of 54 meters at full power was used at a distance of 20 cm. The CaF_2 was then evaporated on the foil substrate with the method described in subsection 4.1.1.

4.2.2 Experimental setup

For these experiments a ^4He beam was produced with the KN van de Graaf accelerator at the University of Notre Dame. The beam was analyzed, collimated and transmitted into the 45° beamline; the Ortec scattering chamber (see figure 4.10) was attached to the end of the beamline. Both beamline and chamber were

kept at a pressure of a few μTorr with cryogenic vacuum pumps. The target was mounted on a ladder attached to a rotating rod at the center of the scattering chamber; the target ladder could hold one target and a collimator at a time. The collimator consisted of an aluminum sheet with a 3.5 mm hole in the center. The beam was focused at the collimator postion by maximizing the current measured at the beam stop. Beam was stopped with a tantalum sheet attached to an aluminum two-inch dependex blank off at the far end of the beamline.

Three EG&G Ortec ULTRA ion-implanted-silicon charged-particle detectors with a B mount and 100 mm^2 of effective area were used to detect both the p_0 and p_1 protons from the $^{19}F(\alpha, p)^{22}Ne$ reaction. They were mounted on aluminum detector holders to the rotating table at 30 and 90° on one side of the chamber and at 130° on the other side. The distance from the center of the target to the detectors was set to 16 cm. Detectors and holders were electrically isolated from each other with plastic insets; thin Ni foils were placed in front of the detectors to stop elastically scattered alphas.

The fourth detector, the target monitor, was mounted directly to the microdot feedthrough on the wall of the chamber at an angle of 160°. It was not shielded with a foil so the elastic scattered alphas were used to monitor the target content at all times. A 1 mm pinhole collimator was placed in front of the detector to reduce the count rate from elastically scattered alphas. A spectrum of elastically scattered alphas is shown in figure 4.11.

For forward angles, where the proton energy is higher, detectors with a depletion depth of 300 μm instead of the 100 μm at backward angles were used. Detectors were connected with microdot cables to vacuum-tight feedthroughs mounted on the wall of the scattering chamber. Outside the chamber, 10 cm long BNC

DETECTORS

ROTATING TABLE

BEAM STOP

TARGET

BEAM

TARGET

LADDER

COLLIMATOR
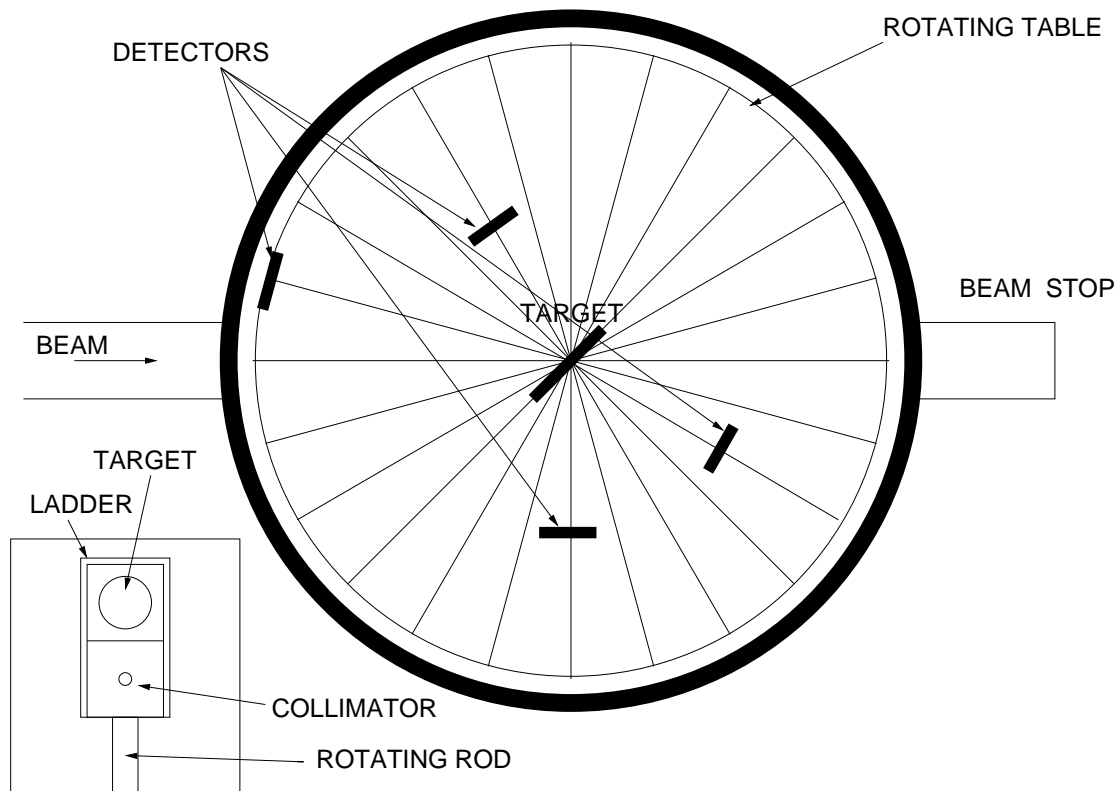
ROTATING ROD

Figure 4.10. Schematic drawing of the Ortec scattering chamber. The chamber's inner diameter is 40 cm. Detectors were mounted on a rotating plate with grooves spaced 15° from each other. The inset shows the target mounted at the upper position of the ladder, and a 3.5 mm diameter collimator used to center and focus the beam. The rod could be rotated and adjusted for height.

64
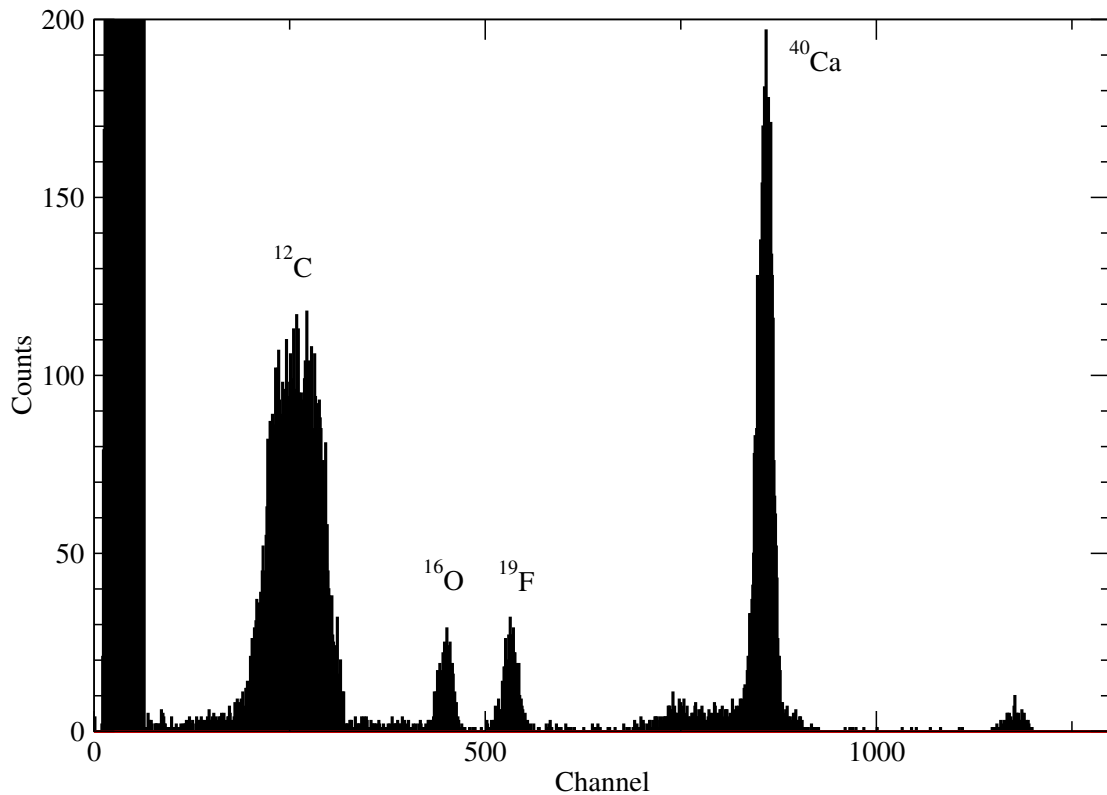
Figure 4.11. Spectrum of alphas elastically scattered from the transmission target. The detector used to take this spectrum was mounted at 160° with respect to the beam direction. The difference in the energy of the detected alphas (and therefore their grouping into peaks) is due to the kinematics from hitting nuclei with different masses. The separation between peaks is enhanced by placing the detector at an angle as back as possible. This technique for monitoring the target contents works only for targets thin enough (thin transmission targets) where peaks do not overlap. The energy of the alpha beam was 1.89 MeV.

cables sent the signal to Ortec 142 preamplifiers. The energy signal from the preamplifiers was then sent to Ortec 671 or 572 amplifiers for further processing. Detectors with a depletion depth of 300 μm were biased through the preamplifiers with TC953 power supplies at 50 volts. Thin detectors (100 μm) were biased with 40 volts.

The analog energy signals were digitized with a 16 channel ADC (Phillips Scientific 752) CAMAC module connected to a Linux computer via a HYTEC 1331 Turbo Personality Card. Data was accumulated and sorted with Daresbury's acquisition software MIDAS. Triggering of electronics was done by sending the fast timing signal from the Ortec 142 preamplifiers to Ortec 579, 454, and 474 fast filter amplifiers. A quad constant fraction discriminator TC 454 converted the timing signal into a logic pulse with a duration of 50 ns at -1.25 volts. A logic fan in/fan out module (Phillips 744) added the logic pulses from all detectors into a single signal as master trigger. A gate generated with a LeCroy 2323 CAMAC module from the master trigger controlled the digitizing process in the ADC.

4.2.3 Energy calibration of charged particle detectors

The calibration of the detectors was done with a $^{241}Am + {}^{148}Gd$ alpha source. ^{241}Am has a $5/2^-$ ground state with a half life of 432.2 years that decays 86% of the time to the $5/2^-$ state at 60 keV of ^{237}Np by emitting a 5486 keV alpha. On the other hand the ground state of ^{148}Gd (0^+) has a half life of 74.6 years and emits a 3183 keV alpha by going the ground state (0^+) of ^{144}Sm. The alpha source was mounted on a rotating rod at the center of the Ortec chamber so all four particle detectors could be irradiated with the chamber under vacuum.

Again, it was assumed that the amplitude of the signal from the detectors

had a linear dependence with respect to the particle energy deposited in the detector from 5486 keV down to the energy of the protons from the reaction of interest (below 1000 keV). However, if the assumption is not fulfilled the result of the experiment would not be affected as long as the estimate of the energy of outcoming protons permits the clear identification of the different groups (p_0 or p_1) involved in the reaction.

The dominant effect in the energy resolution of the detected protons was the straggling in the foil in front of the detectors.

4.2.4 Experimental procedure

A target prepared on a $10\mu g/cm^2$ substrate was mounted with the evaporated material facing the beam and was observed to break shortly after being exposed to a $1\mu A$ alpha beam. Reducing the beam intensity did not help much in keeping the targets in one piece. The carbon substrate thickness was increased to $40\mu g/cm^2$ and targets were then able to hold up to $2\mu A$ of alpha beam. The energy of the alpha beam was set to 1.9 MeV, where the highest proton yield for the experiment was expected. The distance between detectors and target and the beam current were varied so the dead time from detectors and electronics was never over 10%.

The resonance at 1.9 MeV is relatively strong and can be used for normalizing and comparing to Kuperus's 1965 [65] data. From the count rate it was determined that an optimal beam current would be 1.2 μA. A new target was mounted in place and starting at 1980 keV and down to 1630 keV in 5 keV energy steps, proton spectra for each run were taken. It was noticed that after some beam on target the foils shielding the detectors deteriorated: elastically scattered alphas started appearing in the low energy part of spectra.

After a new target was mounted (evaporated in the same batch as the previous target and kept under vacuum while not in use), the base of the chamber was rotated 10° so the detectors at 30° and 90° were moved to 40° and 100°, respectively, and the one at 130° to 120°. This reduced the number of alphas observed at the forward angles significantly.

The 1.67 MeV resonance was rescanned and yield curves were continued to be measured by reducing the energy in 5 keV steps. When the beam energy reached 1224 keV no further energy reduction was done as the count rate in the proton detectors was too small to be able to identify proton groups from the background before the fluorine nuclei have been washed out from the target. The stability of the target was then evaluated by setting the beam energy on top of the 1.9 MeV resonance and measuring the yield of elastically scattered alphas from fluorine at the 160° detector. The result is shown in figure 4.12 and the conclusion was that the stability of the target had to be improved before trying to measure lower energies. The resonance was mapped again with a different target evaporated simultaneosly with the previous target and a thickness of 27 keV was determined. Finally, by placing a mixed alpha source (^{241}Am + ^{148}Gd) with a known activity at the target position the solid angle covered by all detectors was determined.

4.2.5 Yield curve and analysis

Four hundred and eighty three proton spectra were acquired in this experiment and for every energy an elastic scattering alpha particle spectrum was taken. The transmission target feature of the experiment allowed to identify the alpha beam particles scattered from target nuclei with different masses, therefore allowing monitoring of the target content at all times.
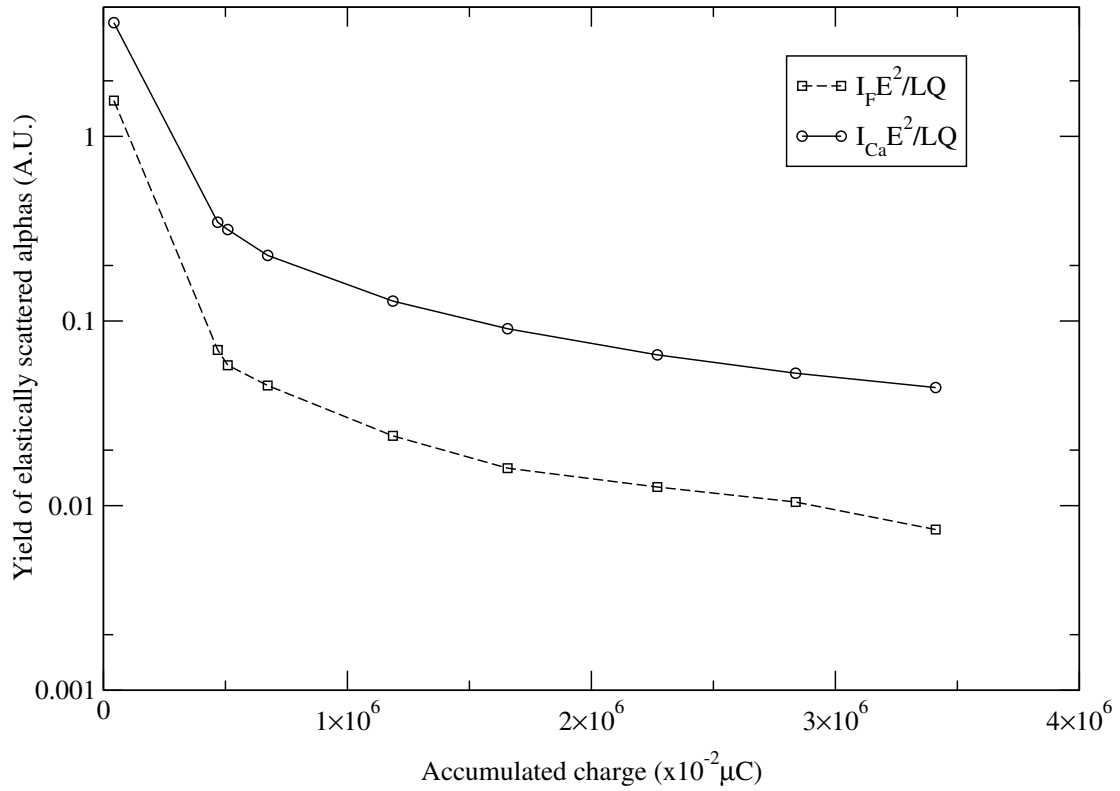
Figure 4.12. The yield of elastically scattered alphas from both calcium and fluorine versus the accumulated charge on target is shown. The Rutherford elastic cross section quadratic energy dependence is removed from the yield by multiplying by E^2. The result is a curve that quantifies the stability of the target as a function of beam exposure. See section 4.2.5 for details.

For any two detectors with the same absolute efficiency the ratio of the number of counts seen in them concurrently is independent of the target stoichiometry and of the beam intensity. The relation can be written as

$$\frac{N_1(E,\theta)}{N_2(E,\theta)} = \left(\frac{d\Omega_1}{d\Omega_2}\right)_{lab/cm} \left(\frac{d\sigma(E,\theta)}{d\Omega}\right)_2^{-1} \left(\frac{d\sigma(E,\theta)}{d\Omega}\right)_1, \qquad (4.15)$$

such that $N_1(E,\theta)$ and $N_2(E,\theta)$ are the number of counts from the interaction of the beam with the target nucleus seen in detectors 1 and 2, respectively, $\left(\frac{d\Omega_1}{d\Omega_2}\right)_{lab/cm}$ is the ratio of solid angles corrected from the center of mass to the laboratory system, and $\frac{d\sigma(E,\theta)}{d\Omega}$ are the differential cross sections measured at detectors 1 and 2, respectively. If one of the detectors is chosen to be the monitor at 160°, and if the elastic scattering differential cross section of alphas on fluorine is known, the differential cross section of the $^{19}F(\alpha,p)^{22}Ne$ reaction can be evaluated. It has been shown by Huang-sheng et al. [53] and by Cseh et al. [17] that below 2.5 MeV the elastic scattering of ^4He on ^{19}F follows a Rutherford cross section, that is

$$\left(\frac{d\sigma(E,\theta)}{d\Omega}\right)_{elastic} = \left(\frac{d\sigma(E,\theta)}{d\Omega}\right)_{Ruth} = \left(\frac{Z_1 Z_2 e^2}{4E}\right)^2 \sin^{-4}\frac{\theta}{2}, \qquad (4.16)$$

such that Z_1 and Z_2 are the atomic numbers of projectile and target, respectively, e is the proton electric charge and $e^2 = 1440$ keV fm, E is the relative energy of target and projectile, in the center of mass, and θ is the center of mass angle at which the elastic scattered particles are observed [94]. Furthermore, from equation 4.13 it is correct to assume that over the target thickness the stopping cross section ϵ is a constant. On the other hand the variation of the elastic differential cross section across the target thickness is very small as it does not show resonant

structure. Therefore the elastic yield can be written as

$$Y_{elas} = \left(\frac{d\sigma(E,\theta)}{d\Omega} \right)_{Ruth} \frac{\Delta}{\epsilon}. \tag{4.17}$$

The stopping cross section as a function of energy was evaluated by sampling from 1.0 to 2.0 MeV in 50 keV steps Ziegler's estimates [106] of the stopping power dE/dx of ^4He on both calcium and fluorine and then fitting a quadratic polynomial to the data points so

$$\left(\frac{dE}{dx} \right)_F = \sum_{i=0}^{2} a_i E^i, \tag{4.18}$$

with a similar relation for the calcium stopping power. A partial stopping cross section can be defined for each of the nuclear species in the target. For example:

$$\epsilon_F = \frac{1}{n} \left(\frac{dE}{dx} \right)_F, \tag{4.19}$$

where

$$n = \nu \rho N_A / A \tag{4.20}$$

with ν the number of atoms per molecule, ρ the density of the target (again assuming the evaporated material has the same density as that one in bulk), N_A the Avogadro number, and A the mass number. The stopping cross section comptutation requires the partial stopping cross sections of the active nucleus (fluorine), the inactive (calcium) and measuring the stoichiometry of the target, so

$$\epsilon = \epsilon_F + \frac{N_{Ca}}{N_F} \epsilon_{Ca}. \tag{4.21}$$

In general the ratio $\frac{N_{Ca}}{N_F}$ measured in an evaporated target does not reflect the

71

stoichiometry of the material before being evaporated. (See [69] for an example on CaF_2, where it is reported that a ratio of calcuim to fluorine of 1:1 was found.) However, it was observed that with the targets used here the stoichiometry of the evaporated material is the same as that of the CaF_2 powder.

The relation between the solid angle in the laboratory and in the center of mass reference system is given by

$$d\Omega_{lab} = \frac{|1 + \gamma \cos \theta_{cm}|}{(1 + 2\gamma \cos \theta_{cm} + \gamma^2)^{3/2}} d\Omega_{cm}, \qquad (4.22)$$

such that γ is obtained by solving the non-analytic relation

$$\tan \theta_{lab} = \frac{\sin \theta_{cm}}{\cos \theta_{cm} + \gamma}. \qquad (4.23)$$

Here θ_{cm} and θ_{lab} are the angles of the scattered particles in the center of mass and the laboratory systems, respectively. (The reader is refered to [63] and [72] for further details.) The corrected ratio of solid angles in the two detectors can then be written as

$$\left(\frac{d\Omega_1}{d\Omega_2}\right)_{lab/cm} = \left(\frac{|1 + \gamma \cos \theta_{cm}|}{(1 + 2\gamma \cos \theta_{cm} + \gamma^2)^{3/2}}\right)_1^{-1} \left(\frac{|1 + \gamma \cos \theta_{cm}|}{(1 + 2\gamma \cos \theta_{cm} + \gamma^2)^{3/2}}\right)_2 \left(\frac{d\Omega_1}{d\Omega_2}\right)_{lab}. \qquad (4.24)$$

By making detector 2 in the previous relations to be the monitor detector and detector 1 the proton detector the center-of-mass differential cross section for the $^{19}F(\alpha, p_0)^{22}Ne$ and $^{19}F(\alpha, p_1)^{22}Ne$ reactions and with equation 4.17, we can write

$$Y_p = \frac{\Delta}{\epsilon} \left(\frac{d\sigma(E, \theta)}{d\Omega}\right)_{prot} = \left(\frac{N_{prot}(E, \theta)}{N_{elas}(E, \theta)}\right) \left(\frac{d\Omega_{prot}}{d\Omega_{elas}}\right)_{lab/cm} \frac{\Delta}{\epsilon} \left(\frac{Z_1 Z_2 e^2}{4E}\right)^2 \sin^{-4} \frac{\theta}{2}, \qquad (4.25)$$

such that Y_p is the target-integrated proton yield.

The experimental dataset obtained with this process is compiled and shown in appendix A(curves 1-6 and 12-17). (See Ugalde et al.[95] for further details.)

4.3 The thick-target chamber experiments

The following set of experiments was designed to measure the proton yield to energies as low as possible. As the reaction probability goes down exponentially as a result of the Coulomb barrier a higher beam current and a larger solid angle are needed. As a result of the increased beam current the stability of targets needed to be improved as well. Fluorine is the most electronegative element in the periodic table; as a result it is akin to bind chemically with matter around it and this makes it hard to keep it in a target exposed to a beam.

4.3.1 Preparation of targets

The first attempt to improve the stability of the targets was to replace the evaporation technique by implanting fluorine on a carbon foil substrate. The SNICS ion source was used to produce a fluorine beam by preparing and mounting a cathode with a mixture of $CaF_2 + Ag$ powders in a 1 to 1 proportion. Calcium fluoride is a crystal with a thermal conductivity low enough (10 W/mK at 273 K) to hinder the production of an intense beam out of the ion source. On the other hand silver has a thermal conductivity of 430 W/mK at 273 K and mixing it into the cathode material is necessary for extracting a useful ion beam.

Down the beamline out of SNICS and towards the FN accelerator (see figure 4.2) an implantation chamber was improvised from a beamline pumping station; the implantation device is shown in figure 4.13. The graphite collimator helps replacing the sputtered nuclei from the foil with the carbon nuclei sputtered from it.
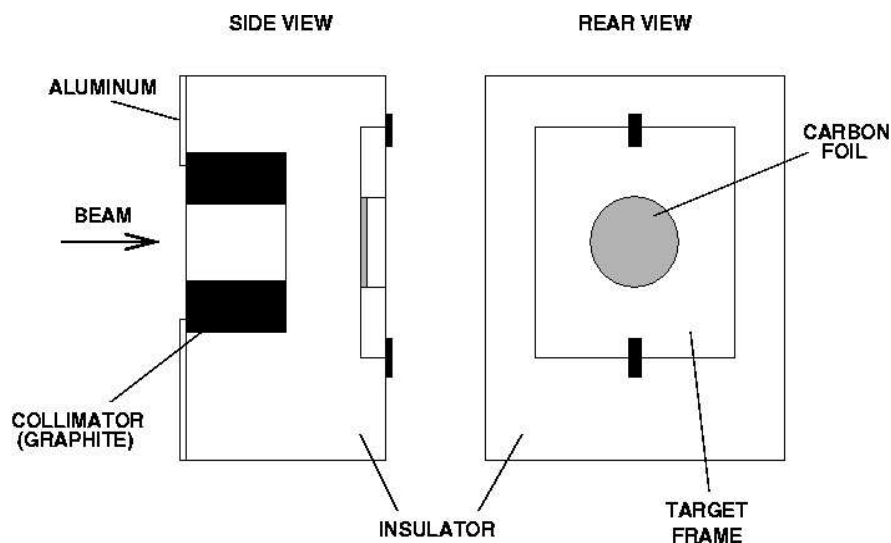
Figure 4.13. The first transmission target implantation device. The insulator was made out of boron nitride and the collimator was graphite. No target cooling capability was implemented here.

Regardless of the beam current, the carbon foil broke soon after the implantation began. No useful targets were produced with this method and the problem was attributed to the lack of a good source of power dissipation via water cooling.

The second attempt to implant fluorine on thin foils was done with a water-cooled target holder-beam collimator device mounted at the implantation chamber. (See fig. 4.14.)

The implanting device consisted of a carbon collimator followed by an insulator and an electron suppression element connected to a power supply set at -400 V. The target cooling element (copper) was isolated from the rest of the device and was in direct contact to an aluminum target ladder thus keeping the thin foils from heating up. Foils with a different thickness (from 10 to 40 $\mu g/cm^2$) were mounted and none were able to withstand fluorine beams above 500 nA. Transmission
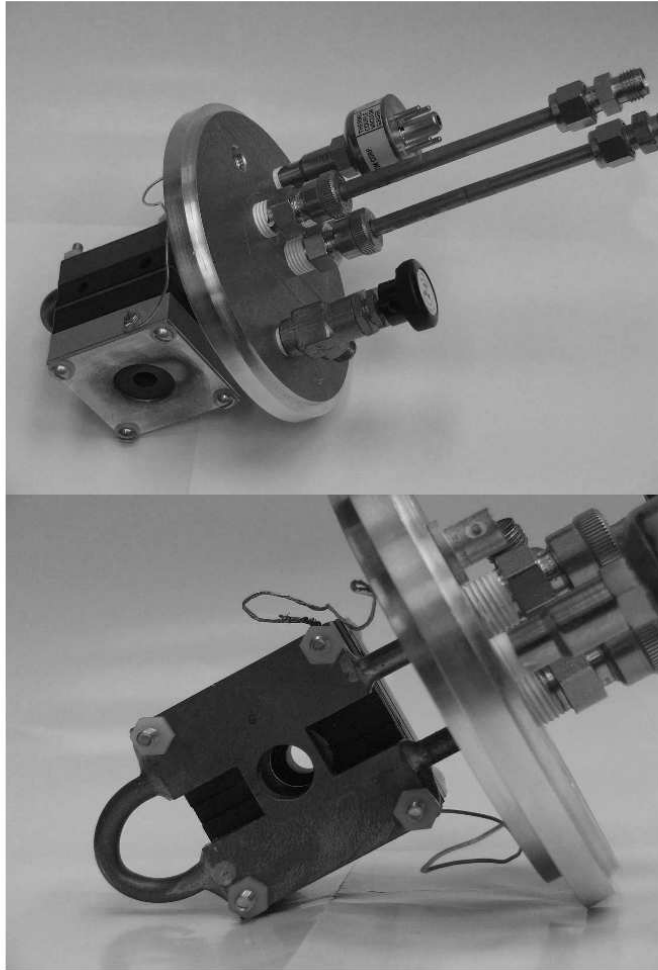
Figure 4.14. Water-cooled implanter. The upper picture shows the graphite collimator side of the device. The two long protruding pipes are the water drain and supply. The copper target holder side is shown in the bottom picture. Two wires are shown and correspond to electron suppression voltage supply and beam current integration at the collimator. The cooling element could hold a target ladder (not shown) where up to four targets could be mounted at a time.

targets were discarded as a viable solution to the target stability problem.

The use of thick targets required the complete redesign of the experimental setup. Two main differences arise here: the first is that particles from the reaction can not emerge on the far side the target.

However, a target tilted with its normal 45° with respect to the beam may be used to obtain scattering angles somewhat greater than 90°. The second difference is that a detector can not be used to monitor the target content using the scattered α-particles because they would have a continuum of energies that eliminates out any information on the target content. Among other things to consider is that the beam is stopped in the target and all the deposited energy needs to be dissipated very efficiently; cooling of the substrate is needed.

Tantalum was used as the first substrate choice for preparing implanted fluorine targets. Three 0.8×0.6 inch targets were implanted with different fluorine doses. The profile of the implanted nuclei was then measured with the 874 keV resonance of the $^{19}F(p, \alpha\gamma)^{16}O$ reaction.

The curves shown in fig. 4.15 were obtained with the use of the experimental set-up described in 4.1.4.

Evident in this first test is the heterogeneous profile of fluorine. Three possible reasons could be attributed to it. First the energy of the fluorine beam was not kept constant while implanting. Second, the surface density of fluorine was not uniform (because of beam density heterogeneity) and during profiling the proton beam sampled different target regions. Last, the targets were so small that during content profiling the target holder was hit at times and the integrated charge had a target holder component not considered in the evaluation of the yield. The implantation device was redesigned to implant larger substrates (1.5×1.5 inches)
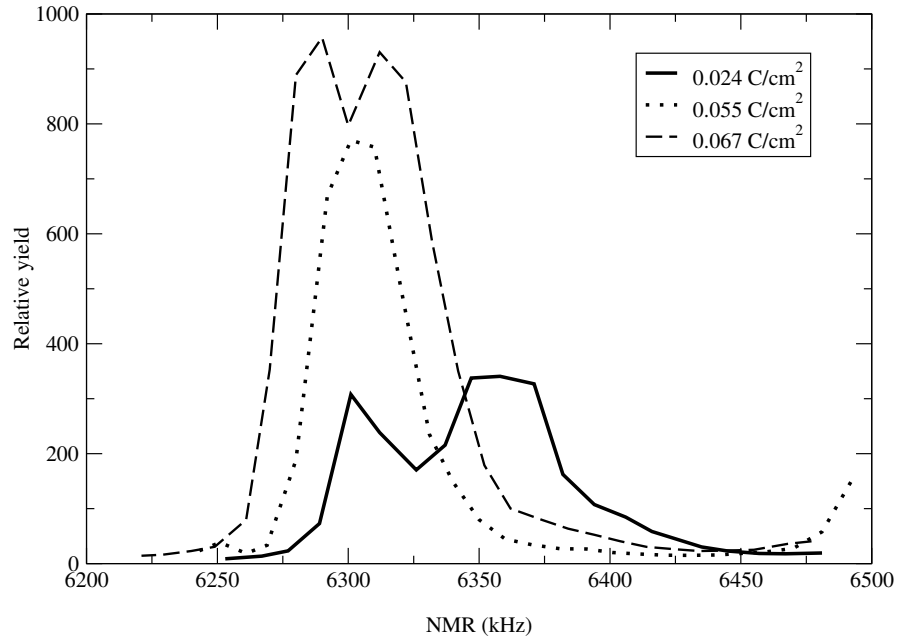
Figure 4.15. Fluorine content profiles for non-wobbled targets. The gamma yield was measured with a NaI detector as a function proton energy (in NMR units) for the $^{19}F(p,\alpha\gamma)^{16}O$ reaction around the 874 keV resonance. A useful target should, among other features, show a smooth profile resembling a single peak. Each curve represents a target with a different amount of implanted fluorine. The surface densities calculated from the integrated charge at the time of implantation identify each target.
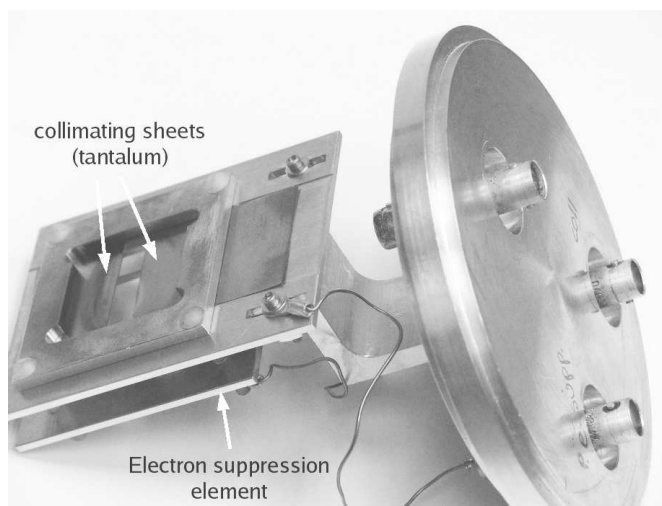
Figure 4.16. Collimator used for implanting fluorine on a solid substrate. The aperture size in the y direction (up-down) can be changed by sliding the tantalum collimating sheets in and out. The electron suppression element can be seen behind the collimator.

and is shown in figure 4.16.

In a second test, a tantalum sheet with a 0.01 inch thickness was held by an aluminum rod at the center of the implantation chamber; it remained isolated from the chamber and the beam current was measured off the rod. The position of the fluorine beam was wobbled this time and its energy carefully kept constant at 70 keV. The SNICS ion source produced beam currents ranging from 30 μA some minutes after the source was lit and down to 800 nA after some hours of operation.

Another desirable target feature when measuring small cross sections is that target nuclei should be as abundant as possible. Of course, there is a physical limit on the amount of implanted nuclei that a substrate would hold and depending on the crystal structure of the material the maximum amount will vary. The
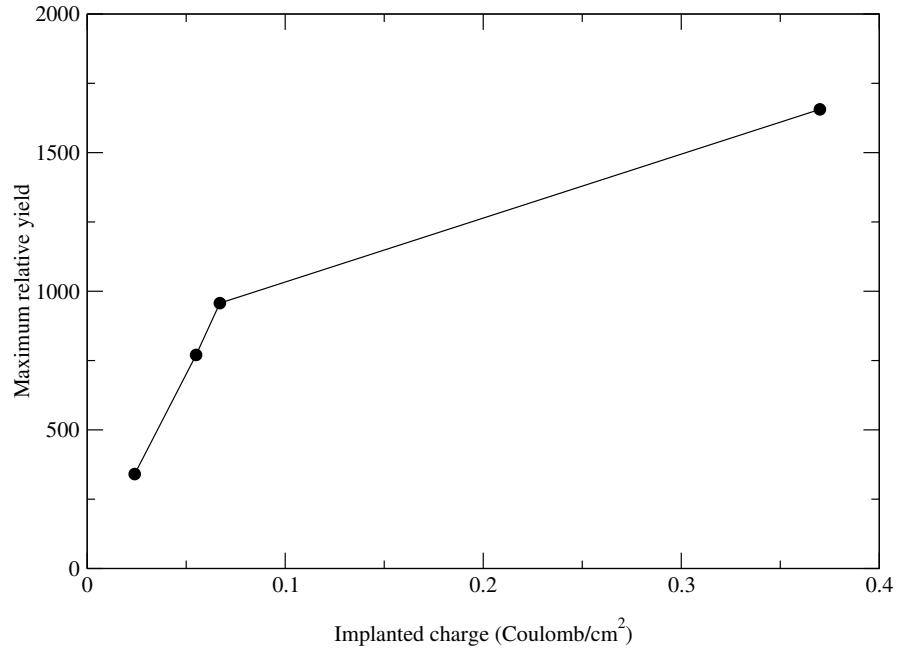
Figure 4.17. The saturation curve for fluorine implanted on tantalum. The maximum yield corresponds to the $^{19}F(p, \alpha\gamma)^{16}O$ resonance at 874 keV, while the implanted charge was obtained by integrating the fluorine beam measured on the substrate at the time of implantation.

saturation curve for fluorine implanted on tantalum is shown in figure 4.17.

The targets obtained with this method were then tested with an α-beam produced with the KN accelerator. The solid target scattering chamber [69] was mounted at the 0° beamline and is shown in figure 4.19. We decided that instead of testing the targets only for thickness with the $^{19}F(p, \alpha\gamma)^{22}Ne$ reaction the stability should be evaluated as well with an α-beam.

Two 450 mm^2 silicon detectors at 90 and 135° were shielded with aluminum foils thick enough to stop elastic scattered alphas and thin enough to let both p_0 and p_1 proton groups go through. The target was water-cooled and electrons were suppressed via a copper tube at -400 V and coaxial to the beam line. The
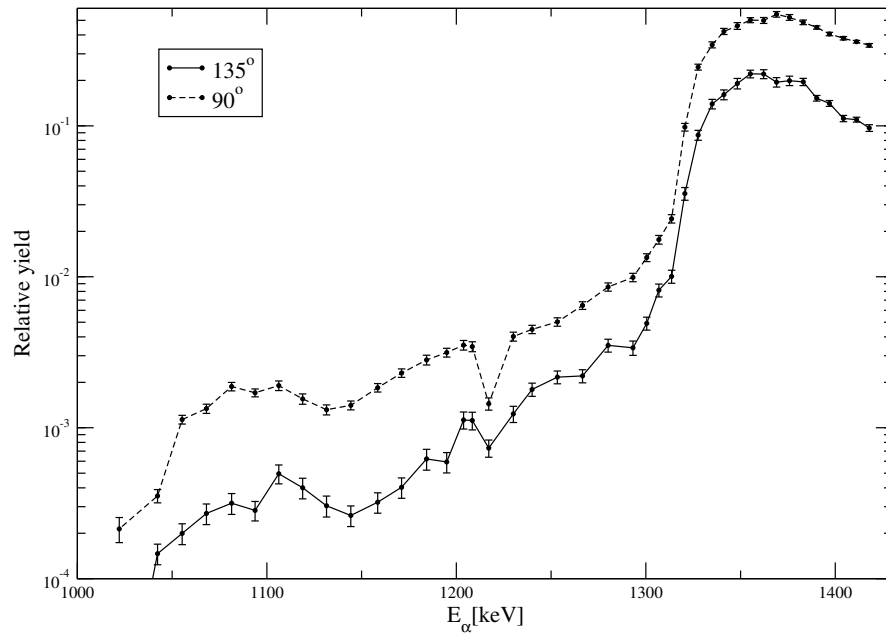
Figure 4.18. Yield curves for the $^{19}F(\alpha, p_0)^{22}Ne$ reaction at 90° and 135° measured with a target implanted with a 70 keV fluorine beam.
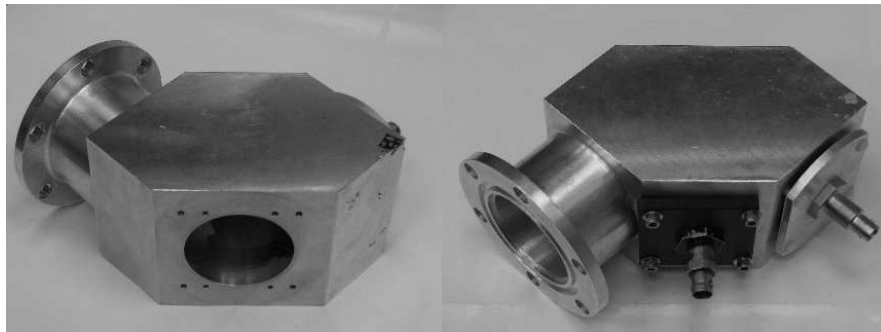
Figure 4.19. The solid target scattering chamber [69] used for testing the fluorine implanted tantalum substrates. On the left the target port tilted 45° with respect to the beam is shown while on the right the detector ports at 90 and 135° degrees, respectively, are shown.
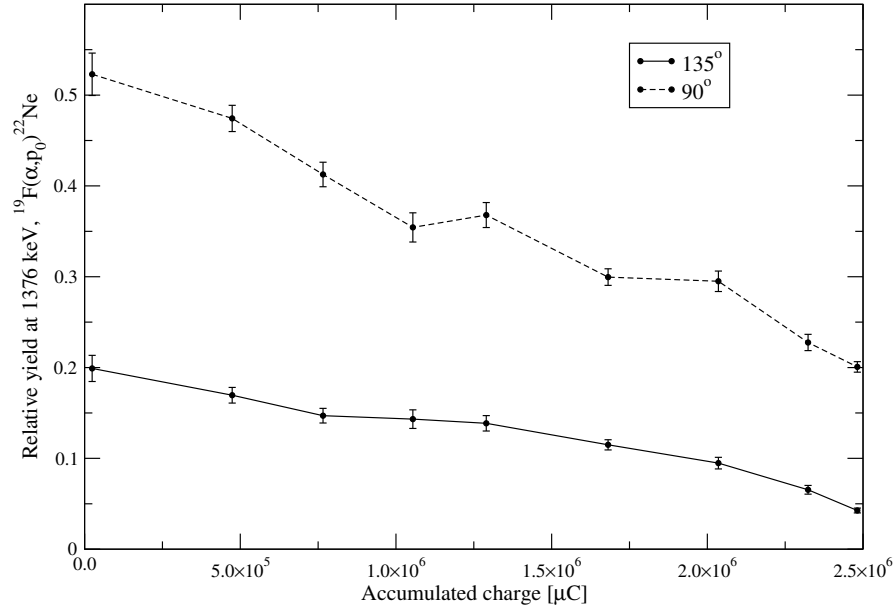
Figure 4.20. The stability of implanted fluorine targets on a tantalum substrate. In order to keep an account of the target content while measuring the curves in figure 4.18 the yield of the resonance at 1.37 MeV in the $^{19}F(\alpha, p)^{22}Ne$ reaction was measured regularly. The plot shows the maximum resonance yield as a function of the accumulated charge on the target. The fluorine content was reduced by 50% after 2 coulombs of alpha beam.

tube was cooled with liquid nitrogen and acted as a cold trap as well. The excitation curve measured for the p_0 channel in both detectors is shown in figure 4.18. By comparing figures 1-6 and 12-17 of the appendix with figure 4.18 the first conclusion one can make is that implanted targets are very thick compared to the evaporated ones used before. On the other hand, as the target content was monitored regularly by scanning the 1.37 MeV resonance, it was determined that the stability of the implanted fluorine (see figure 4.20) could still be improved.

The thickness of the targets can be reduced by implanting with a beam at a lower energy so ions are stopped closer to the substrate surface. Besides, thickness
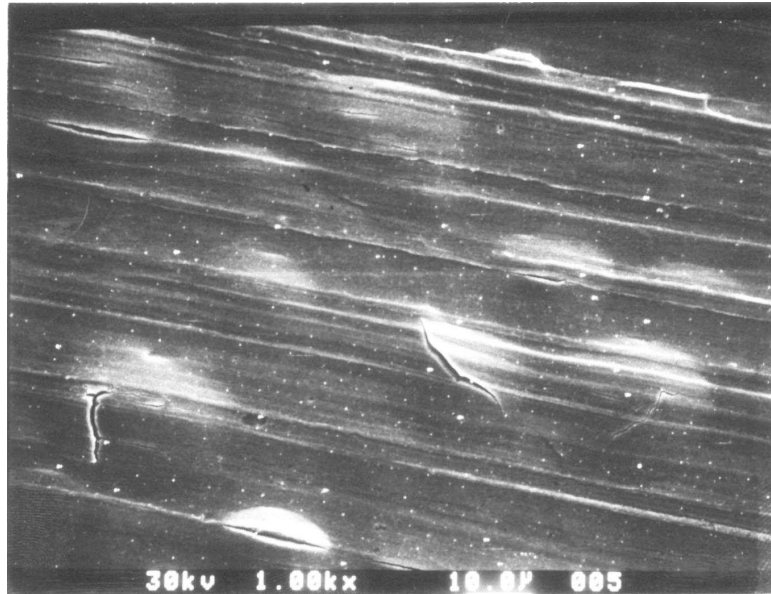
Figure 4.21. 30 kV electron microscope scan of a beam-exposed spot in an implanted fluorine target on a tantalum substrate and exposed to a 2.5 coulomb alpha beam. The surface damage is evident from the cracks and bubbles observed. The scan size is $120 \times 90 \mu m$. (Photo courtesy of Rick Roberts)

can still be reduced further by tilting as much as possible the substrate with respect to the implanting beam

By examining the target under an electron microscope (scan shown in figure 4.21) it was found that the tantalum substrate suffered from severe surface damage from beam exposure. The long lines seen in the scan are due to the milling process of the tantalum sheet; a good part of the damage features are along these lines. It was assumed that if it were possible to produce a substrate without this pattern the situation could have been improved. After not being able to find commercially a smooth tantalum sheet the surface was sanded, baked and attacked with acids.

A relatively smoother surface was obtained but the target stability did not

improve. Trying to find a substrate that would hold fluorine as stable as possible, different materials were implanted and tested after alpha beam bombardment. Some of the materials tried were molybdenum, chromium, nickel, iron, gold, and aluminum. The best stability was achieved with an iron substrate. In figure 4.22 a comparison between targets with the fluorine implanted on tantalum and iron before and after being exposed to alpha beam is shown. The fluorine content in the tantalum substrate was seen to decrease, while in iron, the fluorine yield was even seen to increase by about 10%. All iron targets showed the same behaviour, peaking at around 1 coulomb of accumulated charge and regardless of the beam type used to profile the fluorine content (an explanation of this effect is discussed in [99]). A complete stability curve for the iron substrate is shown in figure 4.23 and can be compared to the tantalum case in figure 4.20.

Thirteen targets were implanted in iron with a wobbled fluorine beam at 36 keV and with the substrate tilted 75° with respect to the beam direction. The amount of fluorine obtained was about one order of magnitude smaller than that of an new evaporated target (see figure 4.24).

4.3.2 Experimental setup

The scattering chamber for the last set of experiments was redesigned from the one shown in figure 4.19. The new chamber is shown in figure 4.25 and among the new features it allowed mounting of the target at two different angles with respect to the beam: at 45 ^{o} and perpendicular. The first option was used to measure scattering angles below 90°, while for the second the effective target thickness was minimized in the beam direction. Another new feature was the flexibility for mounting the detectors at different angles on a rotating plate. However, the
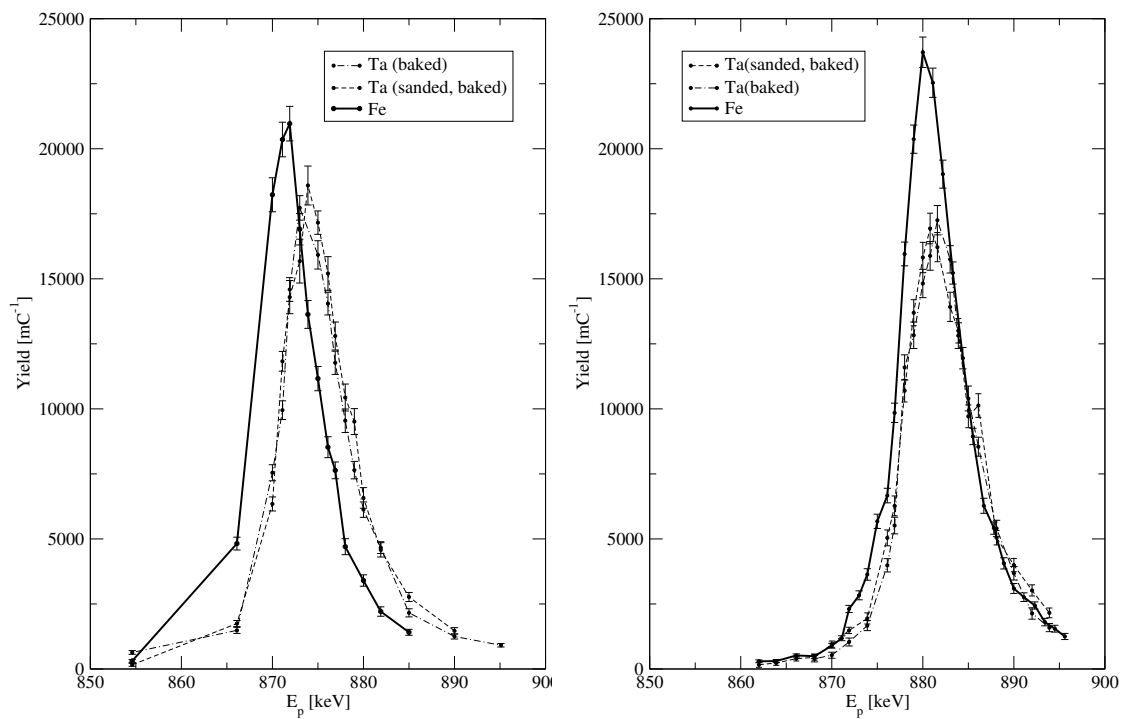
Figure 4.22. Fluorine content of targets implanted on tantalum and iron before (left) and after (right) being exposed to 0.8 coulombs of alpha beam. The curves correspond to the gamma yield from the 874 keV resonance in the $^{19}F(p, \alpha\gamma)^{16}O$ reaction.
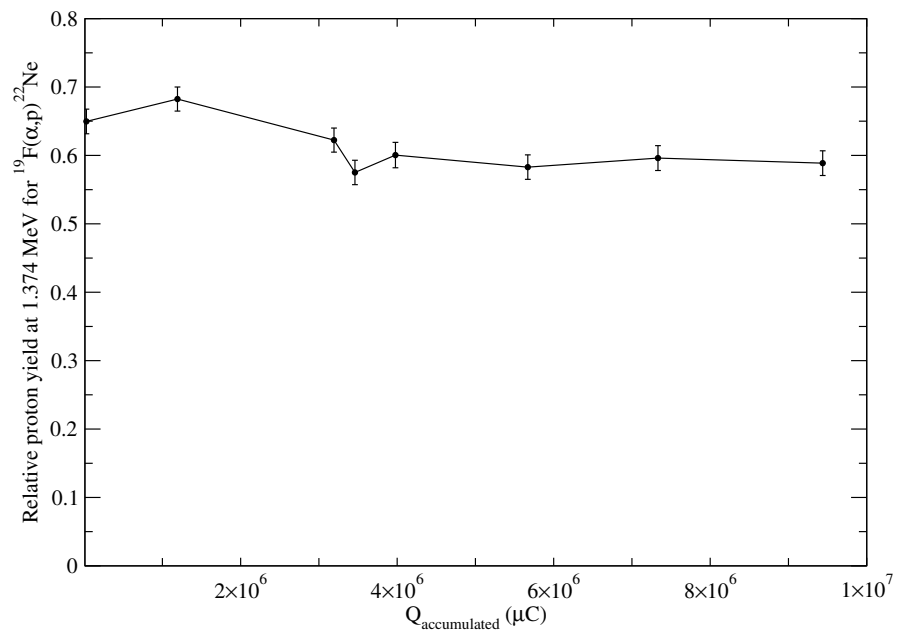
Figure 4.23. The stability curve for the amount of fluorine in an iron substrate. The data points correspond to the maximum proton yield obtained for the 1.37 MeV resonance in the $^{19}F(\alpha, p)^{22}Ne$ reaction using a single target for various accumulated charges. The slight increase in the yield at 1 coulomb was observed for all the fluorine targets implanted on an iron substrate. The solid line is a guide for the eye.
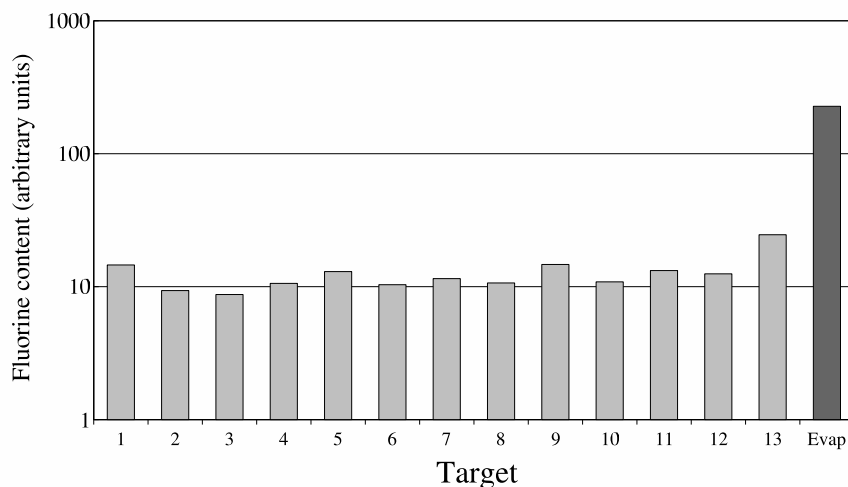
Figure 4.24. Relative amount of fluorine for the implanted targets (light grey) and a new evaporated target (dark grey).

number of detectors was limited to two at a time as the solid angle had to be maximized to be able to measure the small cross sections. Both detectors and rotating plate were electrically isolated from the rest of the chamber.

Electron suppression was implemented with an aluminum plate at -400 volts and 5 mm from and in front of the target. Carbon buildup on the target was minimized with a copper plate kept at liquid nitrogen boiling temperature (77.4 K). The target itself was water cooled from the back and electrically isolated fom the scattering chamber. Beam current was directly measured from the target holder.

The detectors were mounted to the rotating plate with aluminum holders equipped with collimators and foils (aluminum as well) shielding them from elastic scattered alphas. Several sets of foils were tested with beam on target until a pinhole-free pair was found. The detectors used had an effective detection area of
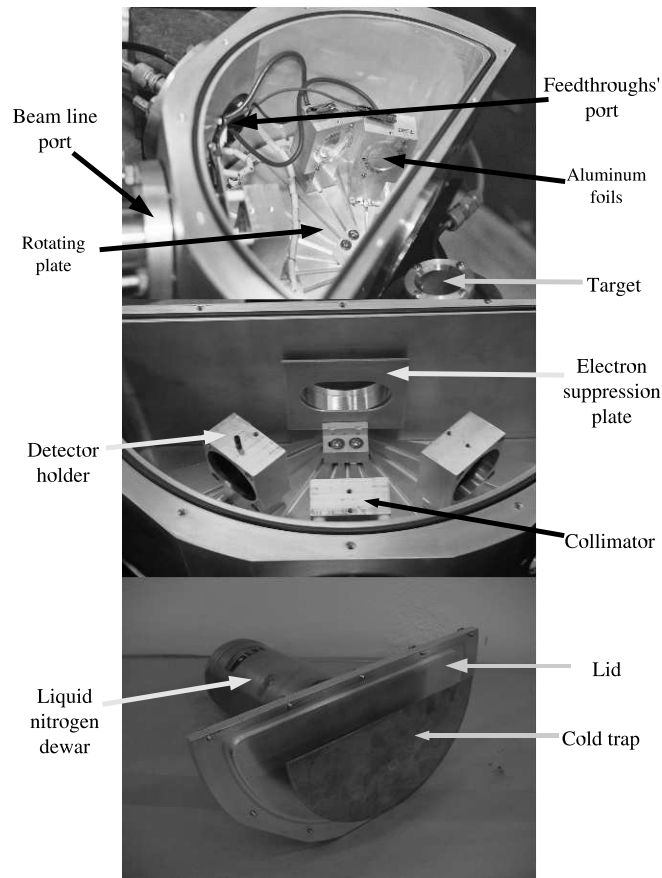
Figure 4.25. Solid target scattering chamber. The picture at the top shows the chamber mounted in its 45° target position. Both feedthroughs' and beamline ports are 2 inch dependex standard ports. The perpendicular-target position is achieved by connecting the beamline to the other port. The middle picture shows the typical detector arrangement for the perpendicular target position; both detectors are mounted at 135°. The bottom picture shows the chamber lid and the cold trap system.

450 mm^2 an were biased with Tennelec TC953A power supplies at 81 and 85 volts. The signal from the detectors was sent to microdot to BNC feedthroughs in one of the ports of the scattering chamber (see figure 4.25). Ortec 142 preamplifiers took the signal from the feedthroughs outside the chamber and sent it to Ortec 572 amplifiers. Spectra were acquired with two Ortec Maestro cards and software running in a PC computer.

The charge on target was measured by integrating the beam current with an Ortec 439 digitizer and after run 165 (because of failure) with a BIC 1000a current integrator.

4.3.3   Yield curves and analysis

With the chamber at the perpendicular target position and both detectors at 135°, 540 spectra were acquired for energies between 1380 keV and 792 keV. Typical spectra are shown in figure 4.26; the last spectrum taken (792 keV) did not show identifiable proton groups.

The solid angle covered by each of the detectors is a parameter needed to evaluate the yields. A mixed alpha source ($^{241}Am+^{148}Gd$) with a nominal activity of 69.11 nCi and 69.31 nCi, respectively, and as of February 1, 2004 was mounted at the target position. One spectrum for each detector was taken.

The activity of a radioactive source as a function of time $A(t)$ is given by the relation

$$A(t) = A_o \exp(-\lambda t), \tag{4.26}$$

such that A_o is the activity at a given time t_o and t is the time elapsed since t_o. λ is the decay constant and is defined as the inverse of the time elapsed at which the activity of the source has been reduced by a factor of $1/e$. The activity $A(t)$ at
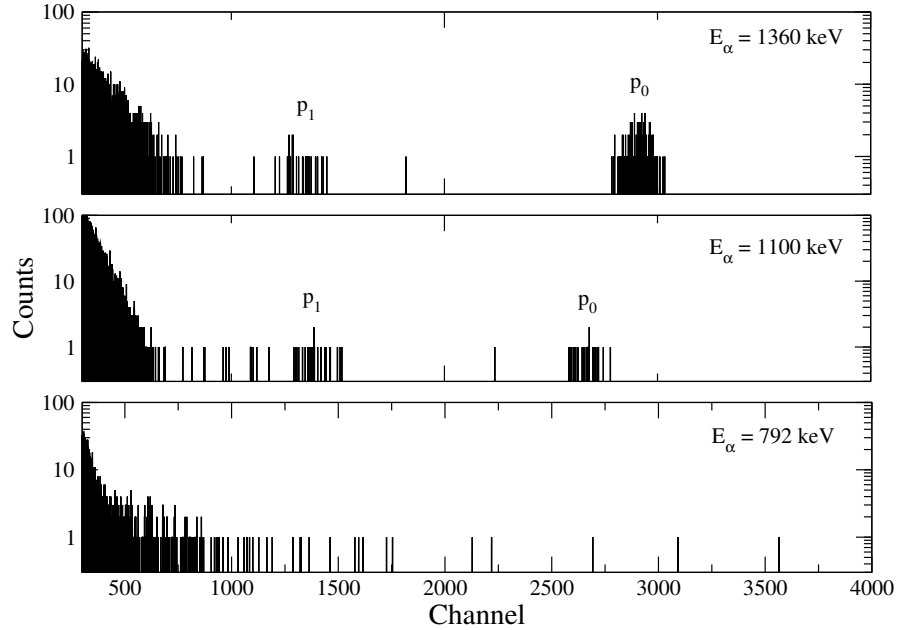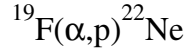
Figure 4.26. Proton spectra for $^{19}F(\alpha, p)^{22}Ne$ at 135° for three beam energies (label at the right upper corner of each box). The upper spectrum shows both proton groups at the reference resonance. Both peaks appear clean of background and are easy to identify. The spectrum at 1100 keV shows two groups of protons, still well isolated from the almost inexistent background. Finally, a spectrum at 792 keV, where no proton groups were positively identified is shown. The integrated charges are (in μC) 1981, 180647, and 519252, respectively.

the time of the solid angle determination was evaluated and assuming the alphas decay isotropically, the equation

$$\frac{A_{tot}}{4\pi} = \frac{A_{measured}}{\Omega}, \tag{4.27}$$

is fulfilled as well. Here A_{tot} is the activity of the source (equivalent to $A(t)$ from above), $A_{measured}$ is the activity measured at the detector, and Ω is its solid angle. It was determined the solid angles to be 0.1302 and 0.1329 steradians, respectively for each detector.

Spectra were converted from the Ortec Maestro native format to a single text column file with the total number of counts for each of 8192 channels. The files were passed on to the computer code JTEK [40] and analyzed by selecting lower and upper channels around each one of the two peaks. JTEK counts the number of events in each region; background around peaks was treated by fitting a straight line to it and substracting the area under the fitted line inside the window from the peak counts. Nevertheless, most of the time spectra were background free already.

Let $N_y(\theta)$ be the number of proton events registered in the detector in time t and Y the experimental reaction yield. Their relation can be written as

$$N_y(\theta) = N_p Y \epsilon_y d\Omega_y, \tag{4.28}$$

where N_p is the number of impinging projectiles in time t, ϵ_y is the absolute detection efficiency (assumed to be 1 for charged particles and silicon detectors at very low count rates), and $d\Omega_y$ is the solid angle subtended by the detector.

The registered number of counts in the detector depends both on the cross

section and on the target content of active nuclei. As charge is accumulated in the target the amount of fluorine is decreased. Therefore, a correction for target stability is required. During the experiment we monitored the target content by scanning regularly a reference resonance. (See figure 4.23.) A curve was fitted and then used to normalize all yield points. For each detector, a least squares fit for the maximum yield in the 1.37 MeV resonance was performed; it was assumed that all targets have the same thickness as all were implanted with the same fluorine-beam energy. The relation is

$$Y_{fitted} = a + bQ_{acc}, \tag{4.29}$$

such that Q_{acc} is the accumulated charge on the target and a and b are constatnts. Let us define the stability factor $f(Q_{acc})$ by

$$Y_{corrected} = f(Q_{acc})Y_{uncorrected}, \tag{4.30}$$

where $Y_{corrected}$ and $Y_{uncorrected}$ are the corrected and uncorrected yields, respectively. Then we finally write

$$f(Q_{acc}) = \frac{a}{a + bQ_{acc}}. \tag{4.31}$$

The chamber was reoriented to the 45° target position. The detectors were mounted at 150° and 120° and 178 spectra were taken. The reference resonance was scanned both before and after the excitation curve measurement. Finally, the detectors were mounted at 75° and 105° and 69 spectra were measured.

4.4 The excitation curves

Data from sections 4.2 and 4.3 were taken as the set of experimental informa-
tion to be analyzed in this work. The set consists of 20 excitation functions, with
eleven corresponding to $^{19}F(\alpha, p_0)^{22}Ne$ and nine to $^{19}F(\alpha, p_1)^{22}Ne$. Ten angles
were measured in different energy regions. All add up to 1505 data points.

Excitation curves from section 4.3 were matched to those of section 4.2 at 120°,
angle measured in both sets of experiments. The resulting excitation curves are
plotted in appendix A, and their interpretation in terms of nuclear parameters (en-
ergies and reduced width amplitudes of resonances) requires a target integration
and an analysis in terms of a multilevel formalism of low energy nuclear reactions.

CHAPTER 5

LOW ENERGY NUCLEAR REACTIONS

In this chapter we describe the theory behind two body nuclear reaction phenomena at energies where strong resonant structures are observed. The model and assumptions for the reaction mechanism are presented and some of its limitations are discussed and the mathematical machinery used for interpreting the experimental dataset in terms of nuclear physics parameters is outlined.

5.1   Model of a nuclear reaction

Understanding of the two-body nuclear reaction process has been pioneered by studying neutron captures. As the neutron does not carry an electric charge the Coulomb potential is not present and the reactions are not hampered by the strong repulsive barrier. By analyzing the lifetimes of resonant structures from the gamma spectra produced by neutron exposure of some nuclei, Bohr concluded in 1936 [9] that these nuclear captures can be thought as two step processes. The first step consists of the formation of an intermediate "compound nucleus" with a number of nucleons equal to that forming the target+projectile system. During this step the collision energy is distributed among all nucleons in the compound. The second step corresponds to the decay of the compound into one of the energetically, parity, and angular momentum-permitted exit channels.

In principle both steps are independent of each other, meaning that beside the conservation rules the compound nucleus has no "memory" of the manner in which it was formed. However, one condition would be favorable to form the compound nucleus: the energy of the collision has to correspond to one of the excited states in the compound. When this is the case the reaction mechanism is called "resonant". Other kinds of reactions (direct reactions) do not involve the formation of a compound and go through a one-step fast process where single nucleons are picked up or stripped from the projectile as it passes through or close to the target.

Other resonant mechanisms are observed in nature, such as in atomic and molecular absorption phenomena. However, although described mathematically in an equivalent way, the nuclear resonant case is fundamentally different in the sense that the energy is shared among all nucleons in the compound system.

The theory outlined here is better known as the "R-matrix" theory. We base our discussion on the review by Lane and Thomas in 1958 [66]. It is not specific to the compound nucleus model but it was conceived from it.

Let us define a 3A dimensional space such that A is the number of nucleons of the target + projectile system. Each of three dimensions per nucleon corresponds to a spatial coordinate. Let a be the distance between target and projectile at time t. Now we divide the 3A space into two regions separated by a 3A-dimensional hypersphere of radius a_c; the internal region is such that $a < a_c$, while the external corresponds to $a > a_c$. The shell $a = a_c$ is called the boundary. The main assumption of the model is that nuclear reactions can take place only in the internal region. Of course this does not mean that when the target + projectile system is found in the internal region a reaction will take place; this feature of the

theory allows us to describe the formation of a compound followed by decay into the elastic channel (i.e. that where the incoming particles have the same identity as the outgoing pair).

Another important feature of the R-matrix theory is that it is time symmetric: only the strong and electromagnetic interactions are considered. This means that whatever is meant to be an outgoing channel is also an incoming channel. In this way we say that the external region contains all the possible channels; no label to whether a channel is incoming or outgoing is introduced. However, in the practice a nuclear physicist tends to think in terms of "formation" and "decay" channels. This is acceptable but irrelevant for the theory.

We now define two sets of eigenfunctions in which we will expand the wave-functions for describing the system: one for the internal region and another for the external. First, we require the internal set to satisfy the Schrödinger equation

$$HX_{\lambda JM} = E_{\lambda J}X_{\lambda JM}, \tag{5.1}$$

such that J and M are the angular momentum and its projection of some internal states with energy $E_{\lambda J}$ and λ identifies the eigenstate. The $E_{\lambda J}$ are eigenstates not necessarily representing the excited states of the compound; from now on we will call them "R-matrix energies" and correspond to the first set of input parameters for the theory. On the other hand, the wave function in the internal region ψ_{JM}^{INT} is written as a linear combination of the $X_{\lambda JM}$'s, i.e.

$$\psi_{JM}^{INT} = \sum_{\lambda} A_{\lambda J}X_{\lambda JM}, \tag{5.2}$$

such that the $A_{\lambda J}$ are coefficients that in general are energy dependent.

On the other hand, the wave function for the external region Ψ^{EXT} is a linear combination of the product of the two wave functions describing the structure of the colliding nuclei (one for the target and other for the projectile), the wave function for the motion of the center of mass of the system (irrelevant for the theory) and that of the relative motion between both nuclei. Therefore we write

$$\Psi^{EXT} = \sum u_{\alpha sl} \phi_\alpha, \tag{5.3}$$

where we have dropped the center of mass motion part, combined the two structure wave functions into a single ϕ_α and written the relative motion wave function as $u_{\alpha sl}$. Here α is the channel, s is the spin, and l is the orbital angular momentum. The external radial Schrödinger equation is then written as

$$\left[\frac{d^2}{dr^2} - \frac{l(l+1)}{r^2} - \frac{2\mu}{\hbar^2}(V_{\alpha sl} - E_\alpha) \right] u_{\alpha sl} = 0, \tag{5.4}$$

with μ the reduced mass of the system, and $V_{\alpha sl}$ the potential, which can be safely assumed to be Coulomb alone, so we write

$$u_{\alpha sl}'' - [l(l+1)\rho_\alpha^{-2} + 2\eta_\alpha/\rho_\alpha - 1]u_{\alpha sl} = 0 \tag{5.5}$$

after making $V_{\alpha sl} = Z_1 Z_2 e^2/r$, $\rho_\alpha = kr$, and η the Sommerfeld parameter defined in equation 3.14. The family of solutions to the equation are a linear combination of incoming (I_c) and outgoing radial waves (O_c). Both I_c and O_c are in general complex functions that can be conveniently written in terms of regular F_c and

irregular G_c real functions as well. Their relation is as follows:

$$I_c = (G_c - iF_c)\exp(i\omega_c) \tag{5.6}$$

$$O_c = (G_c + iF_c)\exp(-i\omega_c), \tag{5.7}$$

with

$$\omega_c = \sum_{n=1}^{l}\tan(\eta/n). \tag{5.8}$$

Rewriting the total wave function in the external region Ψ^{EXT} in terms of the radial waves gives:

$$\Psi^{EXT} = \sum_c (A_c I_c + B_c O_c)\phi_\alpha. \tag{5.9}$$

Now by definition the collision matrix $U_{c'c}$ stablishes the relation between the coefficients of the radial wave functions and is given by

$$B_c = \sum_{c'} U_{c'c} A_{c'}, \tag{5.10}$$

so we write

$$\Psi = \sum_{c'c}(\delta_{c'c}I_c - U_{c'c}O_{c'})B_c \tag{5.11}$$

where $\delta_{c'c}$ is Kronecker's symbol and, as the sum goes through all channels, Ψ is the total wave function.

Let us write now the integrated cross section $\sigma_{\alpha\alpha'}$ i.e. the reaction cross section for the $\alpha \to \alpha'$ process in terms of the collision matrix $U_{c'c}$:

$$\sigma_{\alpha\alpha'} = \frac{\pi}{k_\alpha^2}\sum_{Jsls'l'} g_J |T_{\alpha's'l'\alpha sl}^J|^2, \tag{5.12}$$

97

with the spin factor g_J given by

$$g_J = \frac{2J + 1}{(2I_1 + 1)(2I_2 + 1)} \tag{5.13}$$

and I_1, I_2, and J the spins of the two colliding particles and of the compound, respectively. Here $T^J_{\alpha's'l'\alpha sl}$ is the "T collision" matrix defined by

$$T^J_{\alpha's'l'\alpha sl} = \exp(2i\omega_{\alpha'l'})\delta_{\alpha sl\alpha's'l'} - U^J_{\alpha sl\alpha's'l'}, \tag{5.14}$$

where the collision matrix U has been reindexed for the spin s and orbital angular momentum l of the approaching particles.

It is equation 5.12 the one representing the cross section required in equation 3.11 for calculating the reaction rate. The evaluation of the collision function has involved only external quantities; we have not made use of the internal features of the model. Basically what we need to do is match internal and external wave functions and relate the collision matrix to the internal parameters of the theory.

5.2 The R-matrix parameters and the boundary condition

Having defined the wave functions in both the internal and external regions of the configuration space we now require logarithmic derivative continuity at the boundary $a = a_c$, i.e. we match the wave functions and their derivatives at a_c. Let us define the value V_c and the derivative D_c as

$$V_c = \left(\frac{\hbar^2}{2\mu a_c}\right)^{1/2} u_c(a_c) \tag{5.15}$$

$$D_c = \left(\frac{a_c \hbar^2}{2\mu}\right)^{1/2} u'_c(a_c), \tag{5.16}$$

where the variuos quantities have been defined in chapter 5. By rewriting them as surface integrals but using the internal eigenfunctions in place of u_c one obtains

$$\gamma_{\lambda c} = V_c = \left(\frac{\hbar^2}{2\mu a_c}\right)^{1/2} \int \phi_c^* X_{\lambda JM} dS \tag{5.17}$$

$$\delta_{\lambda c} = D_c = \gamma_{\lambda c} + \left(\frac{a_c \hbar^2}{2\mu}\right)^{1/2} \int \phi_c^* \nabla X_{\lambda JM} dS, \tag{5.18}$$

such that ϕ_c are surface functions forming a complete set and dS is the surface element.

Beside being a complete orthonormal set (in the sense of a Hilbert space), the internal eigenfunctions $X_{\lambda JM}$ are imposed the boundary conditions

$$b_c = \frac{D_{\lambda c}}{V_{\lambda c}}. \tag{5.19}$$

In general, any wave function Ψ can be expanded in terms of the set, i.e.

$$\Psi = \sum_\lambda A_\lambda X_\lambda, \tag{5.20}$$

such that

$$A_\lambda = \int X_\lambda^* \Psi d\tau \tag{5.21}$$

and τ is the internal region of space. In short, we are describing the external region in terms of a complete set defined in the internal region, provided the conditions at the boundary are fulfilled. This is the heart of the R-matrix theory of nuclear reactions.

Now, we will evaluate the last integral above; this requires the use of Green's theorem and a mathematical trick. Let us write the Schrödinger for two energies

E_1 and E_2:

$$H\Psi_1 = E_1\Psi_1 \tag{5.22}$$

$$H\Psi_2 = E_2\Psi_2. \tag{5.23}$$

By multiplying the first equation by Ψ_2^*, the second by Ψ_1, substracting one from the other and integrating over the internal region τ we get:

$$(E_2 - E_1)\int_\tau \Psi_2^*\Psi_1 d\tau = \int_\tau [(H\Psi_2)^*\Psi_1 - \Psi_2^*H\Psi_1]d\tau. \tag{5.24}$$

By applying the Green theorem then

$$(E_2 - E_1)\int_\tau \Psi_2^*\Psi_1 d\tau = \left(\frac{\hbar^2}{2\mu a_c}\right)\int_S (\Psi_2^*\nabla\Psi_1 - \Psi_1\nabla\Psi_2^*)dS. \tag{5.25}$$

By making $E_1 = E$ and $E_2 = E_\lambda$, and by using equations 5.17 and 5.18 we rewrite equation 5.21 as

$$(E_\lambda - E)A_\lambda = \sum(D_c - b_cV_c)V_c, \tag{5.26}$$

so equation 5.20 becomes

$$\Psi = \sum_{c\lambda}\left[\frac{X_\lambda V_c}{E_\lambda - E}\right](D_c - b_cV_c). \tag{5.27}$$

We now multiply by the surface function ϕ_c^* and integrate over dS for the whole hypersphere so, with equations 5.17 and 5.18 again one gets

$$V_{c'} = \sum_c\left[\left[\sum_\lambda \frac{\gamma_{\lambda c'}\gamma_{\lambda c}}{(E_\lambda - E)}\right](D_c - b_cV_c)\right]. \tag{5.28}$$

By definition, the R-matrix $R_{c'c}$ is given by

$$R_{c'c} = \sum_\lambda \frac{\gamma_{\lambda c'} \gamma_{\lambda c}}{(E_\lambda - E)}. \tag{5.29}$$

The relation between the collision function (and therefore the cross section) with the internal functions is then obtained via the R-matrix. In terms of equation 5.9 the value and derivative functions can be written as

$$V_c = \left(\frac{\hbar}{2\rho_c}\right)^{1/2} (A_c O_c + B_c I_c) \tag{5.30}$$

$$D_c = \left(\frac{\hbar \rho_c}{2}\right)^{1/2} (A_c O'_{c'} + B_c I'_{c'}), \tag{5.31}$$

and with equation 5.28 these give

$$\rho_{c'}^{-1/2}(A_{c'} O_{c'} + B_{c'} I_{c'}) = R_{c'c} \rho^{1/2}[(A_c O'_{c'} + B_c I'_{c'}) - b_c \rho_c^{-1/2}(A_c O_c + B_c I_c)]. \tag{5.32}$$

With the definition of the collision matrix (equation 5.10) one finally gets, in matrix notation,

$$U = [O\rho^{-1/2} - R(O' - \rho^{-1}bO)\rho^{1/2}]^{-1}[I\rho^{-1/2} - R(I' - bI\rho^{-1})\rho^{1/2}]. \tag{5.33}$$

5.3   The level matrix

As can be seen in equation 5.33 the calculation of the collision matrix requires the inversion of the R-matrix. When the number of channels connected to the compound is large the inversion is very time consuming. Nevertheless, there is a solution to this problem by inverting instead a "level" matrix defined in terms of the R-matrix and some other quatities we have discussed before.

Let us define the logaritmic derivative of the outgoing wave at a_c as

$$L = \left(\frac{\rho_c O'_c}{O_c} \right)_{a_c} = S_c + i P_c, \tag{5.34}$$

such that S_c and P_c are the real and imaginary part of the ratio, respectively. S_c is known as the shift factor, while P_c corresponds to the penetration factor. (The reason for the names and their physical interpretation will be provided in the next section.) In practice, simple relations for their calculation are given in terms of the Coulomb wave functions F_c and G_c (see Abramowitz and Stegun [1] for a full discussion of Coulomb functions) as follows:

$$S_c = \frac{\rho_c (F_c F'_c + G_c G'_c)}{F_c^2 + G_c^2} \tag{5.35}$$

$$P_c = \frac{\rho_c}{(F_c^2 + G_c^2)}. \tag{5.36}$$

As defined the R-matrix is a sum over the levels λ (eigenvalues) so splitting R in two level groups would give $R = R^O + R'$, where R^0 and R' are the diagonal and non-diagonal parts of the R-matrix, respectively. We define now $L^0 = L - P$ and $L' = L^0 (1 - R^0 L^0)^{-1}$. Calculating L' would require to solve the trivial problem of inverting the diagonal part R^0 of the R-matrix instead. The rule of transformation from the channel matrix (the R-matrix) to a level matrix $A_{\mu\nu}$ is then

$$(1 - R'L')^{-1} = 1 + \sum_{\mu\nu} (\gamma_\mu \times \beta_\nu) A_{\mu\nu}. \tag{5.37}$$

where γ_μ is the matrix of reduced width amplitudes and $\beta_\nu = L' \gamma_\nu$. When the number of levels is small (a very common case in nuclear astrophysics), the transformation above is extremely useful as instead of inverting a channel matrix one

102

needs to invert a small level matrix.

5.4 The physical meaning of the R-matrix parameters

When we defined the set of eigenstates X_λ in the internal region we said that they were not specific to the formation of a compound. In this sense we understand that the quantities defined in this region are particular to the theory. However, there is a connection between the "R-matrix" or "formal" parameters (the eigenvalues E_λ and the reduced width amplitudes $\gamma_{\lambda c}$) and "physical" parameters (resonance energies E_R and physical reduced width amplitudes $\gamma_{\lambda c}^{phys}$) [4], [11],and [12].

The connection equations are as follows:

$$(\gamma_{\lambda c}^{phys})^2 = \gamma_{\lambda c}^2(1 + \gamma_{\lambda c}^2 S_c')^{-1} \tag{5.38}$$

$$E_\lambda + \Delta_\lambda - E_R = 0, \tag{5.39}$$

such that S' is the derivative of the shift function with respect to the energy and the "level shift" is $\Delta_\lambda = -\gamma_\lambda^2(S(E_\lambda) - b_c)$. From equation 5.39 it is simple to deduce that the energy of the resonace would appear "shifted" with respect to the eigenvalue (formal parameter) by a factor Δ_λ unless the boundary condition is defined as $S(E_\lambda) = b_c$. On the other side, the physical partial width would be

$$\Gamma_{c\lambda}^{phys} = 2P_c(\gamma_{c\lambda}^{phys})^2. \tag{5.40}$$

We will conclude this discussion with a feature of the theory fundamental to its understanding: the relevance of the boundary conditions and the hypersurface radius. From equation 5.34 one can deduce that the real and imaginary parts of

the logaritmic derivative of the outgoing wave function depend on both the radius a_c and of course the boundary condition from equation 5.19. About the radius, as long as no nuclear reactions take place outside the hypersphere, any value can be chosen. It is customary to choose values between 5 and 6 fm; in this work we used $a_c = 5.5$ fm.

On the other hand the boundary condition b_c is taken such that $b_c = S_c$ at the eigenvalue E_{λ_0}. When this is the case, in general $b_c \neq S_c$ for $\lambda \neq \lambda_0$. This makes us conclude that while the formal parameters depend strongly on both the radius a_c and the boundary condition b_c, the physical results (parameters) are by definition independent of our choice.

5.5 The differential cross section

Here we derive the differential cross section from the amplitudes of the outgoing waves at infinity $f_{\alpha's'\nu',\alpha s\nu}(\Omega'_\alpha)$, and show that Lane and Thomas [66] have a problem with the calculation of the interference term. By definition the amplitude is given by

$$d\sigma_{\alpha's'\nu',\alpha s\nu} = |f_{\alpha's'\nu',\alpha s\nu}(\Omega'_\alpha)|^2 d\Omega_{\alpha'}. \tag{5.41}$$

By summing over the channel spins s, s' and their projections $\nu\nu'$ we get

$$d\sigma_{\alpha,\alpha} = [(2I_1 + 1)(2I_2 + 1)]^{-1} \sum_{ss'\nu\nu'} |f_{\alpha's'\nu',\alpha s\nu}(\Omega'_\alpha)|^2 d\Omega_{\alpha'}, \tag{5.42}$$

where Ω'_α is the solid angle and I_1 and I_2 are the spins of the colliding nuclei. The amplitudes are given by a Coulomb potential scattering term C_α and a resonant term K

$$f_{\alpha's'\nu',\alpha s\nu}(\Omega'_\alpha) = \frac{\pi^{1/2}}{k_\alpha}[-C_{\alpha'}(\theta_\alpha)\delta_{\alpha's'\nu',\alpha s\nu} + iK], \tag{5.43}$$

where

$$C_{\alpha'}(\theta_\alpha) = (4\pi)^{-1/2}\eta_\alpha \csc^2(\theta_\alpha/2) \exp(-2i\eta_\alpha \log\sin(\theta_\alpha/2)) \qquad (5.44)$$

and

$$K = \sum_{JMll'm'} (2l+1)^{1/2}(sl\nu0|JM)(s'l'\nu'm'|JM)T^J_{\alpha's'l',\alpha sl}Y^{l'}_{m'}(\Omega_{\alpha'}). \qquad (5.45)$$

Here J and M are the spin of the compound and its projection, l and l' the orbital angular momenta of the entrance and exit channels, respectively, $Y^{l'}_{m'}$ are spherical harmonics, and $(abcd|JM)$ are Clebsh-Gordan coefficients. The complex conjugate of the amplitude is given by

$$f^*_{\alpha's'\nu',\alpha s\nu}(\Omega'_\alpha) = \frac{\pi^{1/2}}{k_\alpha}[-C^*_{\alpha'}(\theta_\alpha)\delta_{\alpha's'\nu',\alpha s\nu} - i\sum_{JMll'm'}(2l+1)^{1/2}(sl\nu0|JM)$$

$$\times(s'l'\nu'm'|JM)T^{*J}_{\alpha's'l',\alpha sl}Y^{*l'}_{m'}(\Omega_{\alpha'})], \qquad (5.46)$$

so the square of the module is

$$|f_{\alpha's'\nu',\alpha s\nu}(\Omega'_\alpha)|^2 = f_{\alpha's'\nu',\alpha s\nu}(\Omega'_\alpha)f^*_{\alpha's'\nu',\alpha s\nu}(\Omega'_\alpha)$$

$$= \frac{\pi}{k^2_\alpha}[\Xi_1 + \Xi_2 + \Xi_3 + \Xi_4]. \qquad (5.47)$$

Here the Ξ_i's are the four terms from the product and are given by

$$\Xi_1 = C_{\alpha'}(\theta_{\alpha'})C^*_{\alpha'}(\theta_{\alpha'})\delta_{\alpha's'\nu',\alpha s\nu}\delta_{\alpha's'\nu',\alpha s\nu}, \qquad (5.48)$$

$$\Xi_2 = -i^2\sum_{JMll'm'}(2l+1)^{1/2}(sl\nu0|JM)(s'l'\nu'm'|JM)T^J_{\alpha's'l',\alpha sl}Y^{l'}_{m'}(\Omega_{\alpha'})$$

105

$$\sum_{JMll'm'} (2l+1)^{1/2}(sl\nu 0|JM)(s'l'\nu'm'|JM)T^{*J}_{\alpha's'l',\alpha sl}Y^{*l'}_{m'}(\Omega_{\alpha'}) \qquad (5.49)$$

$$\Xi_3 = iC_{\alpha'}(\theta_{\alpha'})\delta_{\alpha's'\nu',\alpha s\nu}\sum_{JMll'm'} (2l+1)^{1/2}(sl\nu 0|JM)$$

$$\times (s'l'\nu'm'|JM)T^{*J}_{\alpha's'l',\alpha sl}Y^{*l'}_{m'}(\Omega_{\alpha'}) \qquad (5.50)$$

$$\Xi_4 = -iC^*_{\alpha'}(\theta_{\alpha'})\delta_{\alpha's'\nu',\alpha s\nu}\sum_{JMll'm'} (2l+1)^{1/2}(sl\nu 0|JM)$$

$$\times (s'l'\nu'm'|JM)T^{J}_{\alpha's'l',\alpha sl}Y^{l'}_{m'}(\Omega_{\alpha'}). \qquad (5.51)$$

The first term corresponds to the Coulomb potential scattering part of the cross section, while Ξ_2 is the resonance scattering term. The part we are interested is the cross terms Ξ_3 and Ξ_4, corresponding to the interference between the potential and the resonant contributions. We now label the interference term by $IT = \Xi_3 + \Xi_4$ and the product of common factors by

$$\Lambda = \sum_{JMll'm'} (2l+1)^{1/2}(sl\nu 0|JM)(s'l'\nu'm'|JM)\delta_{\alpha's'\nu',\alpha s\nu}, \qquad (5.52)$$

so

$$IT = \Lambda[iC_{\alpha'}(\theta_{\alpha'})T^{*J}_{\alpha's'l',\alpha sl}Y^{*l'}_{m'}(\Omega_{\alpha'})$$

$$-iC^*_{\alpha'}(\theta_{\alpha'})T^{J}_{\alpha's'l',\alpha sl}Y^{l'}_{m'}(\Omega_{\alpha'})]. \qquad (5.53)$$

With some complex algebra we get

$$IT = \Lambda[iC_{\alpha'}(\theta_{\alpha'})T^{*J}_{\alpha's'l',\alpha sl}Y^{*l'}_{m'}(\Omega_{\alpha'})$$

$$+[iC_{\alpha'}(\theta_{\alpha'})T^{*J}_{\alpha's'l',\alpha sl}Y^{*l'}_{m'}(\Omega_{\alpha'})]^*$$

$$= 2\Lambda Re[iC_{\alpha'}(\theta_{\alpha'})T^{*J}_{\alpha's'l',\alpha sl}Y^{*l'}_{m'}(\Omega_{\alpha'})]. \qquad (5.54)$$

106

Now, by summing over ν and ν' the interference term is then

$$\sum_{JMll'm'\nu\nu'} IT = \sum_{JMll'm'\nu\nu'} (2l+1)^{1/2}(sl\nu0|JM)(s'l'\nu'm'|JM)\delta_{\alpha's'\nu',\alpha s\nu}$$

$$\times 2Re[iC_{\alpha'}(\theta_{\alpha'})T^{*J}_{\alpha's'l',\alpha sl}Y^{*l'}_{m'}(\Omega_{\alpha'})]$$

$$= \sum_{JMll'm'\nu} (2l+1)^{1/2}(sl\nu0|JM)(s'l'\nu m'|JM)\delta_{\alpha's'\nu',\alpha s\nu}$$

$$\times 2Re[iC_{\alpha'}(\theta_{\alpha'})T^{*J}_{\alpha's'l',\alpha sl}Y^{*l'}_{m'}(\Omega_{\alpha'})]. \tag{5.55}$$

From Blatt and Biedenharn [8],

$$\sum_{M\nu}(sl\nu0|JM)(s'l'\nu m'|JM) = \frac{2J+1}{2l+1}\delta_{l'm',l0} \tag{5.56}$$

one gets

$$\sum_{JMll'm'\nu\nu'} IT = \sum_{Jll'm'} (2l+1)^{1/2}\frac{2J+1}{2l+1}\delta_{l'm',l0}\delta_{\alpha's'\nu',\alpha s\nu}$$

$$\times 2Re[iC_{\alpha'}(\theta_{\alpha'})T^{*J}_{\alpha's'l',\alpha sl}Y^{*l'}_{m'}(\Omega_{\alpha'})]. \tag{5.57}$$

With $m' = 0$

$$\sum_{JMll'm'\nu\nu'} IT = \sum_{Jll'} (2l+1)^{1/2}\frac{2J+1}{2l+1}\delta_{l',l}\delta_{\alpha's'\nu',\alpha s\nu}$$

$$\times 2Re[iC_{\alpha'}(\theta_{\alpha'})T^{*J}_{\alpha's'l',\alpha sl}Y^{*l'}_0(\Omega_{\alpha'})]. \tag{5.58}$$

We now use the symmetry relation

$$Y^L_{-M}(\Omega) = (-1)^M Y^{L*}_M(\Omega) \tag{5.59}$$

with $M = 0$ so

$$Y_0^L(\Omega) = Y_0^{L*}(\Omega). \qquad (5.60)$$

Expanding in terms of Legendre polynomials gives

$$Y_0^L(\Omega) = \left(\frac{2L+1}{4\pi}\right)^{1/2} P_L(\cos\theta), \qquad (5.61)$$

which we apply to $Y_0^{*l'}(\Omega_{\alpha'})$ thus getting

$$Y_0^{l'*}(\Omega_{\alpha'}) = \left(\frac{2l'+1}{4\pi}\right)^{1/2} P_{l'}(\cos\theta_{\alpha'}). \qquad (5.62)$$

Replacing in equation 5.58 we finally get

$$\sum_{JMll'm'\nu\nu'} IT = \sum_{Jll'} \frac{(2J+1)}{(2l+1)^{1/2}} \delta_{l',l} \delta_{\alpha's'\nu',\alpha s\nu}$$

$$\times 2Re[iC_{\alpha'}(\theta_{\alpha'}) T_{\alpha's'l',\alpha sl}^{*J} \left(\frac{2l'+1}{4\pi}\right)^{1/2} P_{l'}(\cos\theta_{\alpha'})]$$

$$= \sum_{Jl} \frac{(2J+1)}{(4\pi)^{1/2}} \delta_{\alpha's'l',\alpha sl} 2Re[iC_{\alpha}(\theta_{\alpha}) T_{\alpha's'l',\alpha sl}^{*J} P_l(\cos\theta_{\alpha})]. \qquad (5.63)$$

In contrast, Lane and Thomas's version is

$$= \sum_{Jl} \frac{(2J+1)}{(4\pi)^{1/2}} 2Re[iC_{\alpha}(\theta_{\alpha}) T_{\alpha's'l',\alpha sl}^{J} P_l(\cos\theta_{\alpha})]. \qquad (5.64)$$

We conclude then that the interference term vanishes for channels different from the elastic.

5.6 Relating experimental data to the R-matrix theory

This section is particular to the experimental technique used in this work, described in chapter 4. An explanation of the reason for choosing this experimental technique can be done at this point where the main ingredients of the theory have been discussed.

First let us go back to equation 3.11, where the reaction rate is calculated. Is there a way of measuring experimentally the cross section for the reaction? In principle yes, but in the practice the complications would be terrible. First, as in general the products of the reaction are not emitted isotropically measuring $\sigma_{\alpha\alpha'}$ requires one to cover the whole solid angle in the center of mass system. For the case of $^{19}F(\alpha, p)^{22}Ne$ this is equivalent to be able to detect reaction products almost at 4π in the laboratory. As discussed before the reaction products need to be detected under vacuum; even if we were able to implement a detector sphere the problem of separating the protons from the huge elastic scattering background would remain unsolved. The solution was to measure differential cross sections $d\sigma/d\Omega$ with detectors covering small solid angles instead. Beside experimental considerations the first advantage one can think of is that if various angles are measured then from the angular information one can deduce spin states of the compound, required when the Breit-Wigner rate approximation (equation 3.26) is used.

The idea of applying the theory to the experimental data and extract information from it is as follows. Given a set of nuclear parameters (R-matrix energies and width amplitudes) as input to the theory, the differential cross section is calculated and compared to the experimental data. The set of input parameters describing the data is then used to evaluate the cross section out of equation 5.12.

5.7 AZURE: an A- and R-matrix analysis code

AZURE [7] is a fortran code that implements the R-matrix formalism as presented by Lane and Thomas [66]; it certainly is the most powerful R-matrix code available to date. It is flexible: it can treat several types of reactions like those involving charged particles, neutrons, and gamma rays. It is multiplataform: the code has been ported to the most popular operating systems used in scientific applications. It is fast: numerical algorithms such as matrix algebra are fully optimized. It is accurate: it has been proved to describe several experimental data sets. Finally, the code fully complies with scientific ethics as it is both free and open source.

AZURE implements the A-matrix formalism of nuclear reactions as well, so depending on the problem the user can choose the most efficient of them. As input the user provides a set of initial nuclear parameters (eigenvalues and reduced width amplitudes) for each level and channel within. The code then calculates theoretical yield curves at different angles (test mode). The code also has the capability of fitting experimental data by comparing it to its own output by means of a χ^2 analysis (this is called fitting mode). In this case the optimized set of nuclear parameters is given as an output. As extra features (fundamental for analyzing experimental datasets) both convolution (beam energy resolution) and target integration treatments of the yield curves are implemented as well.

5.8 Analysis of the yield curves

From simple examination of the experimental excitation curves in the appendix one can easily verify the complexity of the data. First the density of resonances is high; on the other hand regions between resonances usually show complex inter-

ference patterns. Although not evident from the plots, in some regions the curves also show a pronounced angular dependent structure.

The first step in our procedure was to look in the literature for information on the compound nucleus at the excitation energies relevant to the energy of our experiments. The only source of information comes from an experiment performed in 1968 at Duke University by Keyworth et al. [61]. Their experiments were a spectroscopic study of the elastic and inelastic scattering (to the first excited state in the target) of protons on a ^{22}Ne gas. Particularly impressive is the beam energy resolution (250 eV) they were able to achieve. They covered the energy region between 2.0 and 3.1 MeV at several angles and were able to find 76 resonances and determine most of the spins and parities.

For the analysis of the experimental data we used AZURE running on a Linux plataform. The input file consisted of a list of 44 excited states in the compound with both their spins and parities for three channels: the elastic of $^{4}He + ^{19}F$ and both p_0 and p_1 channels. As discussed before for each state four nuclear parameters were varied in order to reproduce the experimental data: the energy and a reduced width amplitude for each of the three channels. Besides, each of the reduced width amplitudes carries a sign that determines the interference between resonances in a unique way. As an extra parameter we included a renormalization factor for the whole set of data points; as both channels were always measured simultaneously only one parameter was used.

The cross section calculation described in the theory assume that the target is composed of a single layer of nuclei. Nevertheless real targets have a finite thickness so the energy of the projectile nuclei is spread out through the target thickness. This effect has been implemented in AZURE by calculating the cross

sections at energies corresponding to different layers in the target. This means that every point in the excitation function has a contribution from all the layers in the target. This is a simple way of evaluating the integral from equation 4.13. For the analysis a target thickness of 25 keV was used at all energies.

In the next chapter we describe the results of the R-matrix analysis of the experimental data and its implications.

CHAPTER 6

RESULTS

In this chapter we present the results of the R-matrix analysis of the experimental data. The set of formal parameters is given and from it an extrapolation of the reduced alpha widths is performed; with the results a new reaction rate is evaluated. Upper and lower limits for the rate are provided and a comparison with Caughlan and Fowler's rate is given. Finally the implications the new rate has in the nucleosynthesis of fluorine in stellar environments are discussed.

6.1   R-matrix analysis results

AZURE has the feature of letting the user to switch on and off resonances within the input file so even though present, they could be left out of a calculation. In this way we started the analysis by selecting the levels that should have a strong influence in the measured curves: wherever we could see a peak in the curve we turned on a level. As the set of input parameters are R-matrix parameters as opposed to the physical set that would be reflected in the excitation curves we adjusted the energies by hand to get the peaks at the right position. The most complicated part to reproduce in the experimental curves was always the interference between the resonances. As the interference only appears between resonances of the same J^π (spin and parity) we worked in groups of these, turning

off all resonances with different values. Within a single J^π, we worked in pairs of levels trying to understand how one resonance affects the others in the group. We tried to find out the strongest conditions in the group governing a reasonable trend. Once the signs of the reduced width amplitudes were determined, we turned on two groups of J^π at the same time and worked for all possible pairs of J^π. Finally we turned on the levels for all J^π and varied the parameters one at a time. All the steps were performed iteratively, i.e. they were repeated several times until a local minimum in χ^2 was achieved. Every time a calculation was performed all 20 excitation curves were examined. Most of the time an improvement in the fit for one of the curves affected negatively the others.

Data fits are shown in the appendix and table A.3 lists the resulting parameters. Both the energies E_λ and the reduced width amplitudes γ_i are formal parameters for an R-matrix radius $a_c = 5.5$ fm and the boundary condition set to S_c at the first level listed in a J^π group. The constant of renormalization for the experimental yields was 0.15243×10^6.

On the other hand levels of ^{23}Na as compiled by Endt in [29] that were included in the analysis but only assigned an upper limit to their reduced alpha widths $(\gamma_\alpha^2 < 4.0 \times 10^{-5} MeV)$ are listed in table A.4 of the appendix.

6.2   The new reaction rate

The evaluation of the rate was performed from determining the strengths $\omega\gamma$ in equation 3.27 for the single resonances,

$$\omega\gamma = \frac{(2J+1)}{2} \cdot \frac{\Gamma_\alpha \Gamma_p}{\Gamma_{tot}},\tag{6.1}$$

and using the approximation $\gamma = \Gamma_\alpha$, valid for $\Gamma_\alpha << \Gamma_p$.

114
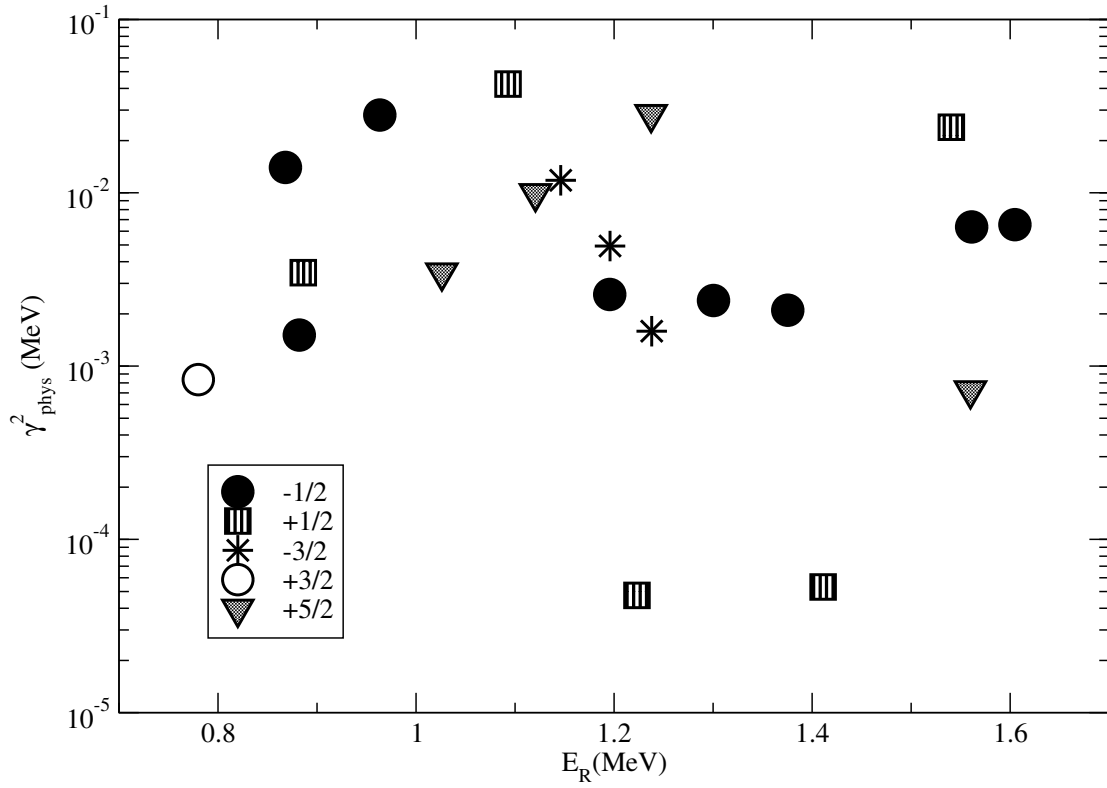
Figure 6.1. The experimentally determined γ^2_α presented in sets of J^π, as suggested by equation 5.17 where the internal eigenfunctions depend on the spin of the compound. The vertical span of the data reflects the reaction rate interval presented in figure 6.2.
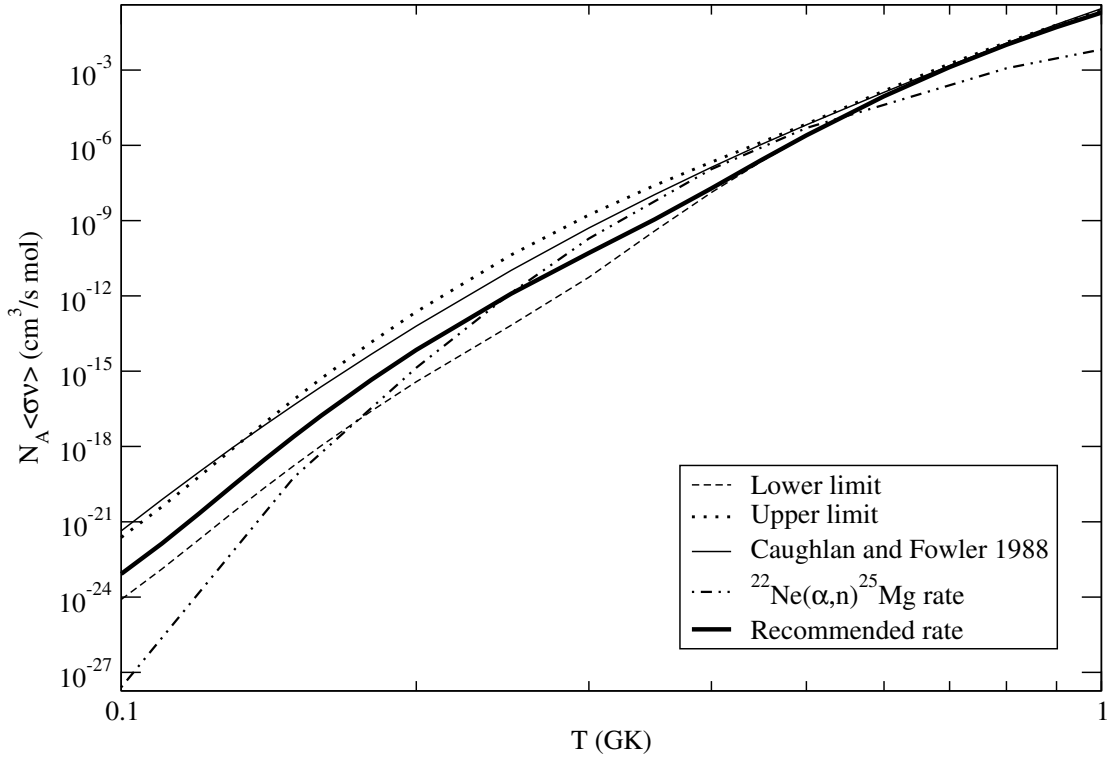
Figure 6.2. The new rate for the $^{19}F(\alpha, p)^{22}Ne$ reaction compared to
Caughlan and Fowler's rate

For resonances with energies above 782 keV we used the values from table A.3 transformed to physical parameters with equations 5.39; Γ_α was then calculated with equation 5.40. On the other hand, for energies below 782 keV extrapolated reduced alpha widths were used; these were obtained by averaging the values above 782 keV (figure 6.1) in groups of J^π and for each resonance observed in the $^{22}Ne(p,p)^{22}Ne$ and $^{22}Ne(p,p')^{22}Ne$ set of experiments by Keyworth [61] a partial width was obtained. The upper limits to the reduced alpha widths from table A.4 were included as well when calculating the average value used for the extrapolation.

The upper limit for the reaction rate was calculated by setting the extrapolated

reduced alpha width equal to the highest γ_α^2 value determined from the experimental data for each of the J^π groups. On the other hand the lower limit to the rate was calculated by extrapolating for all J^π groups with $\gamma_\alpha^2 < 4.0 \times 10^{-5} MeV$, the upper value assigned to the resonances listed in table A.4. The result is shown in figure 6.2 and compared to Caughlan and Fowler's rate; our recommended value of the rate is one order of magnitude smaller. Upper and lower limits together with the recommended rate are tabulated in the appendix. (A reader interested in rate values for energies not listed in the table should contact the author.)

6.3 The consequences of the new rate for the nucleosynthesis of fluorine in stellar environments

An order of magnitude reduction in the reaction rate leads immediatly to investigating the importance of competing reactions destroying fluorine in AGB and Wolf-Rayet stars. As shown in figure 6.2 for temperatures over $2.5 \times 10^8 K$ the $^{22}Ne(\alpha,n)^{25}Mg$ rate dominates over the $^{19}F(\alpha,p)^{22}Ne$ rate, suggesting that $^{19}F(n,\gamma)^{20}F$ may be an important process. In this section we discuss a study of a comparative relevance of these two reactions; we have selected four models of AGB stars with different masses and metalicities. The stellar structure is calculated with the Mount Stromlo Stellar Structure Program (MSSSP) and then the nucleosynthesis with the post processing code MOSN (Monash Stellar Nucleosynthesis Code)(Details are given in Lugaro[70] and Karakas[58]). We have obtained yields of fluorine for the different models turning on and off the two reactions and comparing the results.

Specific to our work, the models reproduce the TDU (third dredge up) self-consistently after some pulses, while other codes have to parameterize it artificially.

We also carry the nucleosynthesis calculation through all the pulsating cycles by including always a partial mixing zone (PMZ) and computing the abundances of nuclear species up to iron. When convection needs to be computed the mixing and nucleosynthesis processes are solved simultaneously; mixing is time-dependent thus no "instantaneous" processes are allowed. The nuclear network we use consists of 59 nuclei ranging from protons to sulphur and 14 iron-like nuclei. Nuclei heavier than $A = 61$ are treated as a single particle that simulates captures of neutrons into s-process nuclei. Our initial abundances are taken from Anders and Grevesse [3] and 506 reactions included with rates mostly from REACLIB[91] and from chapter 3.

One of the most controvesial issues in nuleosynthesis of AGB stars is the introduction of a PMZ at the end of the TDU. As discussed in chapter 2 several possibilities justifying it are now available. The construction of toy models in the laboratory for testing convective overshooting [50] may be one of the first possibilities for settling this problem. However, in our calculations we have ignored the mechanism leading to a PMZ and we introduce this region artificially via the postprocessing code after the TDU. Even more complicated is the profile of the proton abundance in the PMZ; we have chosen to include a profile decaying exponentially into the helium intershell.

The calculations were done at the Institute for Computational Astrophysics in Saint Mary's University's and at Cambridge University's Institute of Astronomy. The four models chosen correspond to a) $M = 3M_\odot$ and $Z = 0.02$, b) $M = 3M_\odot$ and $Z = 0.008$, c) $M = 2M_\odot$ and $Z = 0.0001$, and d) $M = 5M_\odot$ and $Z = 0.02$, such that M is the mass of the star in units of $M_\odot$, the solar mass, and Z the metalicity. All models were calculated both with our version and Caughlan and

Fowler's version of the $^{19}F(\alpha, p)^{22}Ne$ rate.

In all models, the contribution to fluorine destruction is as follows: with CF88 $^{19}F(\alpha, p)^{22}Ne$ is responsible for destroying fluorine by 50%, while $^{19}F(n, \gamma)^{20}F$ destroys the other 50%. In contrast with our new rate $^{19}F(\alpha, p)^{22}Ne$ destroys only 10% while $^{19}F(n, \gamma)^{20}F$ is the main source of fluorine destruction by 90%. In particular, the model where the maxiumum destruction of fluorine by the $^{19}F(\alpha, p)^{22}Ne$ mechanism is model d) with 17%.

The change in the fluorine yield from the Caughlan and Fowler rate to our new recommended values is, for model a) an increase of 24%, for model b) an increase of 40%, for model c) an increase of 43%, and finally for model d) the fluorine yield is larger by a factor of 3.7. Models b) and c) correspond to the largest producers of fluorine.

With the new rate and by removing the $^{19}F(n, \gamma)^{20}F$ reaction artificially from the reaction network we get fluorine yield changes of +18% for model a), +35% for model b), +28% for model c), and a factor of 2.2 increase for model d). About 10% of the $^{19}F(n, \gamma)^{20}F$ destruction occurs in the ^{13}C pocket. The neutrons necessary for this reaction to take place come from $^{22}Ne(\alpha, n)^{25}Mg$. A new estimate for the rate of this reaction has been performed and will be published soon [59]; the importance of the $^{19}F(n, \gamma)^{20}F$ reaction can also be deduced by comparing the rates of $^{22}Ne(\alpha, n)^{25}Mg$ and $^{19}F(\alpha, p)^{22}Ne$ for temperatures around 0.3 GK (see figure 6.2). On the other hand, the contribution from the $^{19}F(p, \alpha)^{16}O$ was always found to be of marginal relevance to the destruction of fluorine. It still remains to investigate the effects the uncertainty in the new rate pose to the nucleosynthesis of fluorine.

Very recently Stancliffe et al. [90] have evaluated the effect the new rate rate

has in Wolf-Rayet stars. A model of a star with $M = 60 M_\odot$ and $Z = 0.02$ was evolved from the pre-main sequence to the WR phase with Eggleton's code STARS [28]. The initial abundances were taken from Anders and Grevesse [3] and the mass loss rates from de Jager et al. [21] for the pre Wolf-Rayet phase and of Langer [67] for the WR phase; no convective overshoot was included in the model. It was concluded that, for a given rate, the yield is a factor of 4 smaller compared to the Meynet and Arnould [75] estimate, where an enhanced mass loss rate was used at the WR phase. On the other hand, it was concluded that the $^{19}F(n,\gamma)^{20}F$ reaction contributes importantly to the destruction of fluorine in these stellar environments.

CHAPTER 7

CONCLUSIONS

Two of the most interesting questions I have been asked about this project will be discussed in this section. The first one was asked during the XXVIII Symposium on Nuclear Physics in Cocoyoc, Mexico by Prof. María Ester Brandan: "how does your results help us understand fluorine on Earth?" Some months ago I was given by Dr. Maria Lugaro her new book about meteoritic presolar grains; there she explains how scientists struggle in the laboratory to extract presolar grains from meteorites. These grains are thought to have the unique characteristic of having been formed before our solar system and for instance carry information from the progenitor of the Sun and planets. In principle everything around does, but with the difference that presolar grains were isolated from the environment right after they were formed; they have never been subject to untraceable mixing processes like the Earth so their isotopic abundances may really reflect the composition of the stellar environment at the time of formation. In order to explain the isotopic abundances found on Earth we need first to understand how the planet was formed.

The other question was asked by Prof. Umesh Garg while my progress with the nuclear physics analysis was being examined. He asked me about the reproducibility in the analysis and uniqueness of the set of nuclear parameters obtained: "If I make the analysis myself, would I come out with the same [formal] parameters as

you did?". The answer is no in general, as these are dependent on the selection of both the boundary conditions and the channel radius . For different conditions the values from the theory will in general be different from what we show in table A.3. However, when the sets of physical parameters are compared, they must be the same for all choices of boundary conditions.

We have traced the origin of the reaction rate currently in use for the $^{19}\text{F}(\alpha, p)^{22}\text{Ne}$ reaction. A summary of some of the most relevant recent work trying to find the nucleosynthetic origin of fluorine has been given. Reaction rates of importance to the synthesis of this element were updated: in particular the $^{14}C(\alpha, \gamma)^{18}O$ reaction rate from current compilations was found to have a problem. On the experimental aspect we were able to sucessfully develop a fluorine target that could stand very high beam intensities. We measured the $^{19}\text{F}(\alpha, p)^{22}\text{Ne}$ reaction down to energies never studied before and several resonances were discovered in both the $^{19}\text{F}(\alpha, p_0)^{22}\text{Ne}$ and $^{19}\text{F}(\alpha, p_1)^{22}\text{Ne}$ channels. We also proved that the interference term in the calculation of the differential cross section from Lane and Thomas's work is incomplete. We have also shown that $^{19}\text{F}(\alpha, p)^{22}\text{Ne}$ is a case where the rate can not be treated in the framework of models based in the continuum, such as the Hauser-Feshbach statistical model. Finally we concluded that the $^{19}\text{F}(\alpha, p)^{22}\text{Ne}$ reaction may not be the most important mechanism of destruction of fluorine in AGB stars; the $^{19}F(n, \gamma)^{20}F$ reaction seems to be of more relevance. A detailed review of these results can be found in [98].

Future work still needs to be done trying to unveil the synthesis of fluorine mechanisms in the universe. For example, it is fundamental to look for fluorine in supernovae remnants and in Wolf-Rayet stars. Also the mixing of protons into the helium intershell in AGB stars needs to be understood. More specific

122

to this work, the full Gamow window of the ^{19}F$(\alpha, p)^{22}$Ne reaction needs to be investigated. This may require higher beam intensities from the ones used here; the stability of the fluorine targets was not taken to its limit in this work, so it is very likely that they will perform well. However, the target thickness can still be improved; an ion source in better working conditions would be ideal for this. The R-matrix analysis still needs input from other channels that may also form the compound state; for example, the elastic and inelastic scattering of ^4He on ^{19}F needs to be measured and analyzed simultaneously with AZURE. The elastic and inelastic data for $p +^{22} Ne$ is also available and should be included in the analysis as well. To conclude, we urge experimenters to start investigation on the $^{19}F(n, \gamma)^{20}F$ reaction as a new mechanism of destruction of fluorine in AGB and probably Wolf-Rayet stars.

APPENDIX A

TABLES

TABLE A.1

REACTION RATE FOR $^{14}C(\alpha, \gamma)^{18}O$

T_9	recomm	lower	upper
0.10	9.138E-16	4.153E-20	1.820E-15
0.15	4.682E-13	2.116E-16	9.326E-13
0.20	9.370E-12	4.498E-14	1.862E-11
0.25	5.418E-11	2.113E-12	1.058E-10
0.30	2.901E-10	1.172E-10	4.618E-10
0.35	1.122E-08	9.055E-09	1.337E-08
0.40	3.434E-07	2.837E-07	4.032E-07
0.50	4.193E-05	3.465E-05	4.922E-05
0.60	9.856E-04	8.142E-04	1.157E-03
0.70	9.073E-03	7.496E-03	1.065E-02
0.80	4.672E-02	3.859E-02	5.484E-02
0.90	1.639E-01	1.354E-01	1.923E-01
1.0	4.405E-01	3.639E-01	5.171E-01

TABLE A.1

Continued

T_9	recomm	lower	upper
1.5	7.786E+00	6.424E+00	9.148E+00
2.0	3.190E+01	2.616E+01	3.765E+01
2.5	7.798E+01	6.315E+01	9.281E+01
3.0	1.491E+02	1.190E+02	1.793E+02
3.5	2.448E+02	1.925E+02	2.972E+02
4.0	3.604E+02	2.800E+02	4.409E+02
4.5	4.889E+02	3.760E+02	6.017E+02
5.0	6.228E+02	4.752E+02	7.704E+02
6.0	8.838E+02	6.664E+02	1.101E+03
7.0	1.112E+03	8.315E+02	1.392E+03
8.0	1.295E+03	9.632E+02	1.628E+03
9.0	1.435E+03	1.062E+03	1.807E+03
10.0	1.534E+03	1.132E+03	1.937E+03

TABLE A.2

REACTION RATE FOR $^{18}O(\alpha,\gamma)^{22}Ne$

T_9	recomm	lower	upper
0.10	3.573E-20	1.333E-20	1.076E-19
0.15	2.955E-14	1.972E-14	3.942E-14
0.20	3.329E-11	2.260E-11	4.398E-11
0.25	2.600E-09	1.894E-09	3.305E-09
0.30	6.540E-08	5.258E-08	7.822E-08
0.35	8.445E-07	7.233E-07	9.657E-07
0.40	6.470E-06	5.711E-06	7.230E-06
0.50	1.229E-04	1.107E-04	1.351E-04
0.60	8.900E-04	8.058E-04	9.740E-04
0.70	3.622E-03	3.282E-03	3.958E-03
0.80	1.024E-02	9.274E-03	1.119E-02
0.90	2.279E-02	2.058E-02	2.489E-02
1.00	4.302E-02	3.872E-02	4.699E-02
1.50	3.180E-01	2.781E-01	3.492E-01
2.00	1.150E+00	9.828E-01	1.276E+00
2.50	3.043E+00	2.579E+00	3.406E+00
3.00	6.309E+00	5.338E+00	7.100E+00
3.50	1.087E+01	9.199E+00	1.228E+01
4.00	1.637E+01	1.386E+01	1.853E+01
4.50	2.238E+01	1.896E+01	2.538E+01
5.00	2.851E+01	2.416E+01	3.236E+01

TABLE A.2

Continued

T_9	recomm	lower	upper
6.00	4.002E+01	3.394E+01	4.550E+01
7.00	4.961E+01	4.208E+01	5.645E+01
8.00	5.696E+01	4.832E+01	6.485E+01
9.00	6.224E+01	5.282E+01	7.090E+01
10.0	6.580E+01	5.584E+01	7.498E+01

TABLE A.3

FORMAL PARAMETERS FOR $^{19}F(\alpha,p)^{22}Ne$

J	π	$E_\lambda(MeV)$	i	s	l	$\gamma_i(MeV^{1/2})$
$\frac{1}{2}$	-	11.469	α	$\frac{1}{2}$	1	-3.86E-002
$\frac{1}{2}$	-	11.469	p_0	$\frac{1}{2}$	1	-2.73E-001
$\frac{1}{2}$	-	11.469	p_1	$\frac{3}{2}$	1	-8.16E-001
$\frac{1}{2}$	-	11.469	p_1	$\frac{5}{2}$	3	2.54E+000
$\frac{1}{2}$	-	11.330	α	$\frac{1}{2}$	1	1.10E-001
$\frac{1}{2}$	-	11.330	p_0	$\frac{1}{2}$	1	-4.89E-003
$\frac{1}{2}$	-	11.330	p_1	$\frac{3}{2}$	1	-1.18E+000
$\frac{1}{2}$	-	11.330	p_1	$\frac{5}{2}$	3	-1.16E+000
$\frac{1}{2}$	-	11.499	α	$\frac{1}{2}$	1	-3.55E-003

Continued

J	π	$E_\lambda(MeV)$	i	s	l	$\gamma_i(MeV^{1/2})$
$\frac{1}{2}$	-	11.499	p_0	$\frac{1}{2}$	1	3.87E-001
$\frac{1}{2}$	-	11.499	p_1	$\frac{3}{2}$	1	8.57E-001
$\frac{1}{2}$	-	11.499	p_1	$\frac{5}{2}$	3	1.12E+000
$\frac{1}{2}$	-	11.676	α	$\frac{1}{2}$	1	-6.09E-002
$\frac{1}{2}$	-	11.676	p_0	$\frac{1}{2}$	1	-4.34E-002
$\frac{1}{2}$	-	11.676	p_1	$\frac{3}{2}$	1	-3.54E-001
$\frac{1}{2}$	-	11.676	p_1	$\frac{5}{2}$	3	-3.54E-001
$\frac{1}{2}$	-	11.788	α	$\frac{1}{2}$	1	2.93E-002
$\frac{1}{2}$	-	11.788	p_0	$\frac{1}{2}$	1	1.30E-001
$\frac{1}{2}$	-	11.788	p_1	$\frac{3}{2}$	1	-6.24E-002
$\frac{1}{2}$	-	11.788	p_1	$\frac{5}{2}$	3	-6.24E-002
$\frac{1}{2}$	-	11.857	α	$\frac{1}{2}$	1	-2.59E-002
$\frac{1}{2}$	-	11.857	p_0	$\frac{1}{2}$	1	-3.54E-002
$\frac{1}{2}$	-	11.857	p_1	$\frac{3}{2}$	1	3.84E-001
$\frac{1}{2}$	-	11.857	p_1	$\frac{5}{2}$	3	5.60E-001
$\frac{1}{2}$	-	12.043	α	$\frac{1}{2}$	1	1.73E-001
$\frac{1}{2}$	-	12.043	p_0	$\frac{1}{2}$	1	1.20E-001
$\frac{1}{2}$	-	12.043	p_1	$\frac{3}{2}$	1	-1.44E-001
$\frac{1}{2}$	-	12.043	p_1	$\frac{5}{2}$	3	-1.44E-001
$\frac{1}{2}$	-	12.078	α	$\frac{1}{2}$	1	-9.11E-002
$\frac{1}{2}$	-	12.078	p_0	$\frac{1}{2}$	1	-9.23E-002

TABLE A.3

Continued

J	π	$E_\lambda(MeV)$	i	s	l	$\gamma_i(MeV^{1/2})$
$\frac{1}{2}$	-	12.078	p_1	$\frac{3}{2}$	1	-6.61E-002
$\frac{1}{2}$	-	12.078	p_1	$\frac{5}{2}$	3	-6.61E-002
$\frac{1}{2}$	+	11.346	α	$\frac{1}{2}$	0	8.35E-002
$\frac{1}{2}$	+	11.346	p_0	$\frac{1}{2}$	0	-2.06E-001
$\frac{1}{2}$	+	11.346	p_1	$\frac{3}{2}$	2	8.22E-001
$\frac{1}{2}$	+	11.346	p_1	$\frac{5}{2}$	2	1.60E+000
$\frac{1}{2}$	+	11.571	α	$\frac{1}{2}$	0	2.09E-001
$\frac{1}{2}$	+	11.571	p_0	$\frac{1}{2}$	0	-6.38E-002
$\frac{1}{2}$	+	11.571	p_1	$\frac{3}{2}$	2	-1.48E-001
$\frac{1}{2}$	+	11.571	p_1	$\frac{5}{2}$	2	-1.50E-003
$\frac{1}{2}$	+	11.692	α	$\frac{1}{2}$	0	-6.89E-003
$\frac{1}{2}$	+	11.692	p_0	$\frac{1}{2}$	0	9.10E-004
$\frac{1}{2}$	+	11.692	p_1	$\frac{3}{2}$	2	-2.79E-002
$\frac{1}{2}$	+	11.692	p_1	$\frac{5}{2}$	2	-2.79E-002
$\frac{1}{2}$	+	11.957	α	$\frac{1}{2}$	0	-9.50E-003
$\frac{1}{2}$	+	11.957	p_0	$\frac{1}{2}$	0	-1.40E-002
$\frac{1}{2}$	+	11.957	p_1	$\frac{3}{2}$	2	-8.15E-001
$\frac{1}{2}$	+	11.957	p_1	$\frac{5}{2}$	2	-2.69E-001
$\frac{1}{2}$	+	12.055	α	$\frac{1}{2}$	0	9.74E-002
$\frac{1}{2}$	+	12.055	p_0	$\frac{1}{2}$	0	-7.80E-002
$\frac{1}{2}$	+	12.055	p_1	$\frac{3}{2}$	2	-2.95E-001

TABLE A.3

Continued

J	π	$E_\lambda(MeV)$	i	s	l	$\gamma_i(MeV^{1/2})$
$\frac{1}{2}$	$+$	12.055	p_1	$\frac{5}{2}$	2	3.05E-001
$\frac{3}{2}$	-	11.616	α	$\frac{1}{2}$	1	-9.69E-002
$\frac{3}{2}$	-	11.616	p_0	$\frac{1}{2}$	1	-6.13E-002
$\frac{3}{2}$	-	11.616	p_1	$\frac{3}{2}$	1	-1.10E-001
$\frac{3}{2}$	-	11.616	p_1	$\frac{3}{2}$	3	-1.10E-001
$\frac{3}{2}$	-	11.616	p_1	$\frac{5}{2}$	1	-1.10E-001
$\frac{3}{2}$	-	11.616	p_1	$\frac{5}{2}$	3	-1.10E-001
$\frac{3}{2}$	-	11.677	α	$\frac{1}{2}$	1	8.17E-002
$\frac{3}{2}$	-	11.677	p_0	$\frac{1}{2}$	1	-5.30E-002
$\frac{3}{2}$	-	11.677	p_1	$\frac{3}{2}$	1	-1.23E-001
$\frac{3}{2}$	-	11.677	p_1	$\frac{3}{2}$	3	-1.23E-001
$\frac{3}{2}$	-	11.677	p_1	$\frac{5}{2}$	1	-1.23E-001
$\frac{3}{2}$	-	11.677	p_1	$\frac{5}{2}$	3	-1.23E-001
$\frac{3}{2}$	-	11.720	α	$\frac{1}{2}$	1	-3.99E-002
$\frac{3}{2}$	-	11.720	p_0	$\frac{1}{2}$	1	-9.24E-002
$\frac{3}{2}$	-	11.720	p_1	$\frac{3}{2}$	1	-8.24E-002
$\frac{3}{2}$	-	11.720	p_1	$\frac{3}{2}$	3	-8.24E-002
$\frac{3}{2}$	-	11.720	p_1	$\frac{5}{2}$	1	-8.24E-002
$\frac{3}{2}$	-	11.720	p_1	$\frac{5}{2}$	3	-8.24E-002
$\frac{3}{2}$	$+$	11.500	α	$\frac{1}{2}$	2	1.33E-001
$\frac{3}{2}$	$+$	11.500	p_0	$\frac{1}{2}$	2	4.14E-001

TABLE A.3

Continued

J	π	$E_\lambda(MeV)$	i	s	l	$\gamma_i(MeV^{1/2})$
$\frac{3}{2}$	$+$	11.500	p_1	$\frac{3}{2}$	0	-1.64E-001
$\frac{3}{2}$	$+$	11.500	p_1	$\frac{3}{2}$	2	-1.01E-001
$\frac{3}{2}$	$+$	11.500	p_1	$\frac{5}{2}$	2	-5.61E-002
$\frac{3}{2}$	$+$	11.500	p_1	$\frac{5}{2}$	4	-9.62E-001
$\frac{3}{2}$	$+$	12.400	α	$\frac{1}{2}$	2	8.31E-002
$\frac{3}{2}$	$+$	12.400	p_0	$\frac{1}{2}$	2	2.76E-001
$\frac{3}{2}$	$+$	12.400	p_1	$\frac{3}{2}$	0	-5.31E-002
$\frac{3}{2}$	$+$	12.400	p_1	$\frac{3}{2}$	2	2.36E-001
$\frac{3}{2}$	$+$	12.400	p_1	$\frac{5}{2}$	2	5.64E-001
$\frac{3}{2}$	$+$	12.400	p_1	$\frac{5}{2}$	4	1.07E+000
$\frac{5}{2}$	$+$	11.507	α	$\frac{1}{2}$	2	-4.89E-002
$\frac{5}{2}$	$+$	11.507	p_0	$\frac{1}{2}$	2	2.20E-001
$\frac{5}{2}$	$+$	11.507	p_1	$\frac{3}{2}$	2	-1.64E-001
$\frac{5}{2}$	$+$	11.507	p_1	$\frac{3}{2}$	4	-1.64E-001
$\frac{5}{2}$	$+$	11.507	p_1	$\frac{5}{2}$	0	-1.64E-001
$\frac{5}{2}$	$+$	11.507	p_1	$\frac{5}{2}$	2	-1.64E-001
$\frac{5}{2}$	$+$	11.594	α	$\frac{1}{2}$	2	-9.99E-002
$\frac{5}{2}$	$+$	11.594	p_0	$\frac{1}{2}$	2	7.48E-002
$\frac{5}{2}$	$+$	11.594	p_1	$\frac{3}{2}$	2	-5.81E-002
$\frac{5}{2}$	$+$	11.594	p_1	$\frac{3}{2}$	4	-5.81E-002
$\frac{5}{2}$	$+$	11.594	p_1	$\frac{5}{2}$	0	-5.81E-002

TABLE A.3

Continued

J	π	$E_\lambda(MeV)$	i	s	l	$\gamma_i(MeV^{1/2})$
$\frac{5}{2}$	$+$	11.594	p_1	$\frac{5}{2}$	2	-5.81E-002
$\frac{5}{2}$	$+$	11.708	α	$\frac{1}{2}$	2	1.89E-001
$\frac{5}{2}$	$+$	11.708	p_0	$\frac{1}{2}$	2	-2.00E-001
$\frac{5}{2}$	$+$	11.708	p_1	$\frac{3}{2}$	2	-8.90E-002
$\frac{5}{2}$	$+$	11.708	p_1	$\frac{3}{2}$	4	-8.90E-002
$\frac{5}{2}$	$+$	11.708	p_1	$\frac{5}{2}$	0	-8.90E-002
$\frac{5}{2}$	$+$	11.708	p_1	$\frac{5}{2}$	2	-8.90E-002
$\frac{5}{2}$	$+$	12.069	α	$\frac{1}{2}$	2	1.30E-004
$\frac{5}{2}$	$+$	12.069	p_0	$\frac{1}{2}$	2	-4.25E-002
$\frac{5}{2}$	$+$	12.069	p_1	$\frac{3}{2}$	2	-7.37E-001
$\frac{5}{2}$	$+$	12.069	p_1	$\frac{3}{2}$	4	-7.37E-001
$\frac{5}{2}$	$+$	12.069	p_1	$\frac{5}{2}$	0	-7.37E-001
$\frac{5}{2}$	$+$	12.069	p_1	$\frac{5}{2}$	2	-7.37E-001

TABLE A.4

LEVELS IN ^{23}Na WITH $\gamma_\alpha^2 < 4.0 \times 10^{-5}$ MeV

J	π	$E_\lambda(MeV)$
$\frac{1}{2}$	$+$	11.295
$\frac{3}{2}$	$-$	11.238
$\frac{3}{2}$	$-$	11.267
$\frac{3}{2}$	$-$	11.335
$\frac{3}{2}$	$+$	11.111
$\frac{3}{2}$	$+$	11.198
$\frac{3}{2}$	$+$	11.273
$\frac{3}{2}$	$+$	11.277
$\frac{3}{2}$	$+$	11.280
$\frac{3}{2}$	$+$	11.303
$\frac{3}{2}$	$+$	11.336
$\frac{5}{2}$	$+$	11.334
$\frac{5}{2}$	$+$	11.525
$\frac{5}{2}$	$+$	11.549
$\frac{7}{2}$	$-$	11.490
$\frac{7}{2}$	$-$	11.748

TABLE A.5

REACTION RATE FOR $^{19}F(\alpha,p)^{22}Ne$

T_9	recomm	lower	upper
0.10	8.435E-24	8.036E-25	2.382E-22
0.11	1.358E-22	1.307E-23	3.936E-21
0.12	2.094E-21	1.934E-22	6.172E-20
0.13	2.794E-20	2.364E-21	8.266E-19
0.14	2.973E-19	2.267E-20	8.812E-18
0.15	2.503E-18	1.728E-19	7.474E-17
0.16	1.702E-17	1.080E-18	5.158E-16
0.18	4.595E-16	2.607E-17	1.455E-14
0.20	7.033E-15	3.795E-16	2.336E-13
0.25	1.230E-12	6.825E-14	4.346E-11
0.30	5.155E-11	5.533E-12	1.681E-09
0.35	1.113E-09	3.863E-10	2.529E-08
0.40	1.929E-08	1.318E-08	2.145E-07
0.45	2.612E-07	2.285E-07	1.332E-06
0.50	2.511E-06	2.385E-06	7.137E-06
0.60	9.083E-05	8.988E-05	1.479E-04
0.70	1.307E-03	1.303E-03	1.771E-03
0.80	1.014E-02	1.012E-02	1.277E-02
0.90	5.154E-02	5.152E-02	6.274E-02

TABLE A.6

EXPERIMENTAL DATASET FOR $^{19}F(\alpha, p_0)^{22}Ne$

$E_{lab}(MeV)$	θ_{lab}	$Yield$	$dYield$
1.98058E+00	130.0	6.81710E-01	5.93820E-02
1.97596E+00	130.0	5.21082E-01	4.88417E-02
1.97135E+00	130.0	4.49909E-01	4.23396E-02
1.96570E+00	130.0	7.26258E-01	5.48706E-02
1.96089E+00	130.0	1.19533E+00	8.17919E-02
1.95567E+00	130.0	1.44667E+00	9.81354E-02
1.95108E+00	130.0	1.41196E+00	8.92114E-02
1.93611E+00	130.0	4.68961E-01	4.45879E-02
1.93113E+00	130.0	3.72922E-01	3.13034E-02
1.92574E+00	130.0	3.19211E-01	3.54005E-02
1.92574E+00	130.0	3.18836E-01	4.17338E-02
1.92078E+00	130.0	3.84130E-01	3.92028E-02
1.91582E+00	130.0	4.80215E-01	4.51135E-02
1.91086E+00	130.0	6.17263E-01	5.66374E-02
1.90571E+00	130.0	7.83451E-01	6.35823E-02
1.90118E+00	130.0	1.14357E+00	7.73564E-02
1.89584E+00	130.0	1.59761E+00	1.17682E-01
1.89112E+00	130.0	2.78919E+00	1.58132E-01
1.88620E+00	130.0	3.24228E+00	2.05640E-01
1.88026E+00	130.0	4.61962E+00	1.15555E-01
1.87597E+00	130.0	4.89980E+00	1.38641E-01

TABLE A.6

Continued

$E_{lab}(MeV)$	θ_{lab}	$Yield$	$dYield$
1.87086E+00	130.0	3.91522E+00	2.11642E-01
1.86597E+00	130.0	3.11993E+00	1.58648E-01
1.87127E+00	130.0	4.27867E+00	1.68617E-01
1.86637E+00	130.0	3.73671E+00	1.96358E-01
1.86108E+00	130.0	2.25575E+00	1.16266E-01
1.85579E+00	130.0	1.59754E+00	7.42815E-02
1.85092E+00	130.0	1.08207E+00	5.45433E-02
1.84605E+00	130.0	7.60055E-01	4.01501E-02
1.84078E+00	130.0	5.66780E-01	2.84164E-02
1.83471E+00	130.0	5.02823E-01	2.31176E-02
1.82906E+00	130.0	3.34002E-01	1.53214E-02
1.82402E+00	130.0	2.52926E-01	1.10657E-02
1.81878E+00	130.0	3.31581E-01	1.62632E-02
1.81376E+00	130.0	2.65420E-01	1.35752E-02
1.80834E+00	130.0	2.47773E-01	1.48611E-02
1.80413E+00	130.0	1.76058E-01	1.01500E-02
1.79872E+00	130.0	1.67289E-01	1.07983E-02
1.79352E+00	130.0	1.40311E-01	9.70404E-03
1.78833E+00	130.0	1.47903E-01	1.04013E-02
1.78374E+00	130.0	1.31321E-01	9.00872E-03
1.77379E+00	130.0	1.13806E-01	7.88684E-03

$E_{lab}(MeV)$	θ_{lab}	$Yield$	$dYield$
1.76863E+00	130.0	9.36748E-02	7.06933E-03
1.76308E+00	130.0	9.40172E-02	4.54609E-03
1.75754E+00	130.0	9.23117E-02	4.61955E-03
1.75299E+00	130.0	8.04727E-02	5.00331E-03
1.74766E+00	130.0	7.48320E-02	4.76505E-03
1.74234E+00	130.0	7.11955E-02	5.13436E-03
1.73664E+00	130.0	6.23680E-02	4.28420E-03
1.73212E+00	130.0	5.42898E-02	3.77794E-03
1.72721E+00	130.0	5.47245E-02	2.75360E-03
1.72212E+00	130.0	6.53347E-02	3.42697E-03
1.71703E+00	130.0	7.61542E-02	4.52559E-03
1.71195E+00	130.0	7.21727E-02	4.97146E-03
1.70688E+00	130.0	7.39765E-02	5.49816E-03
1.70201E+00	130.0	7.99955E-02	5.96144E-03
1.69695E+00	130.0	5.81347E-02	4.99274E-03
1.69171E+00	130.0	5.54385E-02	4.98017E-03
1.68706E+00	130.0	5.22224E-02	6.16192E-03
1.67680E+00	130.0	5.81283E-02	5.74991E-03
1.66947E+00	130.0	5.55032E-02	8.07915E-03
1.66504E+00	130.0	6.72406E-02	6.70025E-03
1.66023E+00	130.0	7.67815E-02	7.18439E-03

TABLE A.6

Continued

$E_{lab}(MeV)$	θ_{lab}	$Yield$	$dYield$
1.65543E+00	130.0	8.25675E-02	6.98839E-03
1.65121E+00	130.0	6.55043E-02	6.06486E-03
1.64584E+00	130.0	8.15855E-02	5.73037E-03
1.64049E+00	130.0	1.11200E-01	6.80556E-03
1.63495E+00	130.0	9.49980E-02	4.54262E-03
1.63495E+00	130.0	6.17167E-02	4.23821E-03
1.62923E+00	130.0	5.18558E-02	4.33978E-03
1.98058E+00	90.0	9.80598E-01	7.01844E-02
1.97596E+00	90.0	5.68774E-01	4.80511E-02
1.97135E+00	90.0	6.12815E-01	4.82968E-02
1.96570E+00	90.0	8.35055E-01	5.69777E-02
1.96089E+00	90.0	1.04530E+00	7.01573E-02
1.95567E+00	90.0	1.34092E+00	8.82051E-02
1.95108E+00	90.0	1.17042E+00	7.35501E-02
1.93611E+00	90.0	5.39806E-01	4.53084E-02
1.93113E+00	90.0	4.72724E-01	3.34287E-02
1.92574E+00	90.0	4.68268E-01	4.13149E-02
1.92574E+00	90.0	4.73643E-01	4.90880E-02
1.92078E+00	90.0	5.08110E-01	4.30148E-02
1.91582E+00	90.0	7.21786E-01	5.46719E-02
1.91086E+00	90.0	8.68219E-01	6.64343E-02

TABLE A.6

Continued

$E_{lab}(MeV)$	θ_{lab}	$Yield$	$dYield$
1.90571E+00	90.0	1.41675E+00	9.03766E-02
1.90118E+00	90.0	1.93961E+00	1.08182E-01
1.89584E+00	90.0	3.31723E+00	1.97856E-01
1.89112E+00	90.0	5.47220E+00	2.66779E-01
1.88620E+00	90.0	7.36519E+00	4.07171E-01
1.88026E+00	90.0	9.92817E+00	2.23656E-01
1.87597E+00	90.0	1.03800E+01	2.64339E-01
1.87086E+00	90.0	8.18328E+00	3.93404E-01
1.86597E+00	90.0	5.64491E+00	2.56000E-01
1.87127E+00	90.0	8.74788E+00	3.10877E-01
1.86637E+00	90.0	6.77786E+00	3.20944E-01
1.86108E+00	90.0	3.97888E+00	1.78015E-01
1.85579E+00	90.0	2.32250E+00	9.35858E-02
1.85092E+00	90.0	1.45219E+00	6.32952E-02
1.84605E+00	90.0	1.10135E+00	4.77355E-02
1.84078E+00	90.0	7.26461E-01	3.08054E-02
1.83471E+00	90.0	5.54281E-01	2.25512E-02
1.82906E+00	90.0	3.93330E-01	1.54210E-02
1.82402E+00	90.0	3.31855E-01	1.17785E-02
1.81878E+00	90.0	4.18328E-01	1.69236E-02
1.81376E+00	90.0	3.09553E-01	1.34584E-02

TABLE A.6

Continued

$E_{lab}(MeV)$	θ_{lab}	$Yield$	$dYield$
1.80834E+00	90.0	2.57135E-01	1.38019E-02
1.80413E+00	90.0	1.90448E-01	9.60988E-03
1.79872E+00	90.0	1.80725E-01	1.02151E-02
1.79352E+00	90.0	1.31652E-01	8.50632E-03
1.78833E+00	90.0	1.24722E-01	8.61907E-03
1.78374E+00	90.0	1.25488E-01	7.96916E-03
1.77379E+00	90.0	9.97934E-02	6.66813E-03
1.76863E+00	90.0	7.86776E-02	5.84440E-03
1.76308E+00	90.0	6.74446E-02	3.46520E-03
1.75754E+00	90.0	5.75674E-02	3.27764E-03
1.75299E+00	90.0	6.27283E-02	3.98104E-03
1.74766E+00	90.0	5.12312E-02	3.54828E-03
1.74234E+00	90.0	4.82025E-02	3.80226E-03
1.73664E+00	90.0	4.79062E-02	3.38442E-03
1.73212E+00	90.0	4.16336E-02	2.98230E-03
1.72721E+00	90.0	3.44370E-02	1.96614E-03
1.72212E+00	90.0	3.01649E-02	2.09216E-03
1.71703E+00	90.0	3.25860E-02	2.65736E-03
1.71195E+00	90.0	2.89495E-02	2.82575E-03
1.70688E+00	90.0	2.79803E-02	3.03253E-03
1.70201E+00	90.0	2.40568E-02	2.92908E-03

TABLE A.6

Continued

$E_{lab}(MeV)$	θ_{lab}	$Yield$	$dYield$
1.69695E+00	90.0	1.91971E-02	2.57460E-03
1.69171E+00	90.0	2.32755E-02	2.89945E-03
1.68706E+00	90.0	2.32888E-02	3.69873E-03
1.67680E+00	90.0	2.86623E-02	3.63031E-03
1.66947E+00	90.0	2.25906E-02	4.63090E-03
1.66504E+00	90.0	3.87977E-02	4.57734E-03
1.66023E+00	90.0	5.12933E-02	5.28716E-03
1.65543E+00	90.0	4.41926E-02	4.59454E-03
1.65121E+00	90.0	4.43745E-02	4.49696E-03
1.64584E+00	90.0	6.48388E-02	4.60845E-03
1.64049E+00	90.0	5.85195E-02	4.42667E-03
1.63495E+00	90.0	5.38548E-02	3.06948E-03
1.63495E+00	90.0	3.54686E-02	2.89574E-03
1.62923E+00	90.0	3.95989E-02	3.42179E-03
1.98058E+00	30.0	6.86310E+00	4.36163E-01
1.97596E+00	30.0	4.48950E+00	3.22520E-01
1.97135E+00	30.0	4.45927E+00	3.08604E-01
1.96570E+00	30.0	5.53665E+00	3.45372E-01
1.96089E+00	30.0	6.18485E+00	3.91510E-01
1.95567E+00	30.0	6.25280E+00	4.10434E-01
1.95108E+00	30.0	4.35876E+00	2.89758E-01

141

TABLE A.6

Continued

$E_{lab}(MeV)$	θ_{lab}	$Yield$	$dYield$
1.93611E+00	30.0	1.14008E+00	1.28479E-01
1.93113E+00	30.0	8.81610E-01	8.97910E-02
1.92574E+00	30.0	1.30551E+00	1.39739E-01
1.92574E+00	30.0	1.46468E+00	1.76632E-01
1.92078E+00	30.0	1.81549E+00	1.69131E-01
1.91582E+00	30.0	2.65891E+00	2.16984E-01
1.91086E+00	30.0	3.50766E+00	2.79701E-01
1.90571E+00	30.0	5.20660E+00	3.53033E-01
1.90118E+00	30.0	6.35085E+00	3.84441E-01
1.89584E+00	30.0	8.89960E+00	5.91980E-01
1.89112E+00	30.0	1.24703E+01	6.81290E-01
1.88620E+00	30.0	1.41998E+01	8.76200E-01
1.88026E+00	30.0	1.53808E+01	3.92107E-01
1.87597E+00	30.0	1.68396E+01	4.83215E-01
1.87086E+00	30.0	1.29089E+01	7.14170E-01
1.86597E+00	30.0	1.02994E+01	5.36925E-01
1.87127E+00	30.0	1.37149E+01	5.54650E-01
1.86637E+00	30.0	1.11835E+01	6.12620E-01
1.86108E+00	30.0	8.12255E+00	4.22749E-01
1.85579E+00	30.0	5.39375E+00	2.58640E-01
1.85092E+00	30.0	3.76164E+00	1.94438E-01

142

TABLE A.6

Continued

$E_{lab}(MeV)$	θ_{lab}	$Yield$	$dYield$
1.84605E+00	30.0	2.46480E+00	1.37669E-01
1.84078E+00	30.0	1.85123E+00	9.80930E-02
1.83471E+00	30.0	1.37959E+00	7.24545E-02
1.82906E+00	30.0	8.92925E-01	4.76424E-02
1.82402E+00	30.0	6.55215E-01	3.39809E-02
1.81878E+00	30.0	7.27125E-01	4.56963E-02
1.81376E+00	30.0	5.70790E-01	3.78948E-02
1.80834E+00	30.0	4.36787E-01	3.74195E-02
1.80413E+00	30.0	3.51867E-01	2.74390E-02
1.79872E+00	30.0	2.91275E-01	2.71988E-02
1.79352E+00	30.0	2.71213E-01	2.58540E-02
1.78833E+00	30.0	2.22150E-01	2.43510E-02
1.78374E+00	30.0	1.84821E-01	2.04557E-02
1.77379E+00	30.0	1.76572E-01	1.88601E-02
1.76863E+00	30.0	1.32539E-01	1.61655E-02
1.76308E+00	30.0	1.01754E-01	9.07245E-03
1.75754E+00	30.0	1.05513E-01	9.48275E-03
1.75299E+00	30.0	9.11915E-02	1.02387E-02
1.74766E+00	30.0	7.57955E-02	9.22340E-03
1.74234E+00	30.0	6.67485E-02	9.56460E-03
1.73664E+00	30.0	6.74865E-02	8.59440E-03

143

TABLE A.6

Continued

$E_{lab}(MeV)$	θ_{lab}	$Yield$	$dYield$
1.73212E+00	30.0	7.70025E-02	8.69100E-03
1.72721E+00	30.0	5.85200E-02	5.49470E-03
1.72212E+00	30.0	9.19040E-02	7.84960E-03
1.71703E+00	30.0	1.46123E-01	1.21150E-02
1.71195E+00	30.0	1.39310E-01	1.33509E-02
1.70688E+00	30.0	1.65973E-01	1.59278E-02
1.70201E+00	30.0	1.67363E-01	1.66715E-02
1.69695E+00	30.0	1.14486E-01	1.35550E-02
1.69171E+00	30.0	5.31550E-02	9.41660E-03
1.68706E+00	30.0	2.70106E-02	8.55105E-03
1.67680E+00	30.0	7.59975E-02	1.27048E-02
1.66947E+00	30.0	6.11550E-02	1.63849E-02
1.66504E+00	30.0	6.16660E-02	1.23672E-02
1.66023E+00	30.0	8.92795E-02	1.49356E-02
1.65543E+00	30.0	2.64062E-01	2.42523E-02
1.65121E+00	30.0	1.97676E-01	2.04433E-02
1.64584E+00	30.0	3.73693E-01	2.39102E-02
1.64049E+00	30.0	4.12891E-01	2.54923E-02
1.63495E+00	30.0	4.24196E-01	1.87300E-02
1.63495E+00	30.0	9.48965E-02	1.01930E-02
1.62923E+00	30.0	9.67205E-02	1.15029E-02

144

TABLE A.6

Continued

$E_{lab}(MeV)$	θ_{lab}	$Yield$	$dYield$
1.67854E+00	120.0	1.72178E-02	2.57873E-03
1.67313E+00	120.0	2.06572E-02	2.82872E-03
1.66947E+00	120.0	3.24446E-02	3.58508E-03
1.66407E+00	120.0	1.05115E-01	6.58268E-03
1.65869E+00	120.0	1.04430E-01	6.92358E-03
1.65389E+00	120.0	9.84880E-02	6.37833E-03
1.64891E+00	120.0	6.40030E-02	5.18286E-03
1.64335E+00	120.0	2.10737E-02	2.18239E-03
1.63877E+00	120.0	1.72145E-02	1.88502E-03
1.63361E+00	120.0	1.53174E-02	1.77413E-03
1.62866E+00	120.0	3.77315E-02	3.14605E-03
1.62371E+00	120.0	3.72014E-02	3.21348E-03
1.61840E+00	120.0	3.55705E-02	2.71506E-03
1.61346E+00	120.0	4.79761E-02	3.82288E-03
1.60854E+00	120.0	4.51335E-02	3.45807E-03
1.60381E+00	120.0	5.88995E-02	4.08000E-03
1.59872E+00	120.0	6.95361E-02	4.66170E-03
1.59400E+00	120.0	1.05851E-01	6.33936E-03
1.58911E+00	120.0	1.13311E-01	7.03978E-03
1.58385E+00	120.0	1.31080E-01	7.52811E-03
1.57897E+00	120.0	1.49888E-01	6.67150E-03

$E_{lab}(MeV)$	θ_{lab}	$Yield$	$dYield$
1.57373E+00	120.0	1.32771E-01	6.54321E-03
1.56905E+00	120.0	1.23078E-01	6.23435E-03
1.56401E+00	120.0	1.11258E-01	5.93967E-03
1.55879E+00	120.0	9.73275E-02	5.89065E-03
1.55414E+00	120.0	9.26298E-02	5.76347E-03
1.54893E+00	120.0	9.83590E-02	5.86210E-03
1.54392E+00	120.0	1.11109E-01	6.50486E-03
1.53892E+00	120.0	1.05406E-01	6.34989E-03
1.53393E+00	120.0	1.19716E-01	6.88610E-03
1.52913E+00	120.0	1.53434E-01	7.88548E-03
1.52378E+00	120.0	2.03631E-01	9.11207E-03
1.51881E+00	120.0	2.41203E-01	8.92833E-03
1.51881E+00	120.0	2.66560E-01	1.18631E-02
1.51349E+00	120.0	3.04165E-01	1.29775E-02
1.50890E+00	120.0	3.35582E-01	1.42468E-02
1.50359E+00	120.0	3.20641E-01	1.22876E-02
1.49829E+00	120.0	2.97124E-01	1.18536E-02
1.49373E+00	120.0	2.16268E-01	1.44101E-02
1.48826E+00	120.0	1.20429E-01	9.49479E-03
1.48335E+00	120.0	4.94077E-02	4.26193E-03
1.47863E+00	120.0	3.20869E-02	3.04304E-03

TABLE A.6

Continued

$E_{lab}(MeV)$	θ_{lab}	$Yield$	$dYield$
1.47302E+00	120.0	2.97974E-02	3.00233E-03
1.46795E+00	120.0	4.59752E-02	4.34572E-03
1.46271E+00	120.0	6.08499E-02	5.04538E-03
1.45875E+00	120.0	6.72350E-02	5.26396E-03
1.45370E+00	120.0	5.95977E-02	4.90665E-03
1.44831E+00	120.0	5.15481E-02	4.61072E-03
1.44311E+00	120.0	4.35451E-02	3.46639E-03
1.43792E+00	120.0	2.81020E-02	2.64925E-03
1.43256E+00	120.0	2.14713E-02	1.94037E-03
1.42738E+00	120.0	2.31021E-02	2.13285E-03
1.42133E+00	120.0	1.74536E-02	2.58086E-03
1.41706E+00	120.0	2.65581E-02	3.12216E-03
1.41174E+00	120.0	3.73288E-02	3.70046E-03
1.40696E+00	120.0	5.72372E-02	4.60840E-03
1.40201E+00	120.0	8.17737E-02	5.50781E-03
1.39707E+00	120.0	1.10760E-01	6.51744E-03
1.39196E+00	120.0	1.05013E-01	6.18298E-03
1.38703E+00	120.0	7.24858E-02	5.15120E-03
1.38194E+00	120.0	4.59838E-02	4.13852E-03
1.37651E+00	120.0	5.31142E-02	3.60000E-03
1.37126E+00	120.0	8.89636E-02	5.74814E-03

147

TABLE A.6

Continued

$E_{lab}(MeV)$	θ_{lab}	$Yield$	$dYield$
1.36568E+00	120.0	9.79888E-02	6.92862E-03
1.36010E+00	120.0	1.04756E-01	7.71839E-03
1.35454E+00	120.0	8.81031E-02	6.32849E-03
1.34934E+00	120.0	1.06084E-01	5.91181E-03
1.34380E+00	120.0	1.47657E-01	5.51696E-03
1.33827E+00	120.0	2.43131E-01	9.51962E-03
1.33361E+00	120.0	3.55736E-01	1.22557E-02
1.32845E+00	120.0	5.48540E-01	1.73441E-02
1.32347E+00	120.0	6.08214E-01	2.71427E-02
1.31901E+00	120.0	4.37797E-01	1.78351E-02
1.31370E+00	120.0	1.59463E-01	9.96693E-03
1.30909E+00	120.0	4.36487E-02	3.42549E-03
1.30602E+00	120.0	1.86615E-02	5.00287E-03
1.30074E+00	120.0	1.06969E-02	9.77953E-04
1.29598E+00	120.0	9.46335E-03	1.09354E-03
1.29038E+00	120.0	7.33727E-03	9.55852E-04
1.28463E+00	120.0	1.04063E-02	1.19459E-03
1.27973E+00	120.0	1.07614E-02	1.20410E-03
1.27467E+00	120.0	9.54091E-03	1.16641E-03
1.27012E+00	120.0	5.27293E-03	8.34044E-04
1.26391E+00	120.0	8.24542E-03	9.59126E-04

148

TABLE A.6

Continued

$E_{lab}(MeV)$	θ_{lab}	$Yield$	$dYield$
1.25721E+00	120.0	6.85160E-03	1.03344E-03
1.25103E+00	120.0	3.08800E-03	6.59897E-04
1.24569E+00	120.0	2.42866E-03	4.76479E-04
1.24070E+00	120.0	1.14474E-03	2.09048E-04
1.23523E+00	120.0	6.02523E-04	2.13058E-04
1.22943E+00	120.0	9.15266E-04	1.83084E-04
1.22398E+00	120.0	1.51717E-03	3.79382E-04
1.67854E+00	100.0	1.55962E-02	2.26239E-03
1.67313E+00	100.0	1.49436E-02	2.21510E-03
1.66947E+00	100.0	2.22419E-02	2.73196E-03
1.66407E+00	100.0	7.44520E-02	5.09894E-03
1.65869E+00	100.0	8.10158E-02	5.61639E-03
1.65389E+00	100.0	7.08605E-02	4.98043E-03
1.64891E+00	100.0	4.30663E-02	3.91423E-03
1.64335E+00	100.0	1.80905E-02	1.86365E-03
1.63877E+00	100.0	1.46226E-02	1.60120E-03
1.63361E+00	100.0	1.52670E-02	1.63333E-03
1.62866E+00	100.0	2.94003E-02	2.55874E-03
1.62371E+00	100.0	2.97316E-02	2.64732E-03
1.61840E+00	100.0	3.33636E-02	2.42464E-03
1.61346E+00	100.0	4.30676E-02	3.33946E-03

149

$E_{lab}(MeV)$	θ_{lab}	$Yield$	$dYield$
1.60854E+00	100.0	4.39203E-02	3.14655E-03
1.60381E+00	100.0	5.50252E-02	3.63725E-03
1.59872E+00	100.0	6.53587E-02	4.16945E-03
1.59400E+00	100.0	9.49932E-02	5.53922E-03
1.58911E+00	100.0	9.41113E-02	5.91228E-03
1.58385E+00	100.0	9.63958E-02	5.93983E-03
1.57897E+00	100.0	1.14616E-01	5.37067E-03
1.57373E+00	100.0	7.92254E-02	4.64105E-03
1.56905E+00	100.0	6.39673E-02	4.12472E-03
1.56401E+00	100.0	5.68942E-02	3.89808E-03
1.55879E+00	100.0	4.21033E-02	3.55297E-03
1.55414E+00	100.0	3.66829E-02	3.32453E-03
1.54893E+00	100.0	3.42558E-02	3.16831E-03
1.54392E+00	100.0	4.54870E-02	3.81318E-03
1.53892E+00	100.0	5.30648E-02	4.13465E-03
1.53393E+00	100.0	5.03971E-02	4.09014E-03
1.52913E+00	100.0	8.18594E-02	5.27679E-03
1.52378E+00	100.0	1.08120E-01	6.07225E-03
1.51881E+00	100.0	1.34765E-01	6.09840E-03
1.51881E+00	100.0	1.40421E-01	7.86471E-03
1.51349E+00	100.0	1.87845E-01	9.33362E-03

TABLE A.6

Continued

$E_{lab}(MeV)$	θ_{lab}	$Yield$	$dYield$
1.50890E+00	100.0	2.20384E-01	1.05679E-02
1.50359E+00	100.0	2.47280E-01	9.92536E-03
1.49829E+00	100.0	2.65356E-01	1.03413E-02
1.49373E+00	100.0	1.99634E-01	1.27877E-02
1.48826E+00	100.0	9.55894E-02	7.79444E-03
1.48335E+00	100.0	3.61496E-02	3.35917E-03
1.47863E+00	100.0	2.77775E-02	2.61131E-03
1.47302E+00	100.0	2.40641E-02	2.48799E-03
1.46795E+00	100.0	3.08009E-02	3.27722E-03
1.46271E+00	100.0	3.87310E-02	3.70749E-03
1.45875E+00	100.0	4.05554E-02	3.76445E-03
1.45370E+00	100.0	3.70885E-02	3.56533E-03
1.44831E+00	100.0	3.34120E-02	3.42055E-03
1.44311E+00	100.0	2.58627E-02	2.46125E-03
1.43792E+00	100.0	2.39093E-02	2.25399E-03
1.43256E+00	100.0	1.72290E-02	1.60307E-03
1.42738E+00	100.0	1.76586E-02	1.71959E-03
1.42133E+00	100.0	9.04017E-03	1.71145E-03
1.41706E+00	100.0	8.97801E-03	1.67011E-03
1.41174E+00	100.0	1.97385E-02	2.47664E-03
1.40696E+00	100.0	3.38192E-02	3.25919E-03

151

TABLE A.6

Continued

$E_{lab}(MeV)$	θ_{lab}	$Yield$	$dYield$
1.40201E+00	100.0	4.71152E-02	3.84149E-03
1.39707E+00	100.0	5.72571E-02	4.29681E-03
1.39196E+00	100.0	6.07911E-02	4.32009E-03
1.38703E+00	100.0	4.58158E-02	3.76873E-03
1.38194E+00	100.0	3.53847E-02	3.34745E-03
1.37651E+00	100.0	4.29637E-02	2.98619E-03
1.37126E+00	100.0	6.12063E-02	4.38966E-03
1.36568E+00	100.0	6.55172E-02	5.21378E-03
1.36010E+00	100.0	7.12562E-02	5.85872E-03
1.35454E+00	100.0	6.81946E-02	5.13260E-03
1.34934E+00	100.0	7.74632E-02	4.65348E-03
1.34380E+00	100.0	1.26919E-01	4.72068E-03
1.33827E+00	100.0	2.01963E-01	8.00073E-03
1.33361E+00	100.0	2.76002E-01	9.92378E-03
1.32845E+00	100.0	4.39874E-01	1.42850E-02
1.32347E+00	100.0	4.77337E-01	2.20832E-02
1.31901E+00	100.0	3.80717E-01	1.53646E-02
1.31370E+00	100.0	1.33781E-01	8.42297E-03
1.30909E+00	100.0	3.83145E-02	2.96250E-03
1.30602E+00	100.0	3.86064E-02	6.67039E-03
1.30074E+00	100.0	1.23016E-02	9.68464E-04

152

$E_{lab}(MeV)$	θ_{lab}	$Yield$	$dYield$
1.29598E+00	100.0	1.10716E-02	1.09202E-03
1.29038E+00	100.0	7.73428E-03	9.05957E-04
1.28463E+00	100.0	9.33281E-03	1.04428E-03
1.27973E+00	100.0	8.13732E-03	9.66394E-04
1.27467E+00	100.0	6.06689E-03	8.58429E-04
1.27012E+00	100.0	4.38084E-03	7.01759E-04
1.26391E+00	100.0	3.60821E-03	5.85522E-04
1.25721E+00	100.0	2.12332E-03	5.30928E-04
1.25103E+00	100.0	2.63193E-03	5.62435E-04
1.24569E+00	100.0	1.91084E-03	3.90184E-04
1.24070E+00	100.0	1.13840E-03	1.92476E-04
1.23523E+00	100.0	1.92601E-03	3.51848E-04
1.22943E+00	100.0	9.36282E-04	1.70975E-04
1.22398E+00	100.0	1.21257E-03	3.13154E-04
1.67854E+00	40.0	4.77533E-03	1.19583E-03
1.67313E+00	40.0	6.56559E-03	1.40337E-03
1.66947E+00	40.0	1.12845E-02	1.86070E-03
1.66407E+00	40.0	3.45208E-02	3.31742E-03
1.65869E+00	40.0	3.31661E-02	3.43150E-03
1.65389E+00	40.0	2.98606E-02	3.08884E-03
1.64891E+00	40.0	1.29778E-02	2.05460E-03

TABLE A.6

Continued

$E_{lab}(MeV)$	θ_{lab}	$Yield$	$dYield$
1.64335E+00	40.0	9.10218E-03	1.26508E-03
1.63877E+00	40.0	6.40120E-03	1.01385E-03
1.63361E+00	40.0	8.13472E-03	1.14147E-03
1.62866E+00	40.0	9.55307E-03	1.39528E-03
1.62371E+00	40.0	1.57155E-02	1.84299E-03
1.61840E+00	40.0	1.23700E-02	1.41217E-03
1.61346E+00	40.0	2.59368E-02	2.48114E-03
1.60854E+00	40.0	2.70708E-02	2.36498E-03
1.60381E+00	40.0	3.18565E-02	2.64780E-03
1.59872E+00	40.0	4.25750E-02	3.21978E-03
1.59400E+00	40.0	6.91137E-02	4.52137E-03
1.58911E+00	40.0	6.16235E-02	4.57256E-03
1.58385E+00	40.0	7.45890E-02	5.00276E-03
1.57897E+00	40.0	8.01968E-02	4.29726E-03
1.57373E+00	40.0	7.21946E-02	4.25030E-03
1.56905E+00	40.0	6.75801E-02	4.07221E-03
1.56401E+00	40.0	5.91758E-02	3.81809E-03
1.55879E+00	40.0	4.34125E-02	3.46437E-03
1.55414E+00	40.0	4.66919E-02	3.60644E-03
1.54893E+00	40.0	5.80223E-02	3.97277E-03
1.54392E+00	40.0	6.86702E-02	4.51363E-03

154

TABLE A.6

Continued

$E_{lab}(MeV)$	θ_{lab}	$Yield$	$dYield$
1.53892E+00	40.0	9.22103E-02	5.26298E-03
1.53393E+00	40.0	1.14576E-01	5.98076E-03
1.52913E+00	40.0	1.81828E-01	7.66402E-03
1.52378E+00	40.0	2.42375E-01	8.89789E-03
1.51881E+00	40.0	2.95547E-01	8.87644E-03
1.51881E+00	40.0	3.30830E-01	1.18659E-02
1.51349E+00	40.0	4.48469E-01	1.42817E-02
1.50890E+00	40.0	5.00817E-01	1.58511E-02
1.50359E+00	40.0	5.23010E-01	1.42968E-02
1.49829E+00	40.0	5.07097E-01	1.40605E-02
1.49373E+00	40.0	3.18914E-01	1.57495E-02
1.48826E+00	40.0	1.34534E-01	8.93483E-03
1.48335E+00	40.0	4.64546E-02	3.66458E-03
1.47863E+00	40.0	3.93367E-02	2.99058E-03
1.47302E+00	40.0	5.21989E-02	3.53109E-03
1.46795E+00	40.0	6.32292E-02	4.53118E-03
1.46271E+00	40.0	8.80576E-02	5.40119E-03
1.45875E+00	40.0	1.05252E-01	5.86825E-03
1.45370E+00	40.0	1.03018E-01	5.75010E-03
1.44831E+00	40.0	8.03251E-02	5.12062E-03
1.44311E+00	40.0	6.43214E-02	3.74616E-03

155

TABLE A.6

Continued

$E_{lab}(MeV)$	θ_{lab}	$Yield$	$dYield$
1.43792E+00	40.0	5.35334E-02	3.25075E-03
1.43256E+00	40.0	3.30568E-02	2.13877E-03
1.42738E+00	40.0	3.29276E-02	2.26263E-03
1.42133E+00	40.0	2.86319E-02	2.93989E-03
1.41706E+00	40.0	3.31776E-02	3.10211E-03
1.41174E+00	40.0	4.47399E-02	3.60364E-03
1.40696E+00	40.0	6.73777E-02	4.45326E-03
1.40201E+00	40.0	8.22493E-02	4.91575E-03
1.39707E+00	40.0	1.09648E-01	5.77443E-03
1.39196E+00	40.0	1.08221E-01	5.59236E-03
1.38703E+00	40.0	5.47837E-02	3.97111E-03
1.38194E+00	40.0	2.54801E-02	2.72810E-03
1.37651E+00	40.0	4.78677E-02	3.03558E-03
1.37126E+00	40.0	5.68959E-02	4.07043E-03
1.36568E+00	40.0	7.67922E-02	5.44281E-03
1.36010E+00	40.0	7.11626E-02	5.63610E-03
1.35454E+00	40.0	6.69563E-02	4.89501E-03
1.34934E+00	40.0	6.71263E-02	4.16445E-03
1.34380E+00	40.0	1.03982E-01	4.10249E-03
1.33827E+00	40.0	1.85571E-01	7.37713E-03
1.33361E+00	40.0	2.85027E-01	9.74759E-03

156

TABLE A.6

Continued

$E_{lab}(MeV)$	θ_{lab}	$Yield$	$dYield$
1.32845E+00	40.0	4.59347E-01	1.41440E-02
1.32347E+00	40.0	5.21565E-01	2.24425E-02
1.31901E+00	40.0	4.04453E-01	1.53487E-02
1.31370E+00	40.0	1.60337E-01	8.92305E-03
1.30909E+00	40.0	5.29261E-02	3.35970E-03
1.30602E+00	40.0	2.73516E-02	5.39475E-03
1.30074E+00	40.0	1.56907E-02	1.05366E-03
1.29598E+00	40.0	1.80301E-02	1.34255E-03
1.29038E+00	40.0	1.39443E-02	1.17201E-03
1.28463E+00	40.0	1.52482E-02	1.28594E-03
1.27973E+00	40.0	1.50885E-02	1.26796E-03
1.27467E+00	40.0	1.51889E-02	1.30906E-03
1.27012E+00	40.0	9.47946E-03	9.94586E-04
1.26391E+00	40.0	8.27865E-03	8.54575E-04
1.25721E+00	40.0	7.14049E-03	9.38212E-04
1.25103E+00	40.0	2.77504E-03	5.56477E-04
1.24569E+00	40.0	2.51209E-03	4.31032E-04
1.24070E+00	40.0	1.29808E-03	1.98019E-04
1.23523E+00	40.0	1.54946E-03	3.04031E-04
1.22943E+00	40.0	8.40283E-04	1.56067E-04
1.22398E+00	40.0	2.10176E-03	3.97359E-04

157

TABLE A.6

Continued

$E_{lab}(MeV)$	θ_{lab}	$Yield$	$dYield$
1.36743E+00	105.0	1.32723E-01	1.24290E-02
1.35603E+00	105.0	1.14242E-01	1.41674E-02
1.34572E+00	105.0	2.08946E-01	1.91522E-02
1.33509E+00	105.0	3.21023E-01	2.37304E-02
1.32452E+00	105.0	4.93275E-01	2.94845E-02
1.31466E+00	105.0	3.26230E-01	2.39837E-02
1.30991E+00	105.0	1.21039E-01	1.45702E-02
1.30500E+00	105.0	3.55256E-02	3.83256E-03
1.29471E+00	105.0	9.88362E-03	9.21562E-04
1.28480E+00	105.0	7.23426E-03	6.89510E-04
1.27475E+00	105.0	6.54984E-03	6.39247E-04
1.26458E+00	105.0	4.24421E-03	4.20226E-04
1.25396E+00	105.0	3.50984E-03	3.40986E-04
1.24486E+00	105.0	3.00885E-03	2.95047E-04
1.23481E+00	105.0	2.45533E-03	2.43121E-04
1.22497E+00	105.0	2.40025E-03	2.30972E-04
1.21353E+00	105.0	1.75063E-03	1.70834E-04
1.20539E+00	105.0	2.53010E-03	2.48084E-04
1.19567E+00	105.0	1.50627E-03	1.43637E-04
1.18598E+00	105.0	1.41861E-03	1.42560E-04
1.17633E+00	105.0	1.17834E-03	1.28559E-04

158

TABLE A.6

Continued

$E_{lab}(MeV)$	θ_{lab}	$Yield$	$dYield$
1.16672E+00	105.0	9.12976E-04	1.30465E-04
1.15715E+00	105.0	6.93808E-04	1.04595E-04
1.14762E+00	105.0	3.55667E-04	6.60674E-05
1.13813E+00	105.0	2.56733E-04	5.60195E-05
1.12868E+00	105.0	3.75928E-04	8.01422E-05
1.11927E+00	105.0	5.06292E-04	9.09230E-05
1.10989E+00	105.0	5.46891E-04	9.51995E-05
1.10056E+00	105.0	6.46390E-04	1.02214E-04
1.09127E+00	105.0	8.39018E-04	1.32679E-04
1.08201E+00	105.0	9.65179E-04	1.17916E-04
1.07280E+00	105.0	7.25414E-04	9.96180E-05
1.06362E+00	105.0	7.69167E-04	1.13386E-04
1.05449E+00	105.0	4.52784E-04	6.90522E-05
1.04539E+00	105.0	3.53019E-04	5.97095E-05
1.03633E+00	105.0	2.47113E-04	4.00752E-05
1.02717E+00	105.0	2.19687E-04	3.94517E-05
1.02717E+00	105.0	2.19687E-04	3.94517E-05
1.35948E+00	120.0	1.06686E-01	7.84458E-03
1.35431E+00	120.0	9.88828E-02	7.58332E-03
1.34915E+00	120.0	1.06341E-01	7.88308E-03
1.34400E+00	120.0	1.27918E-01	8.66727E-03

TABLE A.6

Continued

$E_{lab}(MeV)$	θ_{lab}	$Yield$	$dYield$
1.33886E+00	120.0	1.93064E-01	1.07227E-02
1.33373E+00	120.0	2.77302E-01	1.27653E-02
1.32860E+00	120.0	4.46913E-01	1.64535E-02
1.32349E+00	120.0	6.08258E-01	1.91675E-02
1.31840E+00	120.0	5.23868E-01	1.78405E-02
1.31330E+00	120.0	3.26908E-01	1.15137E-02
1.30822E+00	120.0	8.86718E-02	6.38250E-03
1.30314E+00	120.0	2.15593E-02	2.15593E-03
1.29809E+00	120.0	1.24196E-02	1.06876E-03
1.29303E+00	120.0	9.01301E-03	7.51123E-04
1.28799E+00	120.0	7.42449E-03	6.51119E-04
1.28295E+00	120.0	7.46287E-03	6.87000E-04
1.27793E+00	120.0	6.15302E-03	5.92032E-04
1.27176E+00	120.0	7.27724E-03	6.06378E-04
1.26792E+00	120.0	5.54037E-03	4.61678E-04
1.26259E+00	120.0	4.89796E-03	4.27958E-04
1.25761E+00	120.0	5.22483E-03	4.23831E-04
1.25263E+00	120.0	4.84916E-03	3.86975E-04
1.24800E+00	120.0	3.67892E-03	2.88165E-04
1.24322E+00	120.0	2.50372E-03	2.55515E-04
1.23810E+00	120.0	2.45053E-03	2.34770E-04

TABLE A.6

Continued

$E_{lab}(MeV)$	θ_{lab}	$Yield$	$dYield$
1.23301E+00	120.0	1.83522E-03	1.97900E-04
1.22791E+00	120.0	2.01188E-03	2.14507E-04
1.22317E+00	120.0	2.07613E-03	2.33535E-04
1.21793E+00	120.0	1.92694E-03	1.93746E-04
1.21353E+00	120.0	1.91417E-03	1.86746E-04
1.20864E+00	120.0	1.57939E-03	1.51281E-04
1.20377E+00	120.0	1.74843E-03	1.58258E-04
1.19890E+00	120.0	1.67765E-03	1.53171E-04
1.19405E+00	120.0	1.62323E-03	1.60805E-04
1.18921E+00	120.0	1.64329E-03	1.58139E-04
1.18437E+00	120.0	1.59772E-03	1.41799E-04
1.17954E+00	120.0	1.49659E-03	1.48141E-04
1.17472E+00	120.0	1.28579E-03	1.31966E-04
1.16992E+00	120.0	1.09680E-03	1.18236E-04
1.16512E+00	120.0	1.44327E-03	1.40827E-04
1.16033E+00	120.0	1.55297E-03	1.58447E-04
1.15556E+00	120.0	1.09246E-03	1.12081E-04
1.15080E+00	120.0	1.19305E-03	1.18138E-04
1.14604E+00	120.0	4.68906E-04	5.56411E-05
1.14129E+00	120.0	1.92566E-04	2.52867E-05
1.13655E+00	120.0	1.29123E-04	2.28269E-05

TABLE A.6

Continued

$E_{lab}(MeV)$	θ_{lab}	$Yield$	$dYield$
1.13057E+00	120.0	2.26816E-04	3.45941E-05
1.12569E+00	120.0	3.13919E-04	4.35312E-05
1.12083E+00	120.0	3.58253E-04	4.47933E-05
1.11613E+00	120.0	5.43402E-04	6.54181E-05
1.11146E+00	120.0	6.06501E-04	6.53953E-05
1.10678E+00	120.0	7.28193E-04	7.17467E-05
1.10212E+00	120.0	8.06009E-04	7.98082E-05
1.09746E+00	120.0	8.23707E-04	8.19627E-05
1.09234E+00	120.0	1.08545E-03	1.00350E-04
1.08818E+00	120.0	1.15579E-03	1.13329E-04
1.08355E+00	120.0	1.28746E-03	1.18492E-04
1.07893E+00	120.0	1.52163E-03	1.40629E-04
1.07417E+00	120.0	1.81622E-03	1.78125E-04
1.06973E+00	120.0	1.80726E-03	1.75599E-04
1.06499E+00	120.0	1.51494E-03	1.41938E-04
1.06057E+00	120.0	1.35363E-03	1.32800E-04
1.05600E+00	120.0	1.06443E-03	1.13466E-04
1.05145E+00	120.0	6.79214E-04	7.24053E-05
1.04690E+00	120.0	5.40680E-04	6.46184E-05
1.04236E+00	120.0	4.89401E-04	5.93499E-05
1.03784E+00	120.0	3.09750E-04	4.89778E-05

Continued

$E_{lab}(MeV)$	θ_{lab}	$Yield$	$dYield$
1.03257E+00	120.0	3.64715E-04	6.07975E-05
1.02731E+00	120.0	3.00626E-04	5.08223E-05
1.02281E+00	120.0	3.13433E-04	5.15250E-05
1.01386E+00	120.0	2.34498E-04	4.88897E-05
1.00494E+00	120.0	2.07287E-04	4.75528E-05
9.96055E-01	120.0	1.22627E-04	3.16573E-05
9.87222E-01	120.0	8.65941E-05	2.23551E-05
9.78418E-01	120.0	1.13845E-04	2.68303E-05
9.66745E-01	120.0	7.08093E-05	2.23939E-05
9.55142E-01	120.0	6.60148E-05	2.49531E-05
9.43608E-01	120.0	2.72847E-05	1.22014E-05
9.28720E-01	120.0	9.28034E-06	6.56293E-06
1.36282E+00	135.0	1.07857E-01	4.52700E-03
1.35679E+00	135.0	1.24052E-01	4.80640E-03
1.34650E+00	135.0	1.22793E-01	6.82350E-03
1.34225E+00	135.0	1.41667E-01	7.32601E-03
1.33799E+00	135.0	1.95256E-01	8.59160E-03
1.33799E+00	135.0	1.98932E-01	8.67505E-03
1.33364E+00	135.0	2.69424E-01	1.01076E-02
1.32939E+00	135.0	3.42021E-01	1.13867E-02
1.32513E+00	135.0	4.19248E-01	1.25866E-02

163

TABLE A.6

Continued

$E_{lab}(MeV)$	θ_{lab}	$Yield$	$dYield$
1.32098E+00	135.0	4.94031E-01	1.36826E-02
1.31672E+00	135.0	4.34795E-01	1.28289E-02
1.31247E+00	135.0	2.20458E-01	9.12932E-03
1.30822E+00	135.0	4.69240E-02	4.21405E-03
1.30574E+00	135.0	1.96073E-02	2.89135E-03
1.30574E+00	135.0	1.72249E-02	1.69741E-03
1.29645E+00	135.0	7.04253E-03	4.81400E-04
1.29308E+00	135.0	6.48319E-03	4.50656E-04
1.29021E+00	135.0	5.90682E-03	3.72812E-04
1.28804E+00	135.0	5.90214E-03	3.94312E-04
1.28556E+00	135.0	5.73690E-03	3.85943E-04
1.28299E+00	135.0	6.10138E-03	4.27230E-04
1.28052E+00	135.0	6.22656E-03	4.39203E-04
1.27805E+00	135.0	6.67252E-03	4.53999E-04
1.27567E+00	135.0	5.66970E-03	4.33521E-04
1.27547E+00	135.0	5.66967E-03	3.80512E-04
1.27300E+00	135.0	4.72175E-03	3.39906E-04
1.27053E+00	135.0	4.65570E-03	3.06287E-04
1.26806E+00	135.0	4.64225E-03	3.17307E-04
1.26420E+00	135.0	4.71658E-03	4.97221E-04
1.25806E+00	135.0	4.22794E-03	2.71754E-04

164

TABLE A.6

Continued

$E_{lab}(MeV)$	θ_{lab}	$Yield$	$dYield$
1.25312E+00	135.0	3.66509E-03	2.58536E-04
1.24817E+00	135.0	2.68040E-03	1.84930E-04
1.24402E+00	135.0	1.96216E-03	1.87115E-04
1.24323E+00	135.0	1.96834E-03	1.47980E-04
1.24194E+00	135.0	1.87623E-03	1.88542E-04
1.23749E+00	135.0	2.00037E-03	1.79666E-04
1.23422E+00	135.0	1.68877E-03	1.80064E-04
1.22433E+00	135.0	2.03614E-03	2.15798E-04
1.21454E+00	135.0	1.47001E-03	1.65355E-04
1.20455E+00	135.0	1.84053E-03	1.97402E-04
1.19515E+00	135.0	1.45766E-03	1.52770E-04
1.18536E+00	135.0	1.21622E-03	1.36794E-04
1.17646E+00	135.0	1.32282E-03	1.35699E-04
1.17092E+00	135.0	1.37176E-03	1.42260E-04
1.16646E+00	135.0	1.36390E-03	1.35723E-04
1.16073E+00	135.0	1.30148E-03	1.36397E-04
1.15548E+00	135.0	1.68402E-03	1.75568E-04
1.14876E+00	135.0	8.68421E-04	8.95924E-05
1.14411E+00	135.0	4.21011E-04	4.64920E-05
1.14332E+00	135.0	3.26984E-04	3.77622E-05
1.13867E+00	135.0	1.16118E-04	1.59517E-05

TABLE A.6

Continued

$E_{lab}(MeV)$	θ_{lab}	$Yield$	$dYield$
1.13461E+00	135.0	1.02562E-04	3.87522E-05
1.13066E+00	135.0	1.62054E-04	2.77891E-05
1.12601E+00	135.0	2.07226E-04	3.91641E-05
1.11117E+00	135.0	4.14734E-04	5.69677E-05
1.10652E+00	135.0	4.35718E-04	5.72135E-05
1.10187E+00	135.0	6.74712E-04	8.30575E-05
1.09722E+00	135.0	7.13180E-04	8.40406E-05
1.09415E+00	135.0	8.56492E-04	1.11535E-04
1.08950E+00	135.0	8.48947E-04	1.06098E-04
1.08486E+00	135.0	9.43638E-04	1.09009E-04
1.08031E+00	135.0	1.16185E-03	1.28328E-04
1.07566E+00	135.0	1.15344E-03	1.27403E-04
1.07111E+00	135.0	1.35757E-03	1.51719E-04
1.06646E+00	135.0	1.63984E-03	1.61574E-04
1.06191E+00	135.0	1.71065E-03	1.73725E-04
1.05736E+00	135.0	1.89784E-03	1.87041E-04
1.05281E+00	135.0	1.23884E-03	1.30531E-04
1.04826E+00	135.0	7.73685E-04	9.05818E-05
1.04380E+00	135.0	4.81793E-04	6.32696E-05
1.03836E+00	135.0	4.86311E-04	7.01970E-05
1.03470E+00	135.0	2.66625E-04	4.27015E-05

TABLE A.6

Continued

$E_{lab}(MeV)$	θ_{lab}	$Yield$	$dYield$
1.03025E+00	135.0	2.91709E-04	4.73228E-05
1.02550E+00	135.0	2.18699E-04	3.54783E-05
1.02125E+00	135.0	2.21085E-04	3.25940E-05
1.01235E+00	135.0	1.50243E-04	3.20326E-05
1.00344E+00	135.0	1.39304E-04	2.78525E-05
9.94641E-01	135.0	9.10089E-05	1.98610E-05
9.85837E-01	135.0	8.86070E-05	1.88995E-05
9.77033E-01	135.0	4.67340E-05	1.13352E-05
9.68328E-01	135.0	6.16442E-05	1.34546E-05
9.59623E-01	135.0	4.83674E-05	9.48446E-06
9.50819E-01	135.0	3.30068E-05	7.38116E-06
9.30936E-01	135.0	1.96056E-05	6.20139E-06
9.11152E-01	135.0	8.88625E-06	3.97316E-06
8.93445E-01	135.0	1.15538E-05	4.71661E-06
8.71683E-01	135.0	8.83194E-06	3.33927E-06
8.52987E-01	135.0	6.89187E-06	3.97881E-06
8.52987E-01	135.0	1.31882E-05	3.97713E-06
8.33995E-01	135.0	2.02657E-05	5.41603E-06
8.15299E-01	135.0	1.74482E-05	5.26086E-06
7.89283E-01	135.0	2.61758E-05	6.54394E-06
1.35948E+00	150.0	1.69345E-01	1.07137E-02

167

TABLE A.6

Continued

$E_{lab}(MeV)$	θ_{lab}	$Yield$	$dYield$
1.35431E+00	150.0	1.27118E-01	9.31996E-03
1.34915E+00	150.0	1.24251E-01	9.23560E-03
1.34400E+00	150.0	1.19902E-01	9.08888E-03
1.33886E+00	150.0	2.10741E-01	1.21427E-02
1.33373E+00	150.0	2.66506E-01	1.35659E-02
1.32860E+00	150.0	4.36749E-01	1.76239E-02
1.32349E+00	150.0	5.49166E-01	1.97397E-02
1.31840E+00	150.0	4.52522E-01	1.79744E-02
1.31330E+00	150.0	3.07297E-01	1.20982E-02
1.30822E+00	150.0	9.82011E-02	7.27991E-03
1.30314E+00	150.0	2.22727E-02	2.37420E-03
1.29809E+00	150.0	1.04795E-02	1.06402E-03
1.29303E+00	150.0	6.76209E-03	7.04911E-04
1.28799E+00	150.0	7.04179E-03	6.87289E-04
1.28295E+00	150.0	6.83173E-03	7.12136E-04
1.27793E+00	150.0	6.35442E-03	6.52052E-04
1.27176E+00	150.0	5.51850E-03	5.72162E-04
1.26792E+00	150.0	4.15664E-03	4.33229E-04
1.26259E+00	150.0	4.74200E-03	4.56225E-04
1.25761E+00	150.0	4.23746E-03	4.13458E-04
1.25263E+00	150.0	3.62594E-03	3.62594E-04

168

$E_{lab}(MeV)$	θ_{lab}	$Yield$	$dYield$
1.24800E+00	150.0	2.67614E-03	2.66242E-04
1.24322E+00	150.0	2.84769E-03	2.95331E-04
1.23810E+00	150.0	2.63971E-03	2.63971E-04
1.23301E+00	150.0	2.30495E-03	2.40231E-04
1.22791E+00	150.0	2.49627E-03	2.58812E-04
1.22317E+00	150.0	2.71523E-03	2.89479E-04
1.21793E+00	150.0	2.44533E-03	2.36446E-04
1.21353E+00	150.0	2.56919E-03	2.34447E-04
1.20864E+00	150.0	2.17657E-03	1.92453E-04
1.20377E+00	150.0	2.10231E-03	1.88044E-04
1.19890E+00	150.0	2.03603E-03	1.82791E-04
1.19405E+00	150.0	1.94330E-03	1.90633E-04
1.18921E+00	150.0	1.87571E-03	1.83053E-04
1.18437E+00	150.0	2.02461E-03	1.73030E-04
1.17954E+00	150.0	1.79204E-03	1.75782E-04
1.17472E+00	150.0	1.81158E-03	1.69664E-04
1.16992E+00	150.0	1.58839E-03	1.54320E-04
1.16512E+00	150.0	1.64752E-03	1.63110E-04
1.16033E+00	150.0	2.50848E-03	2.18295E-04
1.15556E+00	150.0	2.01362E-03	1.64975E-04
1.15080E+00	150.0	1.42924E-03	1.40189E-04

TABLE A.6

Continued

$E_{lab}(MeV)$	θ_{lab}	$Yield$	$dYield$
1.14604E+00	150.0	6.44120E-04	7.07028E-05
1.14129E+00	150.0	2.02989E-04	2.81450E-05
1.13655E+00	150.0	2.04148E-04	3.11350E-05
1.13057E+00	150.0	1.86187E-04	3.39977E-05
1.12569E+00	150.0	3.98010E-04	5.31819E-05
1.12083E+00	150.0	4.41684E-04	5.39669E-05
1.11613E+00	150.0	4.63746E-04	6.55858E-05
1.11146E+00	150.0	7.72622E-04	8.01172E-05
1.10678E+00	150.0	8.33077E-04	8.33077E-05
1.10212E+00	150.0	1.02464E-03	9.76841E-05
1.09746E+00	150.0	1.27895E-03	1.10894E-04
1.09234E+00	150.0	1.56484E-03	1.30841E-04
1.08818E+00	150.0	1.32382E-03	1.31727E-04
1.08355E+00	150.0	1.81571E-03	1.52902E-04
1.07893E+00	150.0	2.28643E-03	1.87419E-04
1.07417E+00	150.0	2.36895E-03	2.20929E-04
1.06973E+00	150.0	2.49486E-03	2.23978E-04
1.06499E+00	150.0	2.39977E-03	1.94000E-04
1.06057E+00	150.0	1.58296E-03	1.55978E-04
1.05600E+00	150.0	1.21399E-03	1.31667E-04
1.05145E+00	150.0	7.93224E-04	8.50487E-05

TABLE A.6

Continued

$E_{lab}(MeV)$	θ_{lab}	$Yield$	$dYield$
1.04690E+00	150.0	4.38140E-04	6.32399E-05
1.04236E+00	150.0	3.57401E-04	5.51505E-05
1.03784E+00	150.0	4.57845E-04	6.47388E-05
1.03257E+00	150.0	4.07456E-04	6.98808E-05
1.02731E+00	150.0	3.45528E-04	5.92450E-05
1.02281E+00	150.0	3.31031E-04	5.76239E-05
1.01386E+00	150.0	3.38018E-04	6.38736E-05
1.00494E+00	150.0	2.97365E-04	6.20054E-05
9.96055E-01	150.0	2.42174E-04	4.84348E-05
9.87222E-01	150.0	1.30086E-04	2.98481E-05
9.78418E-01	150.0	7.50588E-05	2.37321E-05
9.66745E-01	150.0	5.88556E-05	2.22374E-05
9.55142E-01	150.0	7.84413E-05	2.96533E-05
9.43608E-01	150.0	4.54239E-05	1.71698E-05
9.28720E-01	150.0	3.31499E-05	1.35315E-05
1.36743E+00	75.0	1.11899E-01	9.35747E-03
1.35603E+00	75.0	1.28767E-01	1.23333E-02
1.34572E+00	75.0	1.69963E-01	1.41644E-02
1.33509E+00	75.0	3.29094E-01	1.96986E-02
1.32452E+00	75.0	4.76295E-01	2.37560E-02
1.31466E+00	75.0	3.13045E-01	1.92648E-02

171

$E_{lab}(MeV)$	θ_{lab}	$Yield$	$dYield$
1.30991E+00	75.0	1.08528E-01	1.13140E-02
1.30500E+00	75.0	3.75076E-02	3.22839E-03
1.29471E+00	75.0	1.42187E-02	9.06578E-04
1.28480E+00	75.0	1.05241E-02	6.82080E-04
1.27475E+00	75.0	8.67912E-03	6.03397E-04
1.26458E+00	75.0	3.74747E-03	3.23902E-04
1.25396E+00	75.0	3.29269E-03	2.70664E-04
1.24486E+00	75.0	2.83567E-03	2.34666E-04
1.23481E+00	75.0	2.50312E-03	2.01121E-04
1.22497E+00	75.0	1.90688E-03	1.68538E-04
1.21353E+00	75.0	1.96479E-03	1.48101E-04
1.20539E+00	75.0	3.51711E-03	2.39182E-04
1.19567E+00	75.0	1.76576E-03	1.27088E-04
1.18598E+00	75.0	1.29065E-03	1.11098E-04
1.17633E+00	75.0	1.22437E-03	1.06968E-04
1.16672E+00	75.0	9.30212E-04	1.07410E-04
1.15715E+00	75.0	5.65985E-04	7.70192E-05
1.14762E+00	75.0	3.17490E-04	5.08266E-05
1.13813E+00	75.0	2.99682E-04	4.92873E-05
1.12868E+00	75.0	3.95737E-04	6.68985E-05
1.11927E+00	75.0	4.20904E-04	6.73871E-05

TABLE A.6

Continued

$E_{lab}(MeV)$	θ_{lab}	$Yield$	$dYield$
1.10989E+00	75.0	6.66964E-04	8.54025E-05
1.10056E+00	75.0	4.36653E-04	6.81960E-05
1.09127E+00	75.0	6.76517E-04	9.66588E-05
1.08201E+00	75.0	6.34443E-04	7.75142E-05
1.07280E+00	75.0	6.37714E-04	7.56726E-05
1.06362E+00	75.0	5.80799E-04	7.97655E-05
1.05449E+00	75.0	3.92316E-04	5.19866E-05
1.04539E+00	75.0	2.89368E-04	4.36293E-05
1.03633E+00	75.0	1.43620E-04	2.46361E-05
1.02717E+00	75.0	1.83366E-04	2.89972E-05
1.02717E+00	75.0	1.83366E-04	2.89972E-05

TABLE A.7

EXPERIMENTAL DATASET FOR $^{19}F(\alpha, p_1)^{22}Ne$

$E_{lab}(MeV)$	θ_{lab}	$Yield$	$dYield$
1.98058E+00	130.0	6.58601E-01	5.81136E-02
1.97596E+00	130.0	2.83923E-01	3.37617E-02
1.97135E+00	130.0	1.44089E-01	2.17227E-02

TABLE A.7

Continued

$E_{lab}(MeV)$	θ_{lab}	$Yield$	$dYield$
1.96570E+00	130.0	2.12690E-01	2.54624E-02
1.96089E+00	130.0	2.10425E-01	2.67215E-02
1.95567E+00	130.0	3.81539E-01	3.95352E-02
1.95108E+00	130.0	2.65449E-01	2.98324E-02
1.93611E+00	130.0	5.19659E-01	4.75727E-02
1.93113E+00	130.0	5.63621E-01	4.03438E-02
1.92574E+00	130.0	5.57814E-01	4.98242E-02
1.92574E+00	130.0	2.69439E-01	3.78324E-02
1.92078E+00	130.0	4.93882E-01	4.56621E-02
1.91582E+00	130.0	8.37958E-01	6.46930E-02
1.91086E+00	130.0	1.05496E+00	8.10645E-02
1.90571E+00	130.0	9.44435E-01	7.19761E-02
1.90118E+00	130.0	1.10181E+00	7.53937E-02
1.89584E+00	130.0	1.50450E+00	1.12745E-01
1.89112E+00	130.0	2.64574E+00	1.51796E-01
1.88620E+00	130.0	3.40318E+00	2.13929E-01
1.88026E+00	130.0	3.66481E+00	9.52282E-02
1.87597E+00	130.0	3.26371E+00	9.92217E-02
1.87086E+00	130.0	1.98694E+00	1.23951E-01
1.86597E+00	130.0	7.72497E-01	5.73002E-02
1.87127E+00	130.0	2.24640E+00	1.00171E-01

174

TABLE A.7

Continued

$E_{lab}(MeV)$	θ_{lab}	$Yield$	$dYield$
1.86637E+00	130.0	1.07114E+00	7.64963E-02
1.86108E+00	130.0	5.03711E-01	4.17740E-02
1.85579E+00	130.0	1.96770E-01	2.04901E-02
1.85092E+00	130.0	1.28232E-01	1.55029E-02
1.84605E+00	130.0	1.16689E-01	1.39195E-02
1.84078E+00	130.0	6.19916E-02	8.41299E-03
1.83471E+00	130.0	5.34358E-02	6.91887E-03
1.82906E+00	130.0	3.84683E-02	4.88852E-03
1.82402E+00	130.0	2.86823E-02	3.55330E-03
1.81878E+00	130.0	4.44018E-02	5.68185E-03
1.81376E+00	130.0	2.92089E-02	4.32871E-03
1.80834E+00	130.0	2.20788E-02	4.26608E-03
1.80413E+00	130.0	1.92563E-02	3.26621E-03
1.79872E+00	130.0	1.37767E-02	3.01405E-03
1.79352E+00	130.0	1.72200E-02	3.32462E-03
1.78833E+00	130.0	1.87483E-02	3.62031E-03
1.78374E+00	130.0	1.47884E-02	2.96513E-03
1.77379E+00	130.0	9.48382E-03	2.23883E-03
1.76863E+00	130.0	9.31573E-03	2.19910E-03
1.76308E+00	130.0	5.53042E-03	1.08567E-03
1.75754E+00	130.0	1.79246E-03	6.33926E-04

175

TABLE A.7

Continued

$E_{lab}(MeV)$	θ_{lab}	$Yield$	$dYield$
1.75299E+00	130.0	7.56322E-03	1.51465E-03
1.74766E+00	130.0	5.91557E-03	1.32411E-03
1.74234E+00	130.0	6.50517E-03	1.53500E-03
1.73664E+00	130.0	6.06356E-03	1.32441E-03
1.73212E+00	130.0	8.53126E-03	1.48708E-03
1.72721E+00	130.0	6.39813E-03	9.34235E-04
1.72212E+00	130.0	3.35503E-03	7.70051E-04
1.71703E+00	130.0	5.00668E-03	1.14939E-03
1.71195E+00	130.0	1.34275E-02	2.12705E-03
1.70688E+00	130.0	1.95938E-02	2.80723E-03
1.70201E+00	130.0	1.17385E-02	2.26269E-03
1.69695E+00	130.0	2.02208E-02	2.92766E-03
1.69171E+00	130.0	2.15594E-02	3.08996E-03
1.68706E+00	130.0	2.93304E-02	4.60161E-03
1.67680E+00	130.0	7.71318E-02	6.64215E-03
1.66947E+00	130.0	1.27195E-01	1.23621E-02
1.66504E+00	130.0	1.03146E-01	8.34760E-03
1.66023E+00	130.0	1.18782E-01	8.99379E-03
1.65543E+00	130.0	9.18058E-02	7.37881E-03
1.65121E+00	130.0	2.69723E-02	3.86912E-03
1.64584E+00	130.0	3.25557E-02	3.59204E-03

TABLE A.7

Continued

$E_{lab}(MeV)$	θ_{lab}	$Yield$	$dYield$
1.64049E+00	130.0	1.04375E-02	2.05057E-03
1.63495E+00	130.0	7.11439E-03	1.22185E-03
1.63495E+00	130.0	4.61433E-03	1.15398E-03
1.62923E+00	130.0	1.58448E-02	2.39182E-03
1.98058E+00	90.0	7.68240E-01	5.95226E-02
1.97596E+00	90.0	3.73766E-01	3.66627E-02
1.97135E+00	90.0	3.14753E-01	3.13111E-02
1.96570E+00	90.0	2.77651E-01	2.73630E-02
1.96089E+00	90.0	3.91097E-01	3.56258E-02
1.95567E+00	90.0	4.22907E-01	3.89933E-02
1.95108E+00	90.0	5.17641E-01	4.14656E-02
1.93611E+00	90.0	5.11531E-01	4.37298E-02
1.93113E+00	90.0	5.46641E-01	3.67061E-02
1.92574E+00	90.0	5.02276E-01	4.32254E-02
1.92574E+00	90.0	4.59069E-01	4.81154E-02
1.92078E+00	90.0	6.12875E-01	4.85897E-02
1.91582E+00	90.0	8.15932E-01	5.95088E-02
1.91086E+00	90.0	8.46969E-01	6.52920E-02
1.90571E+00	90.0	9.40626E-01	6.72177E-02
1.90118E+00	90.0	1.17837E+00	7.43322E-02
1.89584E+00	90.0	1.59895E+00	1.11309E-01

177

TABLE A.7

Continued

$E_{lab}(MeV)$	θ_{lab}	$Yield$	$dYield$
1.89112E+00	90.0	3.08216E+00	1.64109E-01
1.88620E+00	90.0	4.00118E+00	2.36984E-01
1.88026E+00	90.0	4.86363E+00	1.17354E-01
1.87597E+00	90.0	4.39882E+00	1.22618E-01
1.87086E+00	90.0	2.91511E+00	1.59997E-01
1.86597E+00	90.0	1.27387E+00	7.57329E-02
1.87127E+00	90.0	3.09260E+00	1.24181E-01
1.86637E+00	90.0	2.00456E+00	1.14171E-01
1.86108E+00	90.0	7.95776E-01	5.17946E-02
1.85579E+00	90.0	3.97104E-01	2.78725E-02
1.85092E+00	90.0	2.68184E-01	2.11790E-02
1.84605E+00	90.0	1.67763E-01	1.53294E-02
1.84078E+00	90.0	1.37560E-01	1.15881E-02
1.83471E+00	90.0	9.10757E-02	8.23926E-03
1.82906E+00	90.0	6.84483E-02	5.93667E-03
1.82402E+00	90.0	5.57798E-02	4.50577E-03
1.81878E+00	90.0	8.14547E-02	7.00163E-03
1.81376E+00	90.0	5.98470E-02	5.62824E-03
1.80834E+00	90.0	4.38524E-02	5.45052E-03
1.80413E+00	90.0	3.12943E-02	3.76631E-03
1.79872E+00	90.0	2.93212E-02	3.98021E-03

178

TABLE A.7

Continued

$E_{lab}(MeV)$	θ_{lab}	$Yield$	$dYield$
1.79352E+00	90.0	2.59157E-02	3.68675E-03
1.78833E+00	90.0	1.74949E-02	3.15437E-03
1.78374E+00	90.0	2.35590E-02	3.38215E-03
1.77379E+00	90.0	2.22715E-02	3.10236E-03
1.76863E+00	90.0	1.47258E-02	2.49652E-03
1.76308E+00	90.0	1.50453E-02	1.61833E-03
1.75754E+00	90.0	1.31166E-02	1.55009E-03
1.75299E+00	90.0	1.05777E-02	1.61677E-03
1.74766E+00	90.0	1.08235E-02	1.61717E-03
1.74234E+00	90.0	1.26385E-02	1.93250E-03
1.73664E+00	90.0	1.00979E-02	1.54285E-03
1.73212E+00	90.0	8.41083E-03	1.33201E-03
1.72721E+00	90.0	5.53649E-03	7.83845E-04
1.72212E+00	90.0	5.74569E-03	9.09355E-04
1.71703E+00	90.0	1.11478E-02	1.54879E-03
1.71195E+00	90.0	1.47479E-02	2.01200E-03
1.70688E+00	90.0	2.44014E-02	2.83013E-03
1.70201E+00	90.0	2.65333E-02	3.07741E-03
1.69695E+00	90.0	3.80514E-02	3.63753E-03
1.69171E+00	90.0	3.04372E-02	3.32003E-03
1.68706E+00	90.0	5.47286E-02	5.70392E-03

179

TABLE A.7

Continued

$E_{lab}(MeV)$	θ_{lab}	$Yield$	$dYield$
1.67680E+00	90.0	9.59958E-02	6.72562E-03
1.66947E+00	90.0	1.46839E-01	1.20777E-02
1.66504E+00	90.0	1.48813E-01	9.16378E-03
1.66023E+00	90.0	1.37851E-01	8.80970E-03
1.65543E+00	90.0	7.05202E-02	5.83119E-03
1.65121E+00	90.0	2.19631E-02	3.15056E-03
1.64584E+00	90.0	1.46925E-02	2.17255E-03
1.64049E+00	90.0	1.40577E-02	2.15002E-03
1.63495E+00	90.0	3.83460E-02	2.58042E-03
1.63495E+00	90.0	1.64424E-02	1.96820E-03
1.62923E+00	90.0	1.40796E-02	2.03512E-03
1.98058E+00	30.0	8.39145E-01	6.15181E-02
1.97596E+00	30.0	2.60116E-01	2.84832E-02
1.97135E+00	30.0	2.02594E-01	2.32672E-02
1.96570E+00	30.0	1.90384E-01	2.11496E-02
1.96089E+00	30.0	2.80235E-01	2.80929E-02
1.95567E+00	30.0	3.57303E-01	3.40293E-02
1.95108E+00	30.0	3.59703E-01	3.19192E-02
1.93611E+00	30.0	4.94034E-01	4.16010E-02
1.93113E+00	30.0	4.47953E-01	3.13898E-02
1.92574E+00	30.0	4.15828E-01	3.72201E-02

TABLE A.7

Continued

$E_{lab}(MeV)$	θ_{lab}	$Yield$	$dYield$
1.92574E+00	30.0	4.91591E-01	4.89080E-02
1.92078E+00	30.0	5.78537E-01	4.55400E-02
1.91582E+00	30.0	8.38764E-01	5.92859E-02
1.91086E+00	30.0	1.02985E+00	7.34253E-02
1.90571E+00	30.0	9.93008E-01	6.82429E-02
1.90118E+00	30.0	9.61667E-01	6.28628E-02
1.89584E+00	30.0	1.20623E+00	8.86990E-02
1.89112E+00	30.0	2.37145E+00	1.30898E-01
1.88620E+00	30.0	3.08150E+00	1.87606E-01
1.88026E+00	30.0	3.35814E+00	8.44172E-02
1.87597E+00	30.0	2.96870E+00	8.70413E-02
1.87086E+00	30.0	1.76818E+00	1.05858E-01
1.86597E+00	30.0	7.57839E-01	5.13621E-02
1.87127E+00	30.0	2.06264E+00	8.80300E-02
1.86637E+00	30.0	1.11571E+00	7.21821E-02
1.86108E+00	30.0	4.33887E-01	3.41156E-02
1.85579E+00	30.0	2.51757E-01	2.06939E-02
1.85092E+00	30.0	1.75543E-01	1.61235E-02
1.84605E+00	30.0	1.29165E-01	1.28453E-02
1.84078E+00	30.0	7.57132E-02	8.13681E-03
1.83471E+00	30.0	9.15334E-02	7.96175E-03

TABLE A.7

Continued

$E_{lab}(MeV)$	θ_{lab}	$Yield$	$dYield$
1.82906E+00	30.0	6.10587E-02	5.39079E-03
1.82402E+00	30.0	5.22864E-02	4.19789E-03
1.81878E+00	30.0	7.27123E-02	6.36107E-03
1.81376E+00	30.0	4.58541E-02	4.72992E-03
1.80834E+00	30.0	5.65977E-02	5.98082E-03
1.80413E+00	30.0	3.64285E-02	3.91710E-03
1.79872E+00	30.0	3.06085E-02	3.91669E-03
1.79352E+00	30.0	3.40816E-02	4.07874E-03
1.78833E+00	30.0	2.92715E-02	3.93894E-03
1.78374E+00	30.0	2.85024E-02	3.58570E-03
1.77379E+00	30.0	2.81721E-02	3.36388E-03
1.76863E+00	30.0	2.06604E-02	2.85070E-03
1.76308E+00	30.0	1.18579E-02	1.38231E-03
1.75754E+00	30.0	1.94144E-02	1.81841E-03
1.75299E+00	30.0	1.50466E-02	1.85858E-03
1.74766E+00	30.0	1.29298E-02	1.70279E-03
1.74234E+00	30.0	1.47119E-02	2.00877E-03
1.73664E+00	30.0	1.69805E-02	1.92932E-03
1.73212E+00	30.0	1.71550E-02	1.83520E-03
1.72721E+00	30.0	7.90534E-03	9.02432E-04
1.72212E+00	30.0	8.52445E-03	1.06721E-03

TABLE A.7

Continued

$E_{lab}(MeV)$	θ_{lab}	$Yield$	$dYield$
1.71703E+00	30.0	7.75345E-03	1.24327E-03
1.71195E+00	30.0	1.87435E-02	2.18642E-03
1.70688E+00	30.0	2.17274E-02	2.57150E-03
1.70201E+00	30.0	2.59248E-02	2.93042E-03
1.69695E+00	30.0	2.57592E-02	2.87709E-03
1.69171E+00	30.0	2.49165E-02	2.89146E-03
1.68706E+00	30.0	3.13322E-02	4.14075E-03
1.67680E+00	30.0	8.78195E-02	6.19547E-03
1.66947E+00	30.0	1.35414E-01	1.11720E-02
1.66504E+00	30.0	1.35665E-01	8.42535E-03
1.66023E+00	30.0	1.41359E-01	8.61825E-03
1.65543E+00	30.0	1.20465E-01	7.41994E-03
1.65121E+00	30.0	3.20443E-02	3.67548E-03
1.64584E+00	30.0	5.63505E-03	1.29431E-03
1.64049E+00	30.0	1.39654E-02	2.06550E-03
1.63495E+00	30.0	3.16322E-02	2.63508E-03
1.62923E+00	30.0	2.37034E-02	2.54783E-03
1.67854E+00	120.0	3.36704E-02	3.62215E-03
1.67313E+00	120.0	5.89113E-02	4.83162E-03
1.66947E+00	120.0	1.15706E-01	6.88439E-03
1.66407E+00	120.0	3.83933E-01	1.28363E-02

183

TABLE A.7

Continued

$E_{lab}(MeV)$	θ_{lab}	$Yield$	$dYield$
1.65869E+00	120.0	3.46290E-01	1.28270E-02
1.65389E+00	120.0	2.03895E-01	9.24961E-03
1.64891E+00	120.0	3.69887E-02	3.93195E-03
1.64335E+00	120.0	8.51914E-03	1.38425E-03
1.63877E+00	120.0	7.99245E-03	1.28196E-03
1.63361E+00	120.0	6.12696E-03	1.12000E-03
1.62866E+00	120.0	1.50926E-02	1.98495E-03
1.62371E+00	120.0	1.29516E-02	1.89159E-03
1.61840E+00	120.0	1.41871E-02	1.71062E-03
1.61346E+00	120.0	1.14660E-02	1.86215E-03
1.60854E+00	120.0	1.07586E-02	1.68215E-03
1.60381E+00	120.0	1.33989E-02	1.93671E-03
1.59872E+00	120.0	1.32303E-02	2.02062E-03
1.59400E+00	120.0	1.37420E-02	2.26243E-03
1.58911E+00	120.0	2.04471E-02	2.95840E-03
1.58385E+00	120.0	2.05863E-02	2.94761E-03
1.57897E+00	120.0	2.91690E-02	2.91038E-03
1.57373E+00	120.0	3.20157E-02	3.18046E-03
1.56905E+00	120.0	2.59111E-02	2.83419E-03
1.56401E+00	120.0	2.57225E-02	2.83098E-03
1.55879E+00	120.0	2.51168E-02	2.96844E-03

184

TABLE A.7

Continued

$E_{lab}(MeV)$	θ_{lab}	$Yield$	$dYield$
1.55414E+00	120.0	2.73679E-02	3.10888E-03
1.54893E+00	120.0	2.76635E-02	3.08364E-03
1.54392E+00	120.0	3.53021E-02	3.63618E-03
1.53892E+00	120.0	3.58828E-02	3.67684E-03
1.53393E+00	120.0	5.15819E-02	4.48372E-03
1.52913E+00	120.0	7.31941E-02	5.39747E-03
1.52378E+00	120.0	9.16728E-02	6.04067E-03
1.51881E+00	120.0	1.22794E-01	6.28832E-03
1.51881E+00	120.0	1.42065E-01	8.56048E-03
1.51349E+00	120.0	1.50774E-01	9.01047E-03
1.50890E+00	120.0	1.89013E-01	1.05408E-02
1.50359E+00	120.0	2.02182E-01	9.65897E-03
1.49829E+00	120.0	2.68181E-01	1.12375E-02
1.49373E+00	120.0	2.21813E-01	1.46007E-02
1.48826E+00	120.0	1.86117E-01	1.18838E-02
1.48335E+00	120.0	1.14800E-01	6.54710E-03
1.47863E+00	120.0	1.53272E-01	6.74175E-03
1.47302E+00	120.0	2.27242E-01	8.42852E-03
1.46795E+00	120.0	2.83175E-01	1.10468E-02
1.46271E+00	120.0	4.18912E-01	1.36409E-02
1.45875E+00	120.0	4.12782E-01	1.34150E-02

TABLE A.7

Continued

$E_{lab}(MeV)$	θ_{lab}	$Yield$	$dYield$
1.45370E+00	120.0	3.30387E-01	1.18082E-02
1.44831E+00	120.0	2.14375E-01	9.52049E-03
1.44311E+00	120.0	1.05987E-01	5.43700E-03
1.43792E+00	120.0	1.12159E-01	5.32615E-03
1.43256E+00	120.0	5.55112E-02	3.13102E-03
1.42738E+00	120.0	4.44422E-02	2.96607E-03
1.42133E+00	120.0	3.60455E-02	3.72031E-03
1.41706E+00	120.0	3.63810E-02	3.66016E-03
1.41174E+00	120.0	4.89261E-02	4.24438E-03
1.40696E+00	120.0	7.69239E-02	5.35847E-03
1.40201E+00	120.0	1.09635E-01	6.40415E-03
1.39707E+00	120.0	1.52760E-01	7.69864E-03
1.39196E+00	120.0	1.50624E-01	7.45107E-03
1.38703E+00	120.0	8.39687E-02	5.55289E-03
1.38194E+00	120.0	3.89943E-02	3.80746E-03
1.37651E+00	120.0	5.74403E-02	3.74603E-03
1.37126E+00	120.0	8.67849E-02	5.67577E-03
1.36568E+00	120.0	9.70328E-02	6.89392E-03
1.36010E+00	120.0	8.53566E-02	6.95078E-03
1.35454E+00	120.0	3.29274E-02	3.84316E-03
1.34934E+00	120.0	1.70378E-02	2.34498E-03

186

TABLE A.7

Continued

$E_{lab}(MeV)$	θ_{lab}	$Yield$	$dYield$
1.34380E+00	120.0	1.15419E-02	1.51765E-03
1.33827E+00	120.0	2.21029E-02	2.79259E-03
1.33361E+00	120.0	3.16381E-02	3.50847E-03
1.32845E+00	120.0	6.50481E-02	5.66235E-03
1.32347E+00	120.0	7.96091E-02	9.27701E-03
1.31901E+00	120.0	6.57352E-02	6.62528E-03
1.31370E+00	120.0	3.11732E-02	4.33946E-03
1.30909E+00	120.0	1.35737E-02	1.90366E-03
1.30602E+00	120.0	7.99779E-03	3.26940E-03
1.30074E+00	120.0	2.31766E-03	4.54678E-04
1.29598E+00	120.0	5.29948E-03	8.18064E-04
1.29038E+00	120.0	3.23337E-03	6.34298E-04
1.28463E+00	120.0	3.01235E-03	6.42378E-04
1.27973E+00	120.0	4.70810E-03	7.96087E-04
1.27467E+00	120.0	3.41764E-03	6.97795E-04
1.27012E+00	120.0	2.90011E-03	6.18437E-04
1.26391E+00	120.0	5.68265E-03	7.96083E-04
1.25721E+00	120.0	5.29442E-03	9.08338E-04
1.25103E+00	120.0	2.94764E-03	6.44657E-04
1.24569E+00	120.0	2.05502E-03	4.38272E-04
1.24070E+00	120.0	1.14474E-03	2.09048E-04

TABLE A.7

Continued

$E_{lab}(MeV)$	θ_{lab}	$Yield$	$dYield$
1.23523E+00	120.0	1.12973E-03	2.91782E-04
1.22943E+00	120.0	1.94036E-03	2.66624E-04
1.22398E+00	120.0	4.64633E-03	6.64239E-04
1.67854E+00	100.0	2.43691E-02	2.83588E-03
1.67313E+00	100.0	4.41812E-02	3.84806E-03
1.66947E+00	100.0	9.99224E-02	5.89798E-03
1.66407E+00	100.0	3.54336E-01	1.13912E-02
1.65869E+00	100.0	3.21760E-01	1.14208E-02
1.65389E+00	100.0	1.64189E-01	7.64353E-03
1.64891E+00	100.0	3.74182E-02	3.64669E-03
1.64335E+00	100.0	4.95110E-03	9.72080E-04
1.63877E+00	100.0	3.65566E-03	7.98448E-04
1.63361E+00	100.0	3.64326E-03	7.95709E-04
1.62866E+00	100.0	1.19369E-02	1.62685E-03
1.62371E+00	100.0	9.13017E-03	1.46354E-03
1.61840E+00	100.0	9.78201E-03	1.30885E-03
1.61346E+00	100.0	9.48512E-03	1.56108E-03
1.60854E+00	100.0	1.44915E-02	1.80074E-03
1.60381E+00	100.0	1.01986E-02	1.55725E-03
1.59872E+00	100.0	1.07188E-02	1.67639E-03
1.59400E+00	100.0	1.76732E-02	2.36683E-03

188

TABLE A.7

Continued

$E_{lab}(MeV)$	θ_{lab}	$Yield$	$dYield$
1.58911E+00	100.0	1.59265E-02	2.40632E-03
1.58385E+00	100.0	1.35668E-02	2.20472E-03
1.57897E+00	100.0	2.08616E-02	2.26798E-03
1.57373E+00	100.0	1.41379E-02	1.94531E-03
1.56905E+00	100.0	1.59918E-02	2.05126E-03
1.56401E+00	100.0	2.23889E-02	2.43508E-03
1.55879E+00	100.0	1.98656E-02	2.43338E-03
1.55414E+00	100.0	1.69994E-02	2.25698E-03
1.54893E+00	100.0	1.48055E-02	2.07739E-03
1.54392E+00	100.0	2.74817E-02	2.95697E-03
1.53892E+00	100.0	3.39996E-02	3.30144E-03
1.53393E+00	100.0	3.99250E-02	3.63512E-03
1.52913E+00	100.0	6.18937E-02	4.57620E-03
1.52378E+00	100.0	6.66632E-02	4.74284E-03
1.51881E+00	100.0	8.52268E-02	4.81850E-03
1.51881E+00	100.0	1.12678E-01	7.02345E-03
1.51349E+00	100.0	1.41551E-01	8.06206E-03
1.50890E+00	100.0	1.41950E-01	8.40490E-03
1.50359E+00	100.0	2.01080E-01	8.90884E-03
1.49829E+00	100.0	2.42282E-01	9.86182E-03
1.49373E+00	100.0	1.84701E-01	1.22815E-02

189

TABLE A.7

Continued

$E_{lab}(MeV)$	θ_{lab}	$Yield$	$dYield$
1.48826E+00	100.0	1.54557E-01	9.98235E-03
1.48335E+00	100.0	1.01651E-01	5.68468E-03
1.47863E+00	100.0	1.35476E-01	5.84925E-03
1.47302E+00	100.0	1.86625E-01	7.03983E-03
1.46795E+00	100.0	2.30834E-01	9.18792E-03
1.46271E+00	100.0	3.36255E-01	1.12498E-02
1.45875E+00	100.0	3.59106E-01	1.15489E-02
1.45370E+00	100.0	2.86501E-01	1.01470E-02
1.44831E+00	100.0	1.97688E-01	8.44398E-03
1.44311E+00	100.0	1.02053E-01	4.92682E-03
1.43792E+00	100.0	1.03889E-01	4.73169E-03
1.43256E+00	100.0	5.00532E-02	2.74338E-03
1.42738E+00	100.0	3.86489E-02	2.55179E-03
1.42133E+00	100.0	3.19635E-02	3.23247E-03
1.41706E+00	100.0	3.83887E-02	3.47331E-03
1.41174E+00	100.0	4.47201E-02	3.74552E-03
1.40696E+00	100.0	8.25312E-02	5.13586E-03
1.40201E+00	100.0	1.06240E-01	5.82907E-03
1.39707E+00	100.0	1.44566E-01	6.92556E-03
1.39196E+00	100.0	1.25796E-01	6.27971E-03
1.38703E+00	100.0	9.25480E-02	5.39648E-03

190

TABLE A.7

Continued

$E_{lab}(MeV)$	θ_{lab}	$Yield$	$dYield$
1.38194E+00	100.0	4.10212E-02	3.60742E-03
1.37651E+00	100.0	5.56483E-02	3.40571E-03
1.37126E+00	100.0	9.98467E-02	5.63854E-03
1.36568E+00	100.0	7.69115E-02	5.65841E-03
1.36010E+00	100.0	7.22000E-02	5.89819E-03
1.35454E+00	100.0	3.56127E-02	3.69196E-03
1.34934E+00	100.0	2.05291E-02	2.37718E-03
1.34380E+00	100.0	1.25394E-02	1.46027E-03
1.33827E+00	100.0	1.46393E-02	2.09594E-03
1.33361E+00	100.0	3.12145E-02	3.21806E-03
1.32845E+00	100.0	5.25037E-02	4.69279E-03
1.32347E+00	100.0	6.50914E-02	7.73883E-03
1.31901E+00	100.0	4.08711E-02	4.81113E-03
1.31370E+00	100.0	1.42973E-02	2.70749E-03
1.30909E+00	100.0	2.49384E-03	7.52175E-04
1.30602E+00	100.0	4.54193E-03	2.27297E-03
1.30074E+00	100.0	1.67059E-03	3.56269E-04
1.29598E+00	100.0	3.43973E-03	6.08256E-04
1.29038E+00	100.0	3.49632E-03	6.08852E-04
1.28463E+00	100.0	2.91650E-03	5.83446E-04
1.27973E+00	100.0	3.09447E-03	5.95689E-04

191

TABLE A.7

Continued

$E_{lab}(MeV)$	θ_{lab}	$Yield$	$dYield$
1.27467E+00	100.0	4.00415E-03	6.97269E-04
1.27012E+00	100.0	2.80823E-03	5.61781E-04
1.26391E+00	100.0	3.03849E-03	5.37284E-04
1.25721E+00	100.0	4.64477E-03	7.85423E-04
1.25103E+00	100.0	1.31596E-03	3.97240E-04
1.24569E+00	100.0	9.55421E-04	2.75854E-04
1.24070E+00	100.0	3.25258E-04	1.02863E-04
1.23523E+00	100.0	7.06202E-04	2.12975E-04
1.22943E+00	100.0	1.87256E-04	7.64502E-05
1.22398E+00	100.0	1.05090E-03	2.91522E-04
1.67854E+00	40.0	2.38766E-02	2.69173E-03
1.67313E+00	40.0	4.32732E-02	3.65384E-03
1.66947E+00	40.0	8.75311E-02	5.28537E-03
1.66407E+00	40.0	3.41724E-01	1.07386E-02
1.65869E+00	40.0	3.32719E-01	1.11697E-02
1.65389E+00	40.0	1.95365E-01	8.02651E-03
1.64891E+00	40.0	4.76936E-02	3.95216E-03
1.64335E+00	40.0	8.40202E-03	1.21524E-03
1.63877E+00	40.0	4.64087E-03	8.62859E-04
1.63361E+00	40.0	5.10414E-03	9.03475E-04
1.62866E+00	40.0	1.07726E-02	1.48191E-03

192

TABLE A.7

Continued

$E_{lab}(MeV)$	θ_{lab}	$Yield$	$dYield$
1.62371E+00	40.0	1.37779E-02	1.72523E-03
1.61840E+00	40.0	1.23700E-02	1.41217E-03
1.61346E+00	40.0	1.39116E-02	1.81434E-03
1.60854E+00	40.0	1.64065E-02	1.83845E-03
1.60381E+00	40.0	1.26553E-02	1.66457E-03
1.59872E+00	40.0	1.29890E-02	1.77089E-03
1.59400E+00	40.0	2.11987E-02	2.48818E-03
1.58911E+00	40.0	2.53156E-02	2.91496E-03
1.58385E+00	40.0	2.13581E-02	2.65716E-03
1.57897E+00	40.0	3.52414E-02	2.83350E-03
1.57373E+00	40.0	2.97127E-02	2.71170E-03
1.56905E+00	40.0	4.22376E-02	3.20945E-03
1.56401E+00	40.0	3.46809E-02	2.91353E-03
1.55879E+00	40.0	3.00338E-02	2.87601E-03
1.55414E+00	40.0	3.26843E-02	3.01102E-03
1.54893E+00	40.0	2.45993E-02	2.57405E-03
1.54392E+00	40.0	3.20073E-02	3.06568E-03
1.53892E+00	40.0	4.47879E-02	3.64382E-03
1.53393E+00	40.0	4.25139E-02	3.60375E-03
1.52913E+00	40.0	6.68441E-02	4.57158E-03
1.52378E+00	40.0	8.52746E-02	5.16662E-03

Continued

$E_{lab}(MeV)$	θ_{lab}	$Yield$	$dYield$
1.51881E+00	40.0	1.11444E-01	5.31450E-03
1.51881E+00	40.0	1.15653E-01	6.84090E-03
1.51349E+00	40.0	1.38685E-01	7.66891E-03
1.50890E+00	40.0	1.55258E-01	8.46567E-03
1.50359E+00	40.0	1.99358E-01	8.53056E-03
1.49829E+00	40.0	2.46811E-01	9.57897E-03
1.49373E+00	40.0	1.94972E-01	1.21504E-02
1.48826E+00	40.0	1.59151E-01	9.74923E-03
1.48335E+00	40.0	1.23689E-01	6.04944E-03
1.47863E+00	40.0	1.46333E-01	5.85633E-03
1.47302E+00	40.0	2.39265E-01	7.70999E-03
1.46795E+00	40.0	2.68884E-01	9.59237E-03
1.46271E+00	40.0	3.93497E-01	1.17915E-02
1.45875E+00	40.0	3.68542E-01	1.12817E-02
1.45370E+00	40.0	2.83612E-01	9.71822E-03
1.44831E+00	40.0	1.98242E-01	8.13674E-03
1.44311E+00	40.0	9.74501E-02	4.62768E-03
1.43792E+00	40.0	9.14367E-02	4.26383E-03
1.43256E+00	40.0	5.66493E-02	2.80857E-03
1.42738E+00	40.0	3.81591E-02	2.43776E-03
1.42133E+00	40.0	3.19126E-02	3.10589E-03

TABLE A.7

Continued

$E_{lab}(MeV)$	θ_{lab}	$Yield$	$dYield$
1.41706E+00	40.0	3.34636E-02	3.11564E-03
1.41174E+00	40.0	5.15791E-02	3.87468E-03
1.40696E+00	40.0	8.02798E-02	4.87300E-03
1.40201E+00	40.0	9.93253E-02	5.41951E-03
1.39707E+00	40.0	1.48536E-01	6.76660E-03
1.39196E+00	40.0	1.59410E-01	6.84696E-03
1.38703E+00	40.0	9.54479E-02	5.27846E-03
1.38194E+00	40.0	3.82201E-02	3.34849E-03
1.37651E+00	40.0	6.35713E-02	3.50809E-03
1.37126E+00	40.0	1.04357E-01	5.55432E-03
1.36568E+00	40.0	1.24599E-01	6.98506E-03
1.36010E+00	40.0	8.64430E-02	6.22642E-03
1.35454E+00	40.0	5.57385E-02	4.45853E-03
1.34934E+00	40.0	3.06501E-02	2.79903E-03
1.34380E+00	40.0	3.02692E-02	2.18896E-03
1.33827E+00	40.0	3.59526E-02	3.17165E-03
1.33361E+00	40.0	4.92790E-02	3.90368E-03
1.32845E+00	40.0	5.93323E-02	4.80789E-03
1.32347E+00	40.0	6.53003E-02	7.46450E-03
1.31901E+00	40.0	5.34085E-02	5.30518E-03
1.31370E+00	40.0	2.60135E-02	3.52183E-03

TABLE A.7

Continued

$E_{lab}(MeV)$	θ_{lab}	$Yield$	$dYield$
1.30909E+00	40.0	5.67066E-03	1.09222E-03
1.30602E+00	40.0	1.05198E-03	1.05222E-03
1.30074E+00	40.0	1.12579E-03	2.81504E-04
1.29598E+00	40.0	1.89267E-03	4.34288E-04
1.29038E+00	40.0	1.57119E-03	3.92866E-04
1.28463E+00	40.0	4.21760E-03	6.75620E-04
1.27973E+00	40.0	2.33766E-03	4.98498E-04
1.27467E+00	40.0	3.71283E-03	6.46541E-04
1.27012E+00	40.0	4.16680E-03	6.59082E-04
1.26391E+00	40.0	6.16495E-03	7.37301E-04
1.25721E+00	40.0	5.78626E-03	8.44465E-04
1.25103E+00	40.0	2.77504E-03	5.56477E-04
1.24569E+00	40.0	2.36432E-03	4.18150E-04
1.24070E+00	40.0	2.71691E-04	9.05696E-05
1.23523E+00	40.0	2.97973E-04	1.33271E-04
1.22943E+00	40.0	8.69258E-05	5.01876E-05
1.22398E+00	40.0	6.75567E-04	2.25219E-04
1.35948E+00	120.0	9.39927E-02	8.07291E-03
1.35431E+00	120.0	3.37371E-02	5.81678E-03
1.34915E+00	120.0	2.51174E-02	5.25757E-03
1.34400E+00	120.0	1.23173E-02	5.86712E-03

TABLE A.7

Continued

$E_{lab}(MeV)$	θ_{lab}	$Yield$	$dYield$
1.33886E+00	120.0	2.26464E-02	5.95830E-03
1.33373E+00	120.0	1.29290E-02	6.46215E-03
1.32860E+00	120.0	5.93396E-02	6.66064E-03
1.32349E+00	120.0	8.27453E-02	7.24724E-03
1.31840E+00	120.0	8.93434E-02	7.29396E-03
1.31330E+00	120.0	5.19259E-02	5.27450E-03
1.30822E+00	120.0	1.51622E-02	3.67590E-03
1.30314E+00	120.0	1.29356E-03	1.93916E-03
1.28799E+00	120.0	1.82799E-03	5.71088E-04
1.28295E+00	120.0	1.83412E-03	6.32297E-04
1.27793E+00	120.0	2.27894E-03	5.12733E-04
1.27176E+00	120.0	3.68917E-03	4.54835E-04
1.26792E+00	120.0	3.73192E-03	4.23231E-04
1.26259E+00	120.0	3.51551E-03	4.11410E-04
1.25761E+00	120.0	4.02192E-03	5.15568E-04
1.25263E+00	120.0	5.43541E-03	4.32285E-04
1.24800E+00	120.0	4.64919E-03	3.83692E-04
1.24322E+00	120.0	3.78085E-03	3.38944E-04
1.23810E+00	120.0	2.06906E-03	2.47469E-04
1.23301E+00	120.0	1.94132E-03	2.34663E-04
1.22791E+00	120.0	1.55469E-03	1.82919E-04

TABLE A.7

Continued

$E_{lab}(MeV)$	θ_{lab}	$Yield$	$dYield$
1.22317E+00	120.0	1.10398E-03	2.10283E-04
1.21793E+00	120.0	1.12889E-03	1.75221E-04
1.21353E+00	120.0	1.38512E-03	2.00528E-04
1.20864E+00	120.0	9.41576E-04	1.59304E-04
1.20377E+00	120.0	1.48963E-03	1.71845E-04
1.19890E+00	120.0	1.42644E-03	1.67741E-04
1.19405E+00	120.0	9.86813E-04	2.06914E-04
1.18921E+00	120.0	1.61300E-03	1.67374E-04
1.18437E+00	120.0	1.58510E-03	1.50923E-04
1.17954E+00	120.0	1.48145E-03	2.05303E-04
1.17472E+00	120.0	1.27191E-03	1.75850E-04
1.16992E+00	120.0	2.26981E-03	1.91271E-04
1.16512E+00	120.0	2.14473E-03	1.92523E-04
1.16033E+00	120.0	2.24808E-03	2.10226E-04
1.15556E+00	120.0	2.29944E-03	1.72429E-04
1.15080E+00	120.0	2.25770E-03	1.75482E-04
1.14604E+00	120.0	2.23229E-03	1.25442E-04
1.14129E+00	120.0	2.48053E-03	1.02943E-04
1.13655E+00	120.0	2.46519E-03	1.16962E-04
1.13057E+00	120.0	2.52032E-03	1.31789E-04
1.12569E+00	120.0	2.68659E-03	1.38877E-04

198

$E_{lab}(MeV)$	θ_{lab}	$Yield$	$dYield$
1.12083E+00	120.0	2.72661E-03	1.39946E-04
1.11613E+00	120.0	1.37773E-03	1.49545E-04
1.11146E+00	120.0	1.83387E-03	1.33955E-04
1.10678E+00	120.0	1.39262E-03	1.20149E-04
1.10212E+00	120.0	1.49331E-03	1.26482E-04
1.09746E+00	120.0	6.85099E-04	1.30445E-04
1.09234E+00	120.0	2.04112E-04	1.11335E-04
1.08818E+00	120.0	4.88948E-04	1.11135E-04
1.08355E+00	120.0	4.03747E-04	1.09111E-04
1.07893E+00	120.0	6.11299E-04	1.17109E-04
1.07417E+00	120.0	1.04754E-04	1.22219E-04
1.06973E+00	120.0	3.40923E-04	1.02265E-04
1.06057E+00	120.0	1.43170E-04	7.81087E-05
1.05600E+00	120.0	2.17695E-04	8.46669E-05
1.05145E+00	120.0	9.26224E-05	5.40268E-05
1.04690E+00	120.0	6.95142E-05	5.40718E-05
1.04236E+00	120.0	4.31876E-05	4.31876E-05
1.03257E+00	120.0	6.07732E-05	6.07732E-05
1.02731E+00	120.0	6.01126E-05	3.43517E-05
1.02281E+00	120.0	8.47062E-06	5.08261E-05
1.01386E+00	120.0	4.07856E-05	5.09820E-05

199

TABLE A.7

Continued

$E_{lab}(MeV)$	θ_{lab}	$Yield$	$dYield$
1.00494E+00	120.0	9.81973E-05	4.36420E-05
9.96055E-01	120.0	8.17430E-06	4.08657E-05
9.66745E-01	120.0	7.08093E-06	4.24856E-05
9.55142E-01	120.0	8.48869E-05	4.71568E-05
9.43608E-01	120.0	1.63683E-05	4.36450E-05
9.28720E-01	120.0	6.49624E-05	3.24812E-05
1.36282E+00	135.0	8.96205E-02	4.16304E-03
1.35679E+00	135.0	6.96570E-02	3.82184E-03
1.34650E+00	135.0	1.97081E-02	3.21605E-03
1.34225E+00	135.0	2.31158E-02	2.96043E-03
1.33799E+00	135.0	2.42144E-02	2.95461E-03
1.33799E+00	135.0	1.81630E-02	3.21010E-03
1.33364E+00	135.0	3.44924E-02	3.49443E-03
1.32939E+00	135.0	4.54927E-02	4.28910E-03
1.32513E+00	135.0	5.36329E-02	4.54789E-03
1.32098E+00	135.0	7.84287E-02	5.63288E-03
1.31672E+00	135.0	6.62315E-02	5.09177E-03
1.31247E+00	135.0	3.10225E-02	3.74545E-03
1.30822E+00	135.0	1.47570E-02	2.42299E-03
1.30574E+00	135.0	1.09245E-02	1.98597E-03
1.29645E+00	135.0	4.37684E-03	3.96306E-04

TABLE A.7

Continued

$E_{lab}(MeV)$	θ_{lab}	$Yield$	$dYield$
1.29308E+00	135.0	3.25699E-03	3.32970E-04
1.28804E+00	135.0	3.79329E-03	3.54347E-04
1.28299E+00	135.0	3.61905E-03	3.38424E-04
1.27805E+00	135.0	3.27360E-03	3.28279E-04
1.27300E+00	135.0	3.64463E-03	3.11335E-04
1.26806E+00	135.0	4.01361E-03	3.08373E-04
1.26301E+00	135.0	3.97800E-03	2.62082E-04
1.25806E+00	135.0	5.53763E-03	3.21149E-04
1.25688E+00	135.0	5.21007E-03	4.82593E-04
1.25312E+00	135.0	5.45150E-03	3.22548E-04
1.25193E+00	135.0	5.46893E-03	4.02508E-04
1.24817E+00	135.0	4.09530E-03	2.34578E-04
1.24649E+00	135.0	3.56117E-03	3.51525E-04
1.24323E+00	135.0	2.62518E-03	1.81081E-04
1.24194E+00	135.0	2.40763E-03	2.28236E-04
1.23749E+00	135.0	1.27442E-03	1.71537E-04
1.23422E+00	135.0	1.74764E-03	2.65901E-04
1.22433E+00	135.0	2.44610E-03	3.17158E-04
1.21454E+00	135.0	2.00984E-03	2.24011E-04
1.20455E+00	135.0	2.03103E-03	2.39303E-04
1.19515E+00	135.0	1.56978E-03	1.81251E-04

TABLE A.7

Continued

$E_{lab}(MeV)$	θ_{lab}	$Yield$	$dYield$
1.18536E+00	135.0	1.81665E-03	1.85334E-04
1.17537E+00	135.0	2.48282E-03	1.83774E-04
1.16607E+00	135.0	2.53708E-03	2.08632E-04
1.15717E+00	135.0	2.88511E-03	2.35842E-04
1.14718E+00	135.0	3.66236E-03	1.87407E-04
1.14688E+00	135.0	3.30958E-03	1.77644E-04
1.13620E+00	135.0	4.21133E-03	1.90992E-04
1.12739E+00	135.0	4.53257E-03	2.14056E-04
1.12719E+00	135.0	4.40972E-03	2.31437E-04
1.11740E+00	135.0	3.46251E-03	2.29197E-04
1.11117E+00	135.0	1.78441E-03	1.27422E-04
1.10800E+00	135.0	2.51369E-03	2.05907E-04
1.10652E+00	135.0	1.57734E-03	1.11704E-04
1.10187E+00	135.0	1.23690E-03	1.23025E-04
1.09722E+00	135.0	9.40837E-04	1.12052E-04
1.09257E+00	135.0	7.51397E-04	1.06237E-04
1.08763E+00	135.0	5.91980E-04	9.84137E-05
1.08308E+00	135.0	4.92783E-04	1.09932E-04
1.07872E+00	135.0	5.18129E-04	1.01796E-04
1.07417E+00	135.0	2.63409E-04	1.08291E-04
1.07111E+00	135.0	2.20501E-04	8.47761E-05

202

TABLE A.7

Continued

$E_{lab}(MeV)$	θ_{lab}	$Yield$	$dYield$
1.06646E+00	135.0	1.11445E-04	1.01887E-04
1.04826E+00	135.0	1.27169E-04	4.49747E-05
1.04380E+00	135.0	1.07988E-04	4.84202E-05
1.03025E+00	135.0	7.67840E-05	3.25740E-05
1.02550E+00	135.0	6.83843E-05	2.27975E-05
1.01235E+00	135.0	1.10406E-04	4.13980E-05
1.00344E+00	135.0	1.43409E-04	4.41265E-05
9.94641E-01	135.0	1.28687E-04	3.43166E-05
9.85837E-01	135.0	1.51505E-04	3.19023E-05
9.68328E-01	135.0	5.57765E-05	1.24519E-05
9.59623E-01	135.0	1.48788E-05	1.31546E-05
9.50819E-01	135.0	1.48531E-05	1.05679E-05
9.43499E-01	135.0	5.08745E-05	3.39108E-05
9.30936E-01	135.0	4.11809E-05	1.14299E-05
9.19560E-01	135.0	4.81782E-05	1.73726E-05
9.05514E-01	135.0	4.55882E-05	1.51988E-05
8.91566E-01	135.0	3.59496E-05	1.54105E-05
8.52987E-01	135.0	1.91825E-05	1.03100E-05
7.89283E-01	135.0	9.71778E-06	2.59141E-05
1.35948E+00	150.0	7.99514E-02	8.80814E-03
1.35431E+00	150.0	2.46095E-02	7.51902E-03

TABLE A.7

Continued

$E_{lab}(MeV)$	θ_{lab}	$Yield$	$dYield$
1.34915E+00	150.0	8.23698E-03	6.17705E-03
1.33886E+00	150.0	1.39964E-03	6.29975E-03
1.33373E+00	150.0	1.51873E-02	6.21097E-03
1.32860E+00	150.0	5.47658E-02	7.11241E-03
1.32349E+00	150.0	6.81125E-02	9.22323E-03
1.31840E+00	150.0	4.78221E-02	8.56675E-03
1.31330E+00	150.0	3.76439E-02	5.71874E-03
1.30822E+00	150.0	4.85642E-03	4.85642E-03
1.29809E+00	150.0	2.48515E-03	1.29684E-03
1.29303E+00	150.0	1.54358E-03	8.81927E-04
1.28799E+00	150.0	4.69365E-04	9.38729E-04
1.28295E+00	150.0	2.74752E-03	8.16977E-04
1.27793E+00	150.0	6.68921E-05	7.35772E-04
1.26792E+00	150.0	1.76214E-03	6.32531E-04
1.26259E+00	150.0	3.55551E-03	6.14395E-04
1.25761E+00	150.0	2.70462E-03	6.05555E-04
1.25263E+00	150.0	5.47462E-03	5.43895E-04
1.24800E+00	150.0	3.70878E-03	4.23958E-04
1.24322E+00	150.0	2.87810E-03	3.98105E-04
1.23810E+00	150.0	5.80815E-04	3.16808E-04
1.23301E+00	150.0	5.01037E-04	2.75611E-04

$E_{lab}(MeV)$	θ_{lab}	$Yield$	$dYield$
1.22791E+00	150.0	2.95218E-04	2.41493E-04
1.22317E+00	150.0	3.08651E-04	3.39489E-04
1.21793E+00	150.0	4.56963E-04	2.51296E-04
1.21353E+00	150.0	1.28433E-04	2.56921E-04
1.20864E+00	150.0	3.91201E-04	2.38146E-04
1.20377E+00	150.0	3.19573E-04	2.35468E-04
1.19890E+00	150.0	9.85270E-04	1.97081E-04
1.19405E+00	150.0	1.02802E-03	2.05550E-04
1.18921E+00	150.0	1.07197E-03	2.14420E-04
1.18437E+00	150.0	1.41881E-03	2.06933E-04
1.17472E+00	150.0	7.94561E-04	2.06545E-04
1.16992E+00	150.0	1.78232E-03	1.94647E-04
1.16512E+00	150.0	1.01727E-03	2.42207E-04
1.16033E+00	150.0	1.50087E-03	2.66107E-04
1.15556E+00	150.0	1.22953E-03	2.29683E-04
1.15080E+00	150.0	1.51231E-03	2.33757E-04
1.14604E+00	150.0	2.43753E-03	1.70846E-04
1.14129E+00	150.0	2.89325E-03	1.21035E-04
1.13655E+00	150.0	2.32089E-03	1.47071E-04
1.13057E+00	150.0	2.64326E-03	1.55124E-04
1.12569E+00	150.0	2.72191E-03	1.70529E-04

TABLE A.7

Continued

$E_{lab}(MeV)$	θ_{lab}	$Yield$	$dYield$
1.12083E+00	150.0	1.23930E-03	1.91176E-04
1.11613E+00	150.0	2.67105E-03	1.85539E-04
1.11146E+00	150.0	1.23788E-03	1.74440E-04
1.10678E+00	150.0	1.41677E-03	1.66679E-04
1.10212E+00	150.0	4.47086E-04	1.86263E-04
1.09746E+00	150.0	2.30753E-04	1.73133E-04
1.09234E+00	150.0	8.09533E-04	1.64091E-04
1.08818E+00	150.0	9.04436E-04	1.70375E-04
1.08355E+00	150.0	7.72334E-05	1.80152E-04
1.06499E+00	150.0	5.96062E-04	1.41205E-04
1.06057E+00	150.0	1.22942E-04	1.53695E-04
1.05600E+00	150.0	2.57126E-04	1.00013E-04
1.04236E+00	150.0	2.55306E-05	5.95667E-05
1.02731E+00	150.0	1.32117E-04	5.08091E-05
1.02281E+00	150.0	1.50481E-04	7.02515E-05
9.87222E-01	150.0	6.16264E-05	6.16264E-05
9.78418E-01	150.0	2.25242E-05	5.25428E-05
9.66745E-01	150.0	6.72692E-05	6.72692E-05
9.55142E-01	150.0	8.96416E-05	6.72346E-05
9.43608E-01	150.0	7.13897E-05	5.19223E-05
9.28720E-01	150.0	1.98926E-04	4.97247E-05
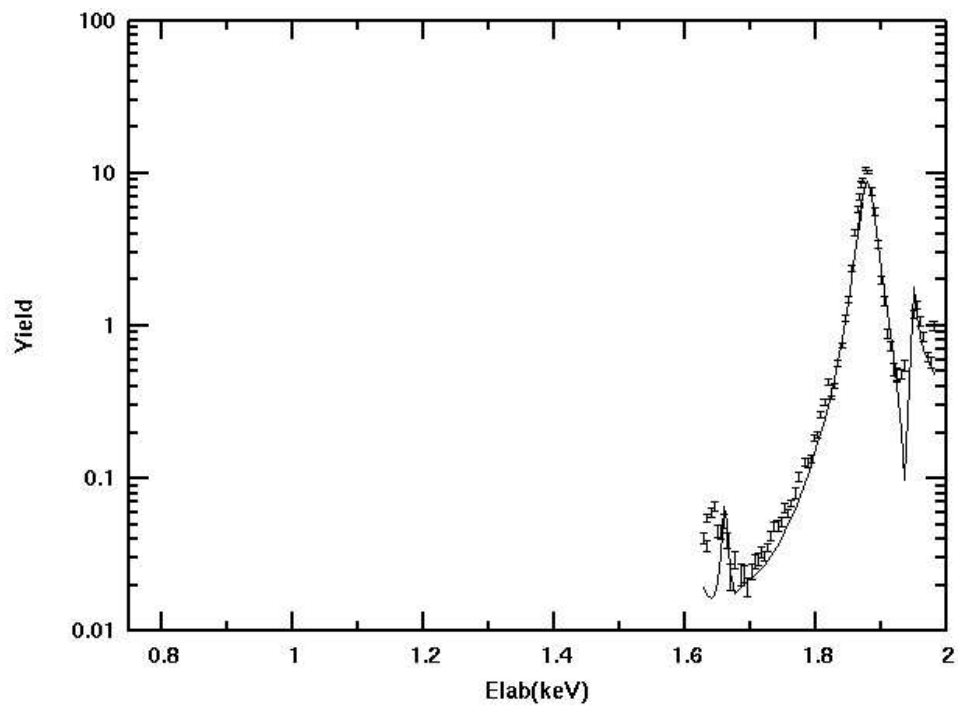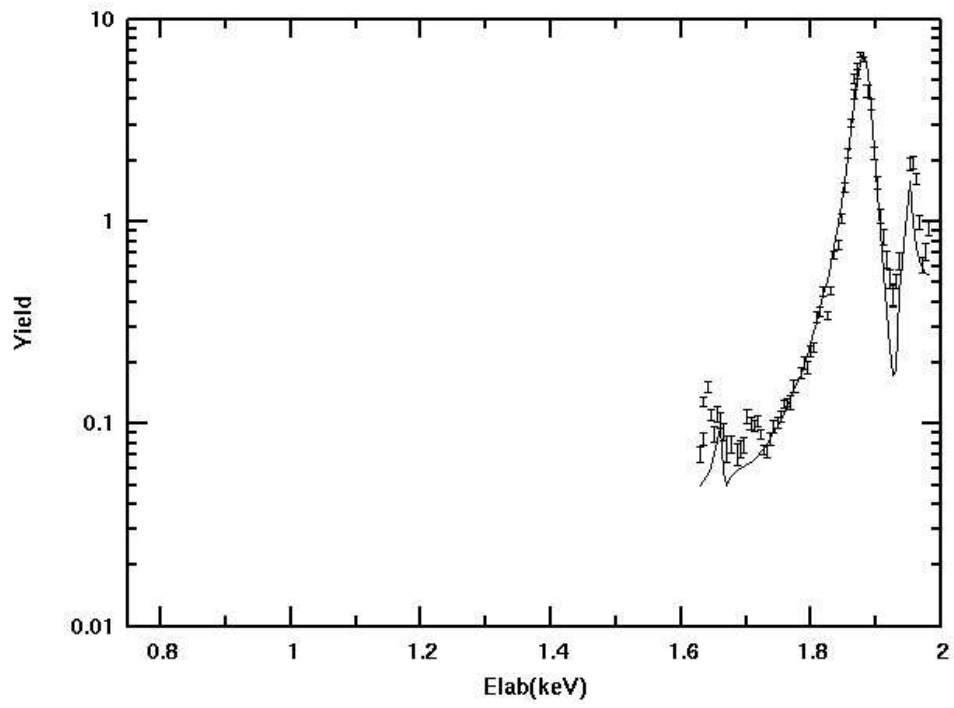
Figure A.1. Yield curves 1 and 2
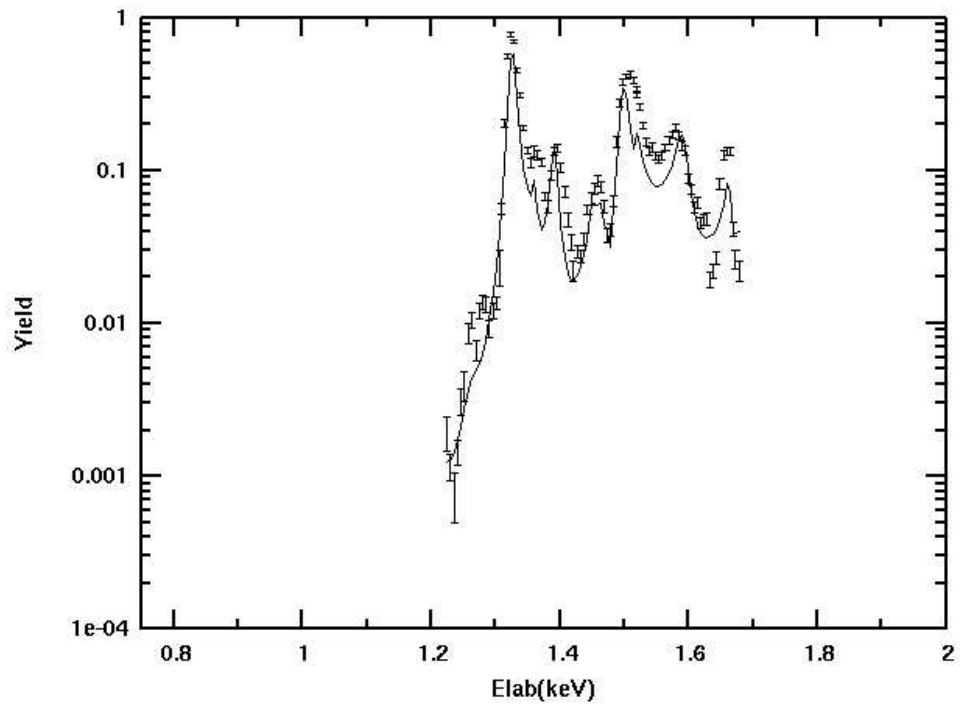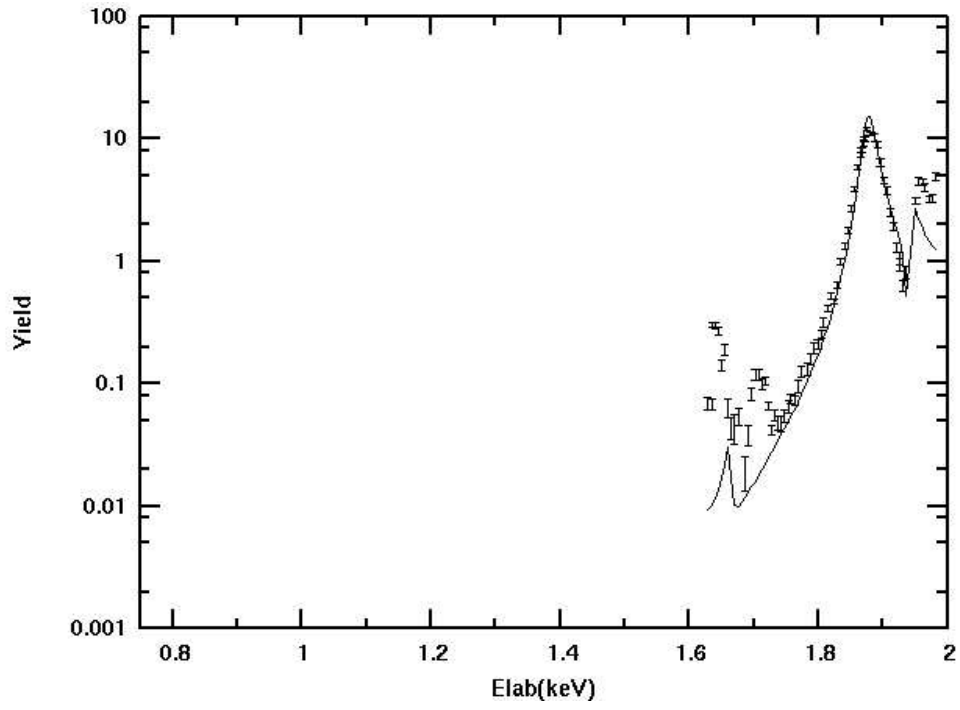
Figure A.2. Yield curves 3 and 4
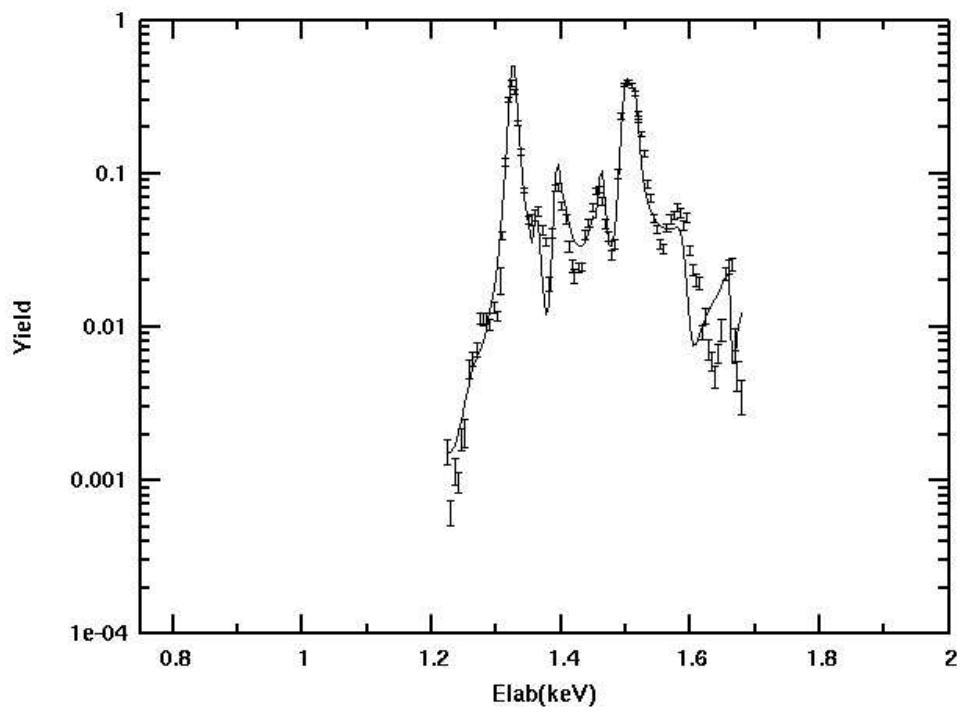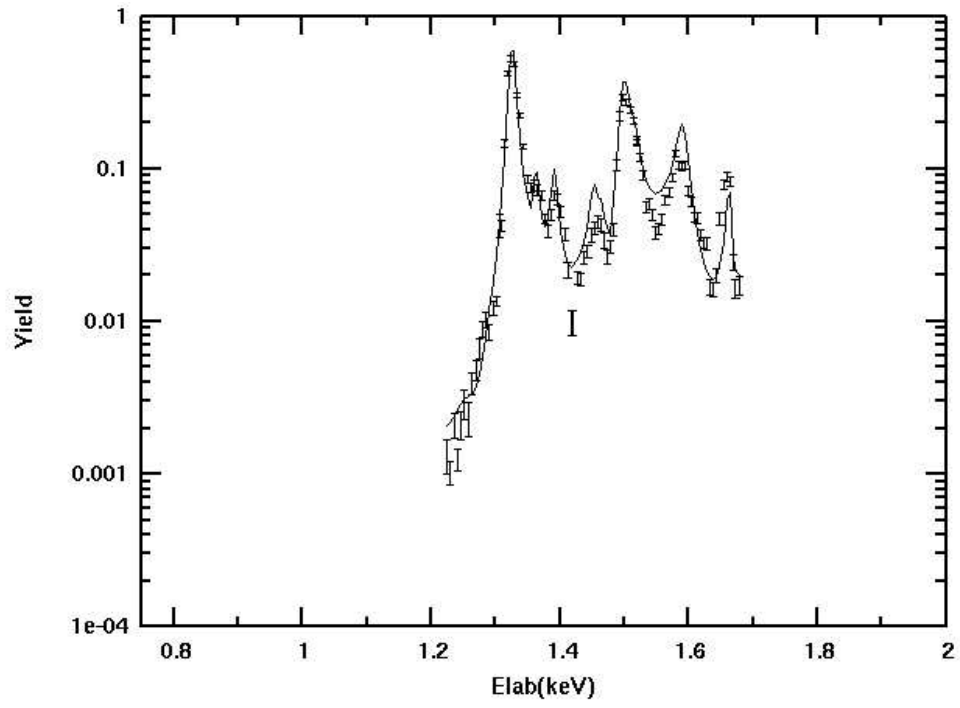
Figure A.3. Yield curves 5 and 6

209
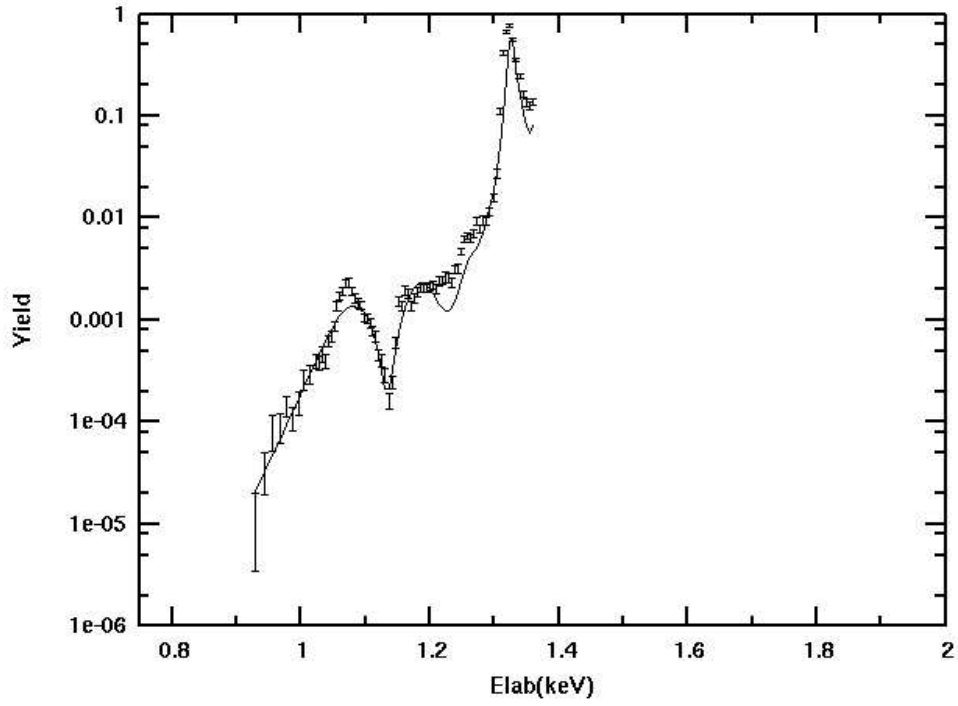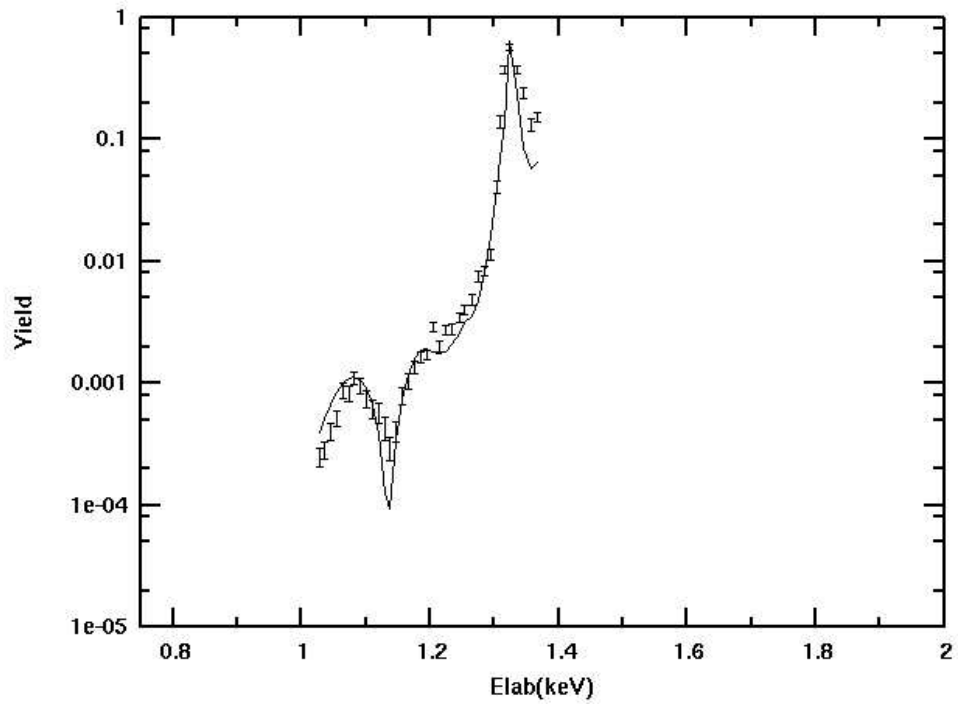
Figure A.4. Yield curves 7 and 8
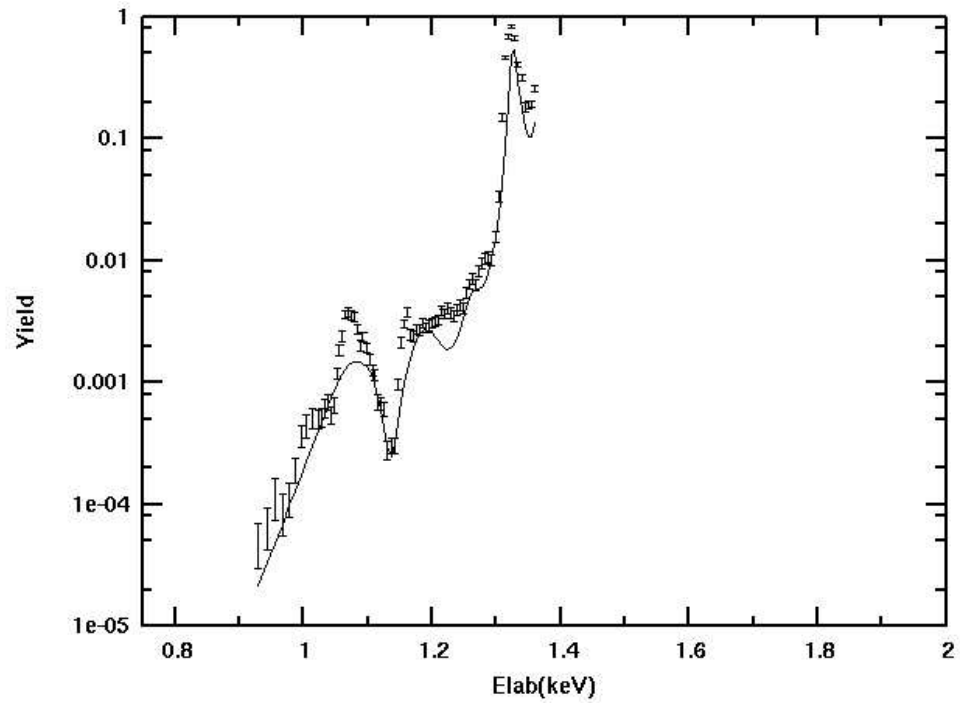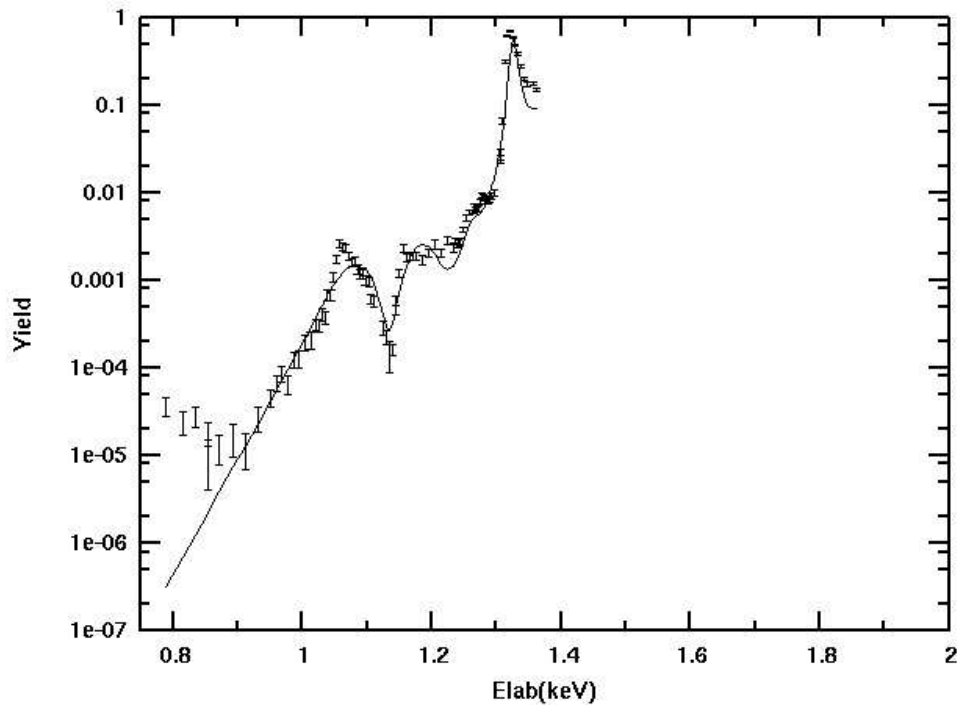
Figure A.5. Yield curves 9 and 10

211
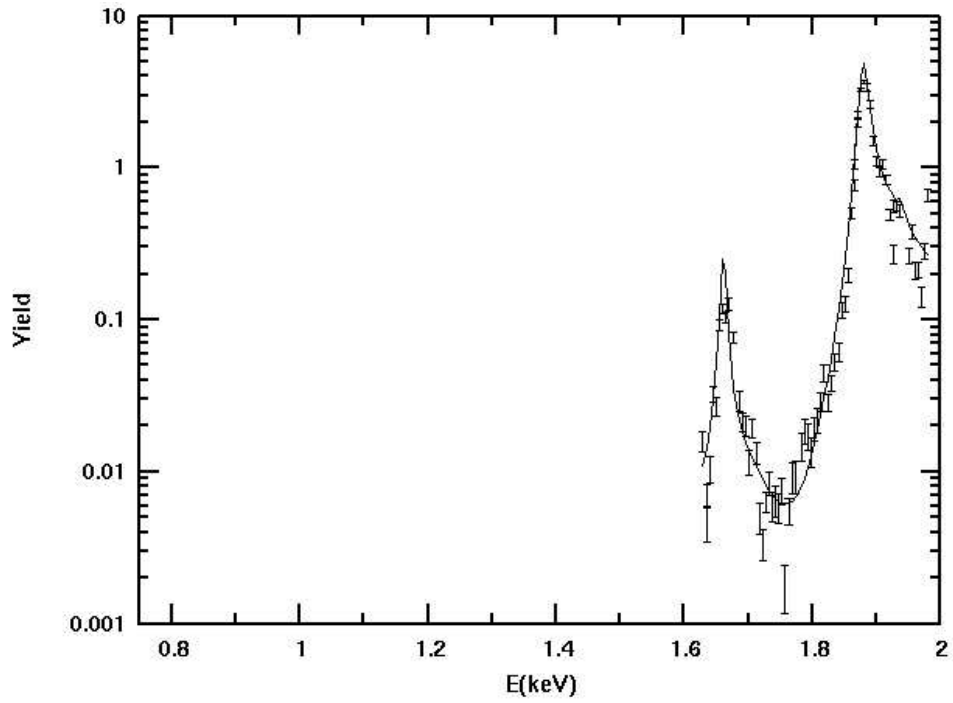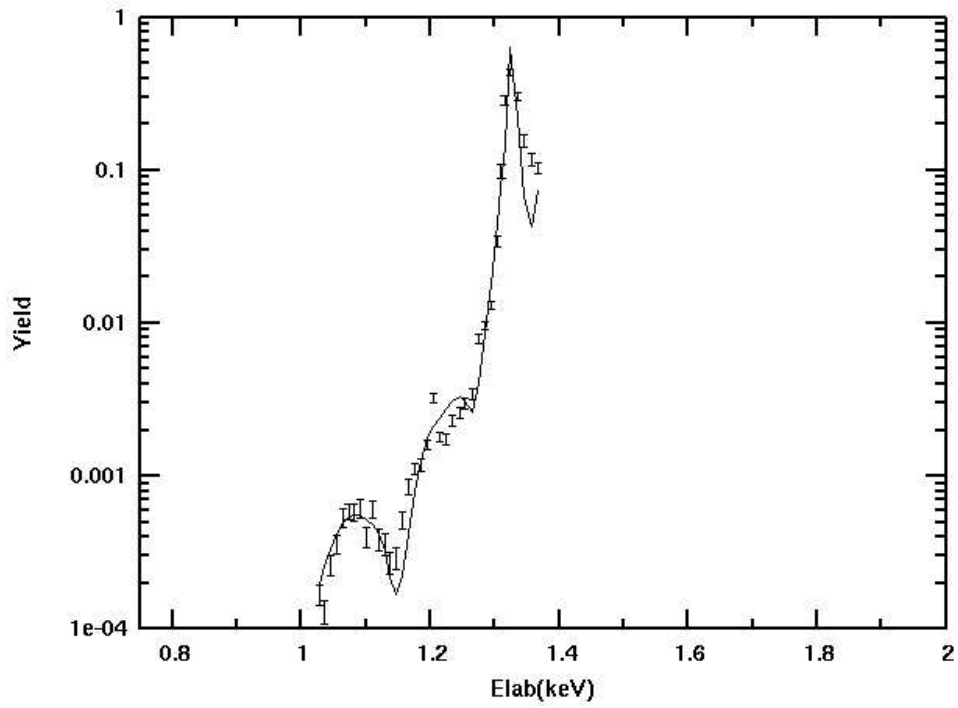
Figure A.6. Yield curves 11 and 12

212
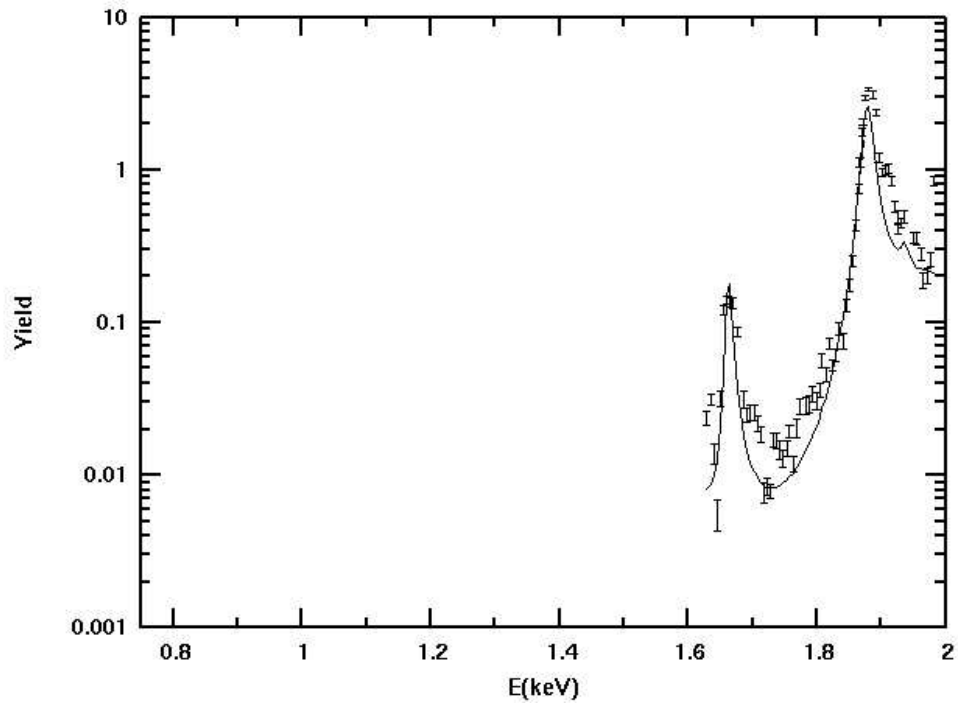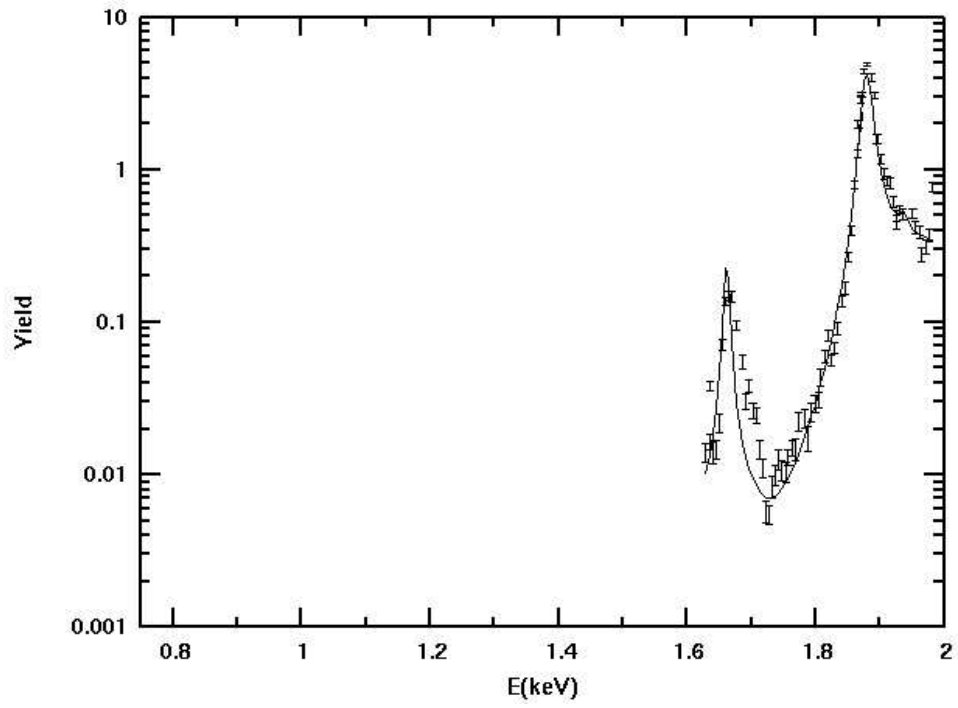
Figure A.7. Yield curves 13 and 14

213
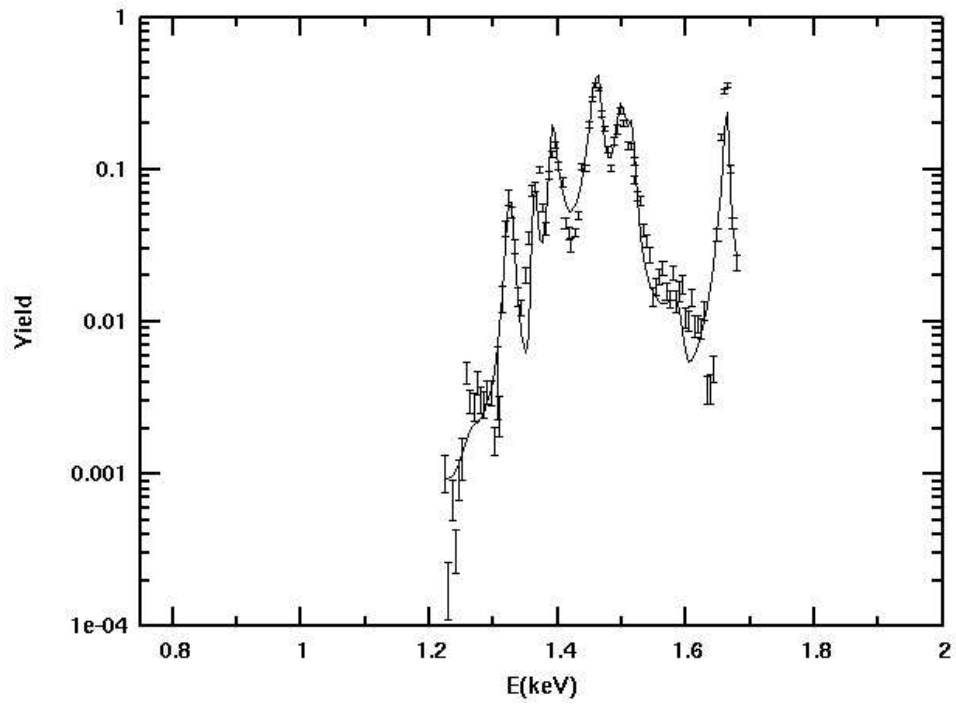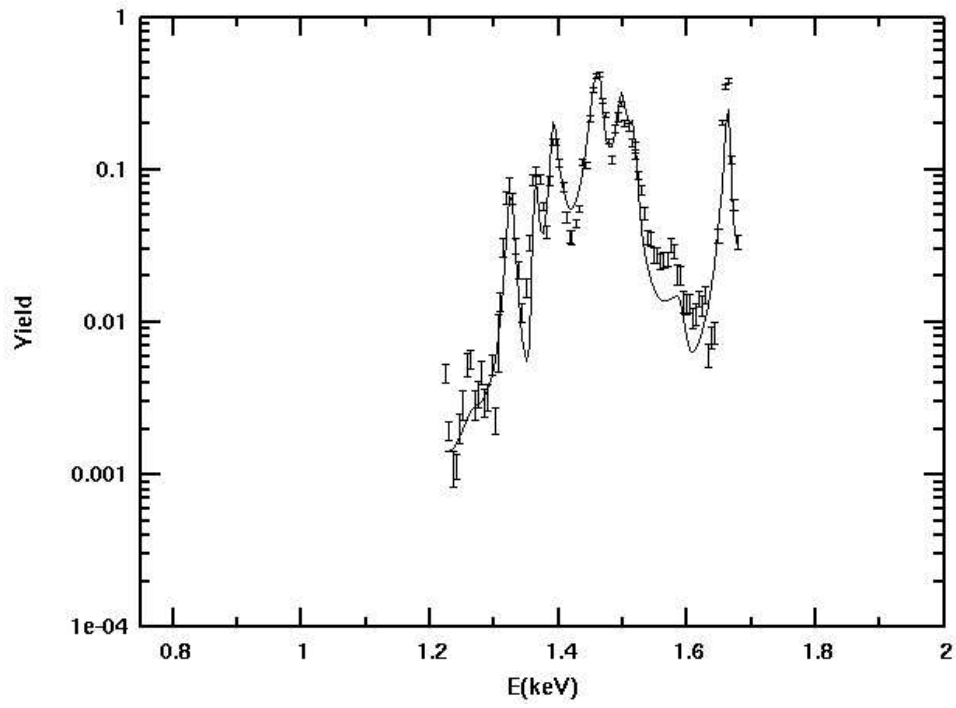
Figure A.8. Yield curves 15 and 16

214
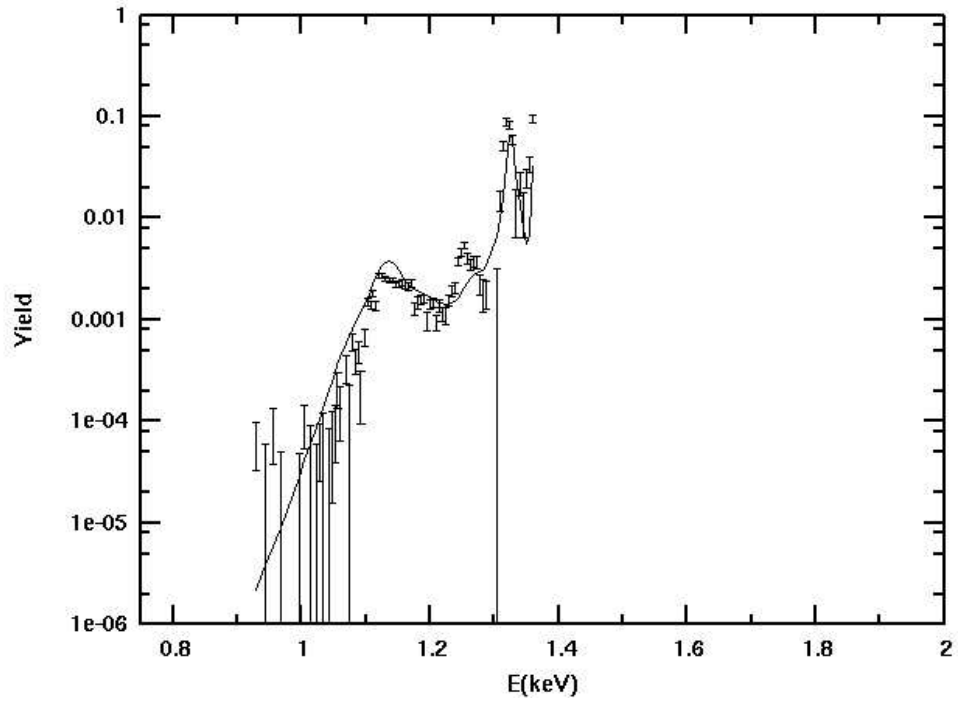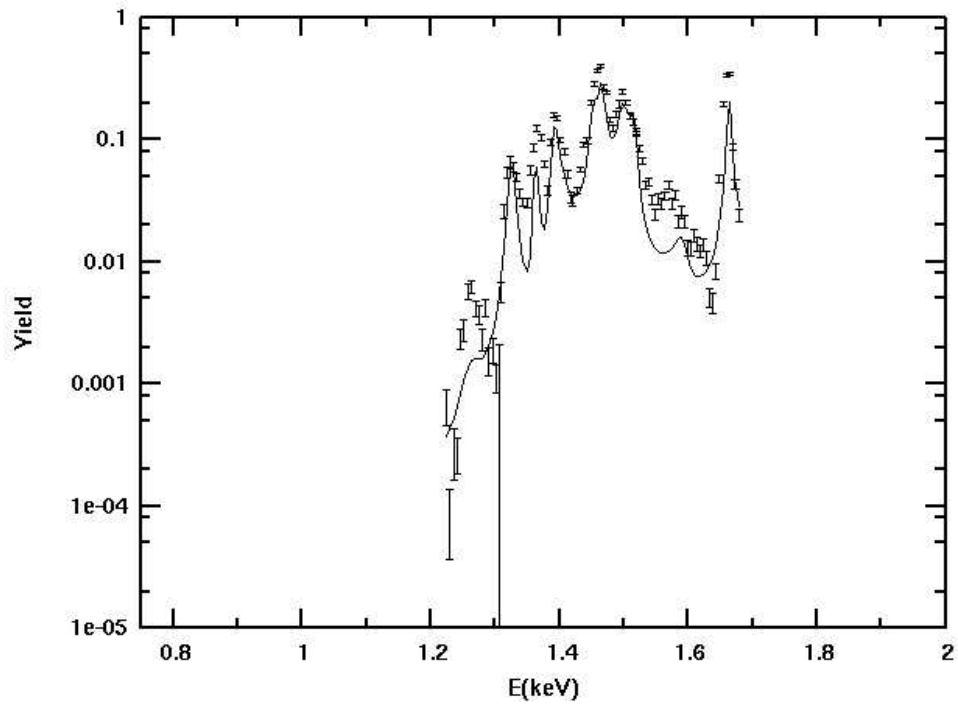
Figure A.9. Yield curves 17 and 18

215
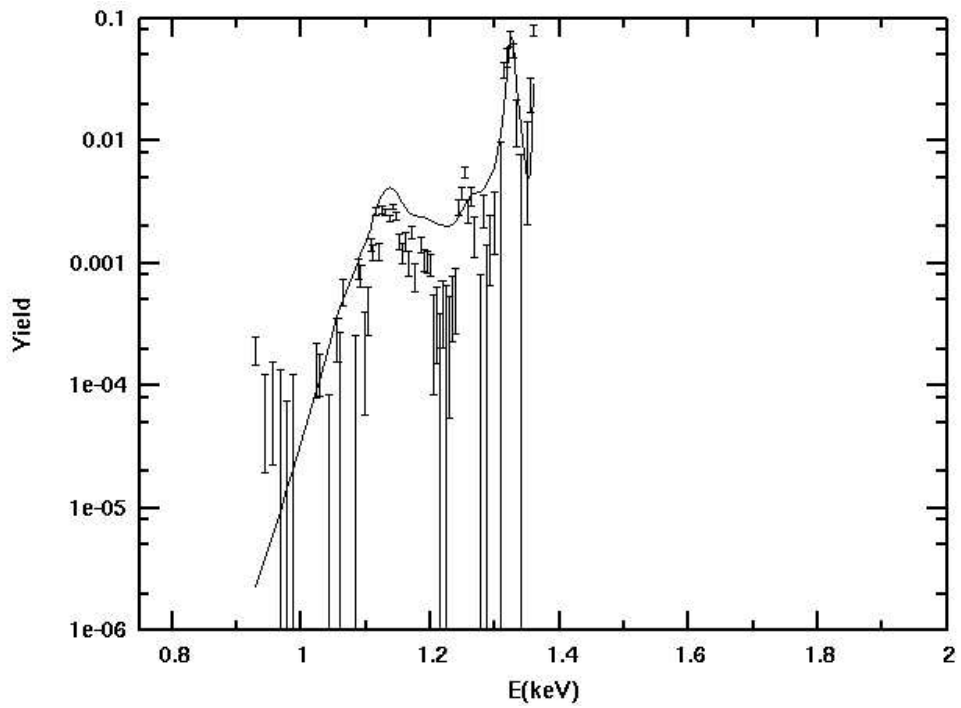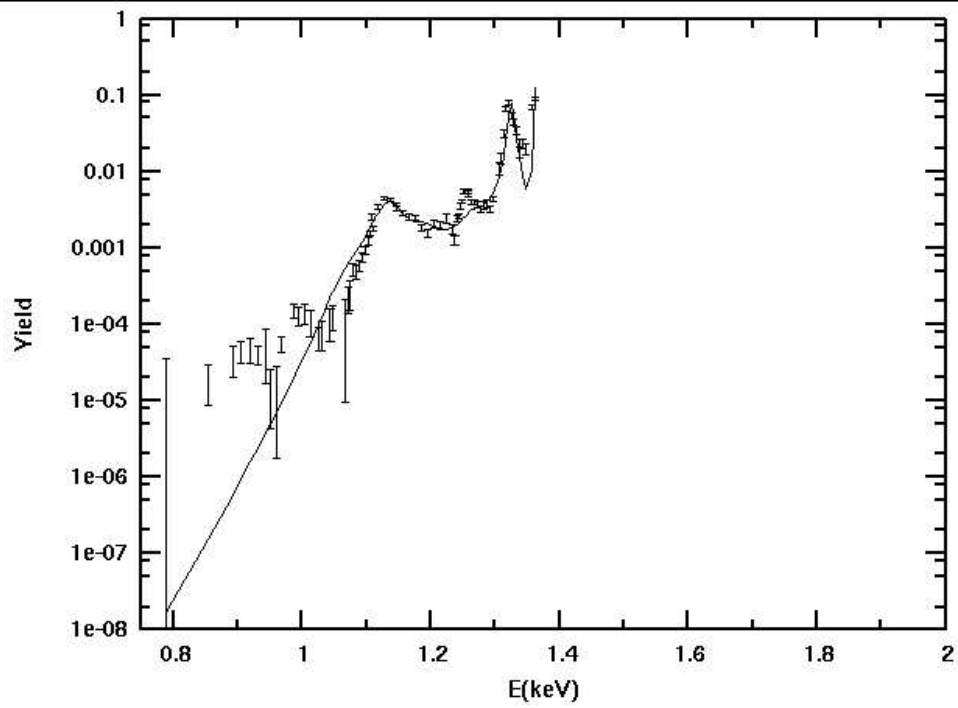
Figure A.10. Yield curves 19 and 20

216

BIBLIOGRAPHY

1. M. Abramowitz and I. A. Stegun, *Handbook of mathematical functions*. Dover Publications, Inc, (1965).

2. A. Alibés, J. Labay and R. Canal, Galactic chemical abundance evolution in the solar neighborhood up to the iron peak. *Astron. Astrophys.*, 370: 1103–1121 (2001).

3. E. Anders and N. Grevesse, Abundances of the elements: Meteoritic and solar. *Geochim. Cosmochim. Acta*, 53: 197–214 (1989).

4. C. Angulo and P. Descouvemont, R-matrix analysis of interference effects in $^{12}C(\alpha,\alpha)^{12}C$ and $^{12}C(\alpha,\gamma)^{16}O$. *Phys. Rev. C*, 61: 064611 (2000).

5. C. Angulo et al., A compilation of charged-particle induced thermonuclear reaction rates. *Nucl. Phys. A*, 656: 3 (1999).

6. G. T. J. Arnison, The production of nuclear targets by vacuum evaporation. *United Kingdom Atomic Energy Authority*, AWRE Report 0-32/67: 1–23 (1967).

7. R. Azuma, AZURE. *private communication* (2005).

8. J. Blatt and L. Biedenharn, The angular distribution of scattering and reaction cross sections. *Rev. Mod. Phys.*, 24: 258 (1952).

9. N. Bohr, Neutron capture and neutron constitution. *Nature*, 137: 344–348 (1936).

10. E. Brady and M. Deutsch, Angular correlation of successive gamma-rays. *Phys. Rev.*, 78: 558–566 (1950).

11. C. R. Brune, Alternative parametrization of R-matrix theory. *Phys. Rev. C*, 66: 044611 (2002).

12. C. R. Brune, Formal and physical R-matrix parameters. *arXiv:nucl-th/0502087* (2005).

13. L. Buchmann, J. d'Auria and P. McCorquodale, Stellar reaction rates of alpha capture on light (N$\neq$Z) nuclei and their astrophysical implications. *Ap. J.*, 324: 953–965 (1988).

14. M. Busso, R. Gallino and G. Wasserburg, Nucleosynthesis in asymptotic giant branch stars: relevance for galactic enrichment and solar system formation. *Annu. Rev. Astron. Astrophys.*, 37: 239–309 (1999).

15. G. R. Caughlan and W. A. Fowler, Thermonuclear Reaction Rates V. *Atom. Data Nucl. Data*, 40: 283–334 (1988).

16. G. R. Caughlan, W. A. Fowler, M. J. Harris and B. A. Zimmerman, Thermonuclear Reaction Rates for low-mass nuclei ($1 \leq Z \leq 14$). *Atom. Data Nucl. Data*, 32: 197–233 (1985).

17. J. Cseh, E. Koltay, Z. Máté, E. Somorjai and L. Zolnai, Levels in ^{23}Na excited by the ^{19}F$(\alpha, \alpha)^{19}$F, ^{19}F$(\alpha, \gamma)^{23}$Na and ^{19}F$(\alpha, p)^{22}$Ne reactions. *Nucl. Phys. A*, 413: 311–322 (1984).

18. K. Cunha, V. V. Smith, D. L. Lambert and K. H. Hinkle, Fluorine abundances in the Large Magellanic Cloud and ω Centauri: Evidence for neutrino nucleosynthesis? *astro-ph/0305303* (2003).

19. A. Cunsolo, A. Foti, G. Immè, G. Pappalardo, G. Raciti and N. Saunier, ^{18}O states via the $^{14}C(^{6}Li, d)^{18}O$ reaction at 34 MeV incident energy. *Phys. Rev. C*, 24: 476–487 (1981).

20. S. Dababneh, M. Heil, F. Käppeler, J. Görres, M. Wiescher, R. Reifarth and H. Leiste, Stellar He burning of ^{18}O: A measurement of low-energy resonances and their astrophysical implications. *Phys. Rev. C*, 68: 025801 (2003).

21. C. de Jager, H. Nieuwenhuijzen and K. van der Hucht, Mass loss rates in the Hertzsprung-Russell diagram. *Astron. Astrophys.*, 72: 259–289 (1988).

22. F. de Oliveira, Determination of α-widths in ^{19}F relevant to fluorine nucleosynthesis. *Nucl. Phys. A*, 597: 231–252 (1996).

23. F. de Oliveira, Comparison of low-energy resonances in $^{15}N(\alpha, \gamma)^{19}F$ and $^{15}O(\alpha, \gamma)^{19}Ne$ and related uncertainties. *Phys. Rev. C*, 55: 3149–3151 (1997).

24. P. A. Denissenkov and C. A. Tout, Partial mixing and formation of the ^{13}C pocket by internal gravity waves in asymptotic giant branch stars. *Mon. Not. R. Astron. Soc.*, 340: 722–732 (2003).

25. A. Denker et al. AIP, New York (1995).

26. P. Descouvemont and D. Baye, Multiconfiguration microscopic study of $\alpha + {}^{14}C$ molecular states. *Phys. Rev. C*, 31: 2274–2284 (1985).

27. H. W. Drotleff, A. Denker, H. Knee, M. Soiné, G. Wolf, J. Hammer, U. Greife, C. Rolfs and H. Trautvetter, Reaction rates of the s-process neutron sources ${}^{13}C(\alpha, n){}^{16}O$ and ${}^{22}Ne(\alpha, n){}^{25}Mg$. *Ap. J.*, 414: 735–739 (1993).

28. P. P. Eggleton, The evolution of low mass stars. *Mon. Not. R. Astron. Soc.*, 151: 351–364 (1971).

29. P. Endt, Energy levels of $A = 21 - 44$ nuclei (VII). *Nucl. Phys. A*, 521: 1–400 (1990).

30. M. Forestini, S. Goriely, A. Jorrisen and M. Arnould, Flourine production in thermal pulses on the asymptotic giant branch. *Astron. Astrophys.*, 261: 157–163 (1992).

31. H. Fortune and A. Lacaze, Reliability of α strengths for weak states. *Phys. Rev. C*, 67: 064305 (2003).

32. W. A. Fowler and F. Hoyle, Neutrino processes and pair formation in massive stars and supernovae. *Ap. J. Suppl.*, 9: 201–319 (1964).

33. W. A. Fowler, C. G. R. and B. Zimmerman, Thermonuclear Reaction Rates, II. *Annu. Rev. Astron. Astrophys.*, 13: 69–112 (1975).

34. C. Funck and K. Langanke, The ${}^{14}C(\alpha, \gamma){}^{18}O$ reaction at astrophysical energies. *Ap. J.*, 344: 46–50 (1989).

35. G. Gamow. *Z. Phys*, 51: 204 (1928).

36. U. Giesen, C. Browne, J. Görres, J. Ross, M. Wiescher, R. Azuma, J. King, J. Vise and M. Buckby, The influence of low-energy resonances on the reaction rate of ${}^{18}O(\alpha, \gamma){}^{22}Ne$. *Nucl. Phys. A*, 567: 146–164 (1994).

37. G. Gilmore and J. Hemingway, *Practical gamma-ray spectrometry*. John Wiley and Sons Ltd. (1995).

38. S. Goriely, *MOST: An updated HF model of nuclear reactions*. Editions Frontires, Gif-sur-Yvette 1998 (1998).

39. S. Goriely, A. Jorrisen and M. Arnould, *On the mechanisms of ${}^{19}F$ production*. Max-Planck-Institut für Physik und Astrophysik Rep. (1989).

40. J. Görres. *private communication* (1999).

41. J. Görres, C. Arlandini, U. Giesen, M. Heil, F. Käppeler, H. Leiste, E. Stech and M. Wiescher, Low-energy resonances in $^{14}N(\alpha,\gamma)^{18}F$ and their astrophysical implications. *Phys. Rev. C*, 62: 55801 (2000).

42. J. Görres, S. Dababneb, A. Couture, M. Heil, F. Käppeler, H. Leiste, M. Lugaro, C. Ugalde and M. Wiescher, Nucleosynthesis in TP-AGB stars and the production of fluorine. *Nucl. Phys. A*, 718: 155c–158c (2003).

43. J. Görres, S. Graff, M. Wiescher, R. Azuma, C. Barnes and T. Wang, Alpha capture on ^{14}C and its astrophysical implications. *Nucl. Phys. A*, 548: 414–426 (1992).

44. M. J. Harris, Notes to "Thermonuclear Reaction Rates, III". *private communication, W. Fowler-M. Wiescher* (1983).

45. M. J. Harris, W. Fowler, G. Caughlan and B. Zimmerman, Thermonuclear Reaction Rates, III. *Annu. Rev. Astron. Astrophys.*, 21: 165–176 (1983).

46. W. C. Haxton, Neutrino heating in supernovae. *Phys. Rev. Lett.*, 60(20): 1999–2002 (1988).

47. A. Heger, E. Kolbe, W. C. Haxton, K. Langanke, G. Martínez-Pinedo and S. Woosley, Neutrino nucleosynthesis. *arXiv:astro-ph/0307546* (2004).

48. M. Heil, Forschungszentrum Karlsruhe report 6783. (2002).

49. M. Heil et al., A measurement of the $^{13}C(\alpha,\alpha)^{13}C$ differential cross section and its application to the $^{13}C(\alpha,n)^{16}O$ reaction. *Nucl. Phys. A*, 688: 499c–501c (2001).

50. F. Herwig, *Private communication* (2005).

51. F. Herwig and S. M. Austin, Nuclear reaction rates and carbon star formation. *Ap. J.*, 613: L73–L76 (2004).

52. F. Herwig, T. Blöker, D. Schönberner and M. El Eid, Stellar evolution of low and intermediate-mass stars. IV. Hydrodynamically-based overshoot and nucleosynthesis in AGB stars. *Astron. Astrophys.*, 324: L81–L84 (1997).

53. C. Huan-sheng, S. Hao, Y. Fujia and T. Jia-yong, Cross sections for non-Rutherford backscattering of ^{4}He from five light elements. *Nucl. Instr. and Meth. B*, 85: 47–50 (1994).

54. I. Iben Jr. and A. Renzini, On the formation of carbon star characteristics and the production of neutron-rich isotopes in asymptotic giant branch stars of small core mass. *Ap. J.*, 263: L23–L27 (1982).

55. A. Jorrisen and S. Goriely, The Nuclear Network Generator: A tool for nuclear astrophysics. *Nucl. Phys. A*, 688: 508–510 (2001).

56. A. Jorrisen, V. V. Smith and D. L. Lambert, Flourine in red giant stars: evidence for nucleosynthesis. *Astron. Astrophys.*, 261: 164–187 (1992).

57. F. Käppeler, M. Wiescher, U. Giesen, J. Görres, I. Baraffe, C. M. El Eid, M.and Raiteri, M. Busso, R. Gallino, M. Limongi and A. Chieffi, Reaction rates for $^{18}O(\alpha, \gamma)^{22}Ne, ^{22}Ne(\alpha, \gamma)^{26}Mg$, and $^{22}Ne(\alpha, n)^{25}Mg$ in stellar helium burning and s-process nucleosynthesis in massive stars. *Ap. J.*, 437: 396–409 (1994).

58. A. I. Karakas, *Asymptotic Giant Branch Stars: their influence on binary systems and the interstellar medium*. Ph.D. thesis, Monash University (2003).

59. A. I. Karakas et al., to be published. *Ap. J.* (2005).

60. N. Keeley and D. T. Kemper, K. W.and Khoa, DWBA analysis of the $^{13}C(^{6}Li, d)^{17}O$ reaction at 10 MeV/nucleon and its astrophysical implications. *Nucl. Phys. A*, 726: 159–172 (2003).

61. G. Keyworth, P. Wilhjelm, J. G.C. Kyker, H. Newson and E. Bilpuch, High-resolution study of isobaric analog resonances in ^{23}Na. *Phys. Rev.*, 176(4): 1302–1310 (1968).

62. R. Kippenhahn and A. Weigert, *Stellar Structure and Evolution*. Springer-Verlag Berlin Heidelberg. (1990).

63. K. Krane, *Introductory Nuclear Physics*. John Wiley and Sons Inc. (1988).

64. S. Kubono et al., Determination of the subthreshold state contribution in $^{13}C(\alpha, n)^{16}O$, the main neutron-source reaction for the s process. *Phys. Rev. Lett.*, 90: 062501 (2003).

65. J. Kuperus, Interfering resonances in the $^{19}F(\alpha, p)^{22}Ne$ reaction. *Physica*, 31: 1603–1616 (1965).

66. A. Lane and R. Thomas, R-matrix Theory of Nuclear Reactions. *Rev. Mod. Phys.*, 30(2): 257–353 (1958).

67. N. Langer, Mass-dependent mass loss rates of Wolf-Rayet stars. *Astron. Astrophys.*, 220: 135–143 (1989).

68. N. Langer, A. Heger, S. Wellstein and F. Herwig, Mixing and nucleosynthesis in rotating TP-AGB stars. *Astron. Astrophys.*, 346: L37–L40 (1999).

69. H. Lorenz-Wirzba, *Unterschung von (p,α)-Reactionen unterhalb der Coulombbarriere*. Ph.D. thesis, Universität Münster (1978).

70. M. Lugaro, *Nucleosynthesis in AGB stars*. Ph.D. thesis, Monash University (2001).

71. M. Lugaro, C. Ugalde, A. I. Karakas, M. Wiescher, J. Görres, J. C. Lattanzio and R. C. Cannon, Reaction rates uncertainties and the production of ^{19}F in AGB stars. *Ap. J.*, 615: 934–946 (2004).

72. J. Marion and F. Young, *Nuclear Reaction Analysis: Graphs and Tables*. John Wiley and Sons Inc. (1968).

73. L. A. Marschall, *The Supernova Story*. Plenum Press (1988).

74. G. Meynet and M. Arnould, *Synthesis of ^{19}F in the He-Burning Zones of Massive Stars*. IOP, Bristol (1993).

75. G. Meynet and M. Arnould, Synthesis of ^{19}F in Wolf-Rayet stars. *Astron. Astrophys.*, 355: 176–180 (2000).

76. G. Meynet, A. Maeder, G. Schaller, D. Schaerer and C. Charbonnel, Grids of massive stars with high mass loss rates. V. from 12 to 120 $M_\odot$ at z = 0.001, 0.004, 0.008, 0.020, and 0.040. *Astron. Astrophys. Sup.*, 103: 97–105 (1994).

77. K. Michaelian. *private communication* (1996).

78. Z. Michalewicz, *Genetic algorithms + data structures = evolution programs*. Springer-Verlag (1996).

79. N. Mowlavi, A. Jorrisen and M. Arnould, Fluorine production in intermediate-mass stars. *Astron. Astrophys.*, 311: 803 (1996).

80. Ortec, *EG&G Ortec Catalog, Modular Pulse-Processing Electronics and Semiconductor Radiation Detectors*. EG&G Ortec (1995).

81. W. H. Press et al., *Numerical recipes in C: the art of scientific computing*. Cambridge University Press (1992).

82. T. Rauscher and F. Thielemann, Astrophysical reaction rates from statistical model calculations. *Atom. Data Nucl. Data*, 75: 1–351 (2000).

83. T. Rauscher and F. Thielemann, Tables of nuclear cross sections and reaction rates: An addendum to the paper "Astrophysical reaction rates from statistical model calculations". *Atom. Data Nucl. Data*, 79: 47–64 (2001).

84. T. Rauscher, F. Thielemann and K. Kratz, Nuclear level density and the determination of thermonuclear rates for astrophysics. *Phys. Rev. C*, 56: 1613–1625 (1997).

85. A. Redder et al. *Z. Phys. A*, 305: 325 (1982).

86. A. Renda, Y. Fenner, B. Gibson, A. I. Karakas, J. C. Lattanzio, S. Campbell, A. Chieffi, K. Cunha and V. V. Smith, On the origen of fluorine in the Milky Way. *Mon. Not. R. Astron. Soc.*, 354: 575–580 (2004).

87. C. Rolfs. *private communication* (2002).

88. A. Schardt, W. A. Fowler and C. C. Lauritsen, The disintegration of ^{15}N by protons. *Phys. Rev.*, 86: 527–535 (1952).

89. V. V. Smith, *Chemical evolution in ω Centauri*, volume 4 (2004).

90. R. Stancliffe, M. Lugaro, C. Ugalde, C. Tout, J. Görres and M. Wiescher, The effect of the reaction rate uncertainty on the yield of fluorine from Wolf-Rayet stars. *arXiv:astro-ph/0504163v1* (2005).

91. F. K. Thielemann, M. Arnould and J. W. Truran, *Reaclib Data Tables of nuclear reaction rates* (1991).

92. F. X. Timmes, J. W. Truran, J. T. Lauroesch and D. G. York, Light-element abundances from z=0 to z=5. *Ap. J.*, 476: 464–478 (1997).

93. F. X. Timmes, S. E. Woosley and T. A. Weaver, Galactic chemical evolution: hydrogen through zinc. *Ap. J. Suppl.*, 98: 617–658 (1995).

94. C. Ugalde, *Estudio de la dispersión elástica en el sistema $^{12}C+^{24}Mg$. Honours Thesis.*. Universidad Nacional Autónoma de México (1997).

95. C. Ugalde, R. Azuma, A. Couture, J. Görres, M. Heil, K. Scheller, E. Stech, W. Tan and M. Wiescher, The reaction rate for the destruction of fluorine in AGB stars. *accepted. Nucl. Phys. A* (2005).

96. C. Ugalde, A. Couture, J. Görres, E. Stech and M. Wiescher, The $^{19}F(\alpha, p_1\gamma)^{22}Ne$ reaction and the abundance of fluorine in AGB stars.*submitted. Rev. Mex. Fis.* (2005).

97. C. Ugalde, J. Görres, M. Lugaro and M. Wiescher, Rates for reactions relevant to fluorine nucleosynthesis. *Mem. S. A. It.*, 75: 712–716 (2004).

98. C. Ugalde et al., The $^{19}F(\alpha, p)^{22}Ne$ reaction and the nucleosynthesis of fluorine. *to be published* (2005).

99. C. Ugalde et al., Fluorine targets for high intensity beam experiments in nuclear physics. *to be published* (2005).

100. R. V. Wagoner, Synthesis of the elements within objects exploding from very high temperatures. *Ap. J. Suppl.*, 18(162): 247–295 (1969).

101. K. Werner, T. Rauch and J. W. Kruk, Fluorine in extremely hot post-AGB stars: Evidence for nucleosynthesis. *Astron. Astrophys.*, 433: 641–645 (2005).

102. S. Wilmes, V. Wilmes, G. Staudt, P. Mohr and J. Hammer, The $^{15}N(\alpha,\gamma)^{19}F$ reaction and nucleosynthesis of ^{19}F. *Phys. Rev. C*, 66: 065802 (2002).

103. S. Woosley, D. Hartmann, R. Hoffman and W. Haxton, The ν-process. *Ap. J.*, 356: 272–301 (1990).

104. S. E. Woosley and W. C. Haxton, Supernova neutrinos, neutral currents and the origin of fluorine. *Nature*, 334: 45–47 (1988).

105. C. Yang, On the angular distribution in nuclear reactions and coincidence measurements. *Phys. Rev.*, 74: 764–772 (1948).

106. J. Ziegler, *The Stopping and Range of Ions in Matter*, volume 2–6. Pergamon Press (1985).

107. J. Zyskind and P. Parker, Remeasurement of the low-energy cross section for the $^{15}N(p,\alpha_0)^{12}C$. *Nucl. Phys. A*, 320: 404–412 (1979).